A FIBER-OPTICS, REAL-TIME DOSIMETER BASED ON OPTICALLY STIMULATED LUMINESCENCE OF Al_2O_3:C AND KBr:Eu, FOR POTENTIAL USE IN THE RADIOTHERAPY OF CANCER

By
RAZVAN GAZA

Bachelor of Science
Western University of Timisoara
Timisoara, Romania
1996

Master of Science
Western University of Timisoara
Timisoara, Romania
1998

Submitted to the Faculty of the
Graduate College of the
Oklahoma State University
in partial fulfillment of
the requirements for
the Degree of
DOCTORATE OF PHILOSOPHY
May, 2004

A FIBER-OPTICS, REAL-TIME DOSIMETER BASED ON OPTICALLY STIMULATED LUMINESCENCE OF Al_2O_3:C AND KBr:Eu, FOR POTENTIAL USE IN THE RADIOTHERAPY OF CANCER

Thesis Approved:

Stephen W.S. McKeever

Thesis Adviser

Joel J. Martin

James P. Wicksted

Kenneth E. Bartels

Al Carlozzi

Dean of the Graduate College

ACKNOWLEDGEMENTS

Even though the title page of this thesis lists me as its sole author, this document represents the product of the efforts of a great many number of people. Without their contribution expressed in various forms of love, patience and skill this adventure of mine wouldn't have been possible.

First, I need to thank my grandparents Alexandru and Maria Dinca, and Adrian and Victoria Gaza for helping me grow into the person I am today. Thank you for showing me unconditional support during my entire life, and for educating me in light of your moral values and cultural heritage. I thank my parents Iosif and Severina Gaza for caring for my well-being, and my baby-brother Victor for coping with an older sibling who sometimes assumed the undeserved role of a surrogate parent. To my uncle Paul Gaza, thank you for all those Sunday morning phone calls. To my cousin and life-long friend Julius Gaza, thank you for the e-mails waiting in my Hotmail Inbox folder every morning.

I want to thank all my friends for their moral support. To Daniel and Diana Dumitru, for letting me know that it was possible to continue my studies at Oklahoma State University; to Doina and Ludovic Kovalik, for giving me advice and support during the hardest time of my life; to George Farca, for discussing yet another LabVIEW detail while drinking a cup of coffee.

To Sharon and Lindsay Jones, thanks for being our 'Oklahoma family', and for offering us a home away from home.

I am indebted to all the teachers that inspired me over the years I spent as a student, and oriented me toward a career in science. Among them, I want to mention the names of Mr. Mircea Niculescu, Mrs. Ildiko Pataki, and Mr. Sever Rotea.

My deepest gratitude goes toward the faculty of the Department of Physics here at OSU. You did more than just teaching me physics, you also made me feel proud to belong to a very special community.

Dr. Paul A. Westhaus: I only wish that at some point in my life I will be able, as a professor, to raise to the standards set by your example. Thank you for bringing Ramona and me to the U.S., and for offering a job to a foreign student who was hardly able to put together a full sentence in English. Thank you for making a vocation out of your duties as graduate coordinator. We, the graduate students, had the most to gain out of it.

Dr. David W. Peakheart: thank you for setting my future on the right track. Thank you for showing me a PMT for the first time in my life. Thanks for teaching me how to align an optical setup, how to control a GPIB interface in HP Basic, how to take apart a Nitrogen laser and how to put in back, how to grow a LiF crystal, and so many more. Thank you for being both an instructor and a friend.

Dr. Joel J. Martin: Thank you for always having the right ‘gizmo’ around, whether it was a solid-state relay or an alkali halide sample doped with the right amount of rare earths. Thanks for correcting the misspellings in my plan of study, and for noticing the victorious look in my eyes after a successful crystal growth run.

Dr. Stephen W.S. McKeever ‘The Boss’: Thank you for helping me fly as high as I could. Doing research in your lab was the most fun I had in my life. Thanks for trusting me enough to let me explore uncharted territories. I only hope that, through my

accomplishments, I was able to (at least partially) return to you the joy of my discoveries. It's been a privilege to work for you.

I am grateful to Dr. Kenneth E. Bartels and to Dr. James P. Wicksted for their guidance as members of my Ph.D. committee, as well as to Dr. Robert J. Bahr.

I want to thank Dr. Mark Akselrod, Dr. Anna Akselrod and Landauer, Inc. for offering us logistic and financial support during the course of this project, in addition to the Al_2O_3:C samples that represented the main focus of our research.

I would like to thank my colleagues in the Dosimetry Lab for their constructive criticism in all matters regarding this project. I am grateful to Dr. Jerimy Polf for introducing me to this area, and sharing the know-how resulted from his previous work on the fiber dosimeter. I am especially thankful to Dr. Enver Bulur who, as far as I know, is the author of the original concept of a single-fiber OSL reader, for sharing with me his vast knowledge, suggesting ideas and offering logistical and technical solutions to the problems I was often faced with.

My gratitude goes to Dr. Lars Bøtter-Jensen and the research team at Risø National Lab, for giving me the occasion to spend a month as a visiting researcher in Denmark, and for sharing with me the subtleties of the 'Swedish Suitcase'.

The hospital testing of the readers was possible only with the support of several people, namely Dr. Kris Gast, Mr. Mike Rohan and Mrs. Kim Vann (Fort Smith, AR.), Dr. Sven Bäck and Dr. Joachim Medin (Malmö, Sweden), and Dr. James Durham (Fort Collins, CO).

I want to thank the staff of the Department of Physics; to Mr. Mike Lucas, for his professional assistance in all matters related to the instrumentation work-shop; to Mr.

Warren Grider and to Mr. Charles A. Hunt for their technical expertise; to Mrs. Susan Cantrell and to Mrs. Cindi Raymond, for their great assistance in keeping track of my work clearance, payroll advice, order requests, invoices, all of those on top of preparing the coffee every morning.

Last, and most important, I would like to thank my wife, Ramona, for being my companion on this long, winding, sometimes cheerful and sometimes painful journey. I sure hope we are now one step closer to finding what we're both looking for.

TABLE OF CONTENTS

LIST OF TABLES

LIST OF FIGURES

CHAPTER ONE

INTRODUCTION

1.1. Brief history of the medical applications of radiation

One of the most dramatic breakthroughs in the history of modern medicine took place on November 8, 1895. That day, Wilhelm Conrad Roentgen noticed the unexpected glow coming from a platinobarium screen situated 9 feet away from a tube containing a rarefied gas which was traversed by an electrical current. Because of their mysterious origin, he referred to the invisible energy emerging from the tube as 'X-rays'. X-rays were found to possess the ability of passing through objects that were completely opaque to visible light and yet was capable of creating latent images on photographic plates. The image of Roentgen' wife's hand appearing on a photographic plate is one of the first radiographs ever obtained and dates from December 22 of that same year.

The scientific world reacted enthusiastically to Roentgen's discovery. During the following years, extensive research in the area was performed and new information on the subject quickly became available. In 1896, Henri Bequerel noticed that radiation with similar properties was spontaneously emitted by uranium samples. Two years later, Pierre and Marie Curie isolated another radioactive element, radium.

With the infusion of knowledge, practical applications, especially in the medical areas, started to blossom. In February 1896, Edwin Brant Frost from Dartmouth, MA, irradiated a patient named Colles in order to obtain a photographic image of a fractured bone. This first example of medical radiography was used by Frost's brother, a medical doctor, to devise the appropriate treatment for the patient.

In January 1896, Emil Grubbe, a therapist from Chicago, irradiated a breast cancer patient by placing an X-ray tube in the proximity of the body [1]. After multiple treatments, he noticed regression of the tumor. This observation acknowledged the first accomplishment of teletherapy - the technique of irradiation with beams originating from sources placed outside the body. In 1901 [1], Robert Abbe, surgeon at St. Luke's Hospital in New York, had the idea of surgically implanting a glass container filled with 100*mg* of radium inside the body of a patient suffering from hyperthyroidism. The radioactive material was extracted after 1 day, the patient was sent home, and after 6 years he was reported to be in good health, with no signs of a recurring illness. In its modern version, the treatment consisting of implanting radioactive seeds inside a patient's body, in the proximity of the tumor, is known as brachytherapy, and is considered the preferred procedure for addressing certain types of cancers.

While diagnostic radiology quickly became a widespread medical technique, especially during and immediately after World War I, radiotherapy gave practitioners reasons for concern no later than a few years after its inception: recurring tumors, life-threatening damage to healthy tissue, and lack of effectiveness in treating deeply situated tumors.

The ignorance regarding the effects of radiation on human tissue, coupled with a misplaced overconfidence in the beneficial effects of X-rays, led to excessive and unnecessary exposure of humans to radiation fields. The absence of specialized training programs for radiotherapists led to a generally empirical approach for treatments, and this in turn resulted in pessimistic prognoses for cancer patients undergoing radiation therapy [2]. Contrary to expectations, improvements in the radiation sources did not lead to better results. With the more intense sources available, the general trend was to reduce the

length of radiotherapy by irradiating the tumors with large doses in single fractions [1]. However, this approach resulted in worse outcomes than previously obtained by stretching the delivery of the same dose over multiple irradiation sessions.

Once the fundamental mechanisms of radiation-matter interaction started to clarify, it became evident that in order to treat deeper tumors, higher energy beams were needed. By 1920, $200kVp$ X-ray tubes became available [3], and the first megavoltage systems appeared before 1940. After World War II the artificial production of a ^{60}Co offered a radioactive material emitting $3MeV$ γ-rays, which could be used as a less expensive alternative to radium. Another result of war-related research was the linear accelerator (LINAC), which became the most important radiation source used for external therapy. The LINAC was able to produce intense beams of both photons and electrons with energies up to $40MeV$.

1.2. Interaction of the ionizing radiation and tissue

Particles such as photons and energetic charged particles such as electrons, capable of ionizing the medium they pass through by way of a large enough energy transfer during atomic collisions, are described under the general name of 'ionizing radiation'. The physical quantity describing the amount of ionizing radiation absorbed by a medium is the radiation dose D, defined as the energy deposited per unit mass in the medium it passes through. The S.I. unit for dose is $1Gy$ (Gray).

$$D = E/m \tag{1.1}$$

$$1\,Gy = 1\,J/1\,kg \tag{1.2}$$

An older unit is known as the *rad*, with

$$1\,Gy = 100\,rad \tag{1.3}$$

For radiation protection purposes, the health effects induced by ionizing radiation on living organisms can be more accurately described in terms of the dose equivalent H rather than the dose D:

$$H = Q \cdot D \tag{1.4}$$

where the dimensionless quality factor Q accounts for the different biological sensitivity of different types of tissues and for different types of radiation quality. The S.I. unit for dose equivalent is 1*Sv* (Sievert). An older unit for dose equivalent in 1*rem*, with

$$1\,Sv = 100\,rem \tag{1.5}$$

The effects of ionizing radiation on human tissue, as well as on other living organisms, can be both stochastic and deterministic.

Age at First Exposure (years)	*H* (*Sv*)	
	Female	Male
25	0.4	0.7
35	0.6	1.0
45	0.9	1.5
55	1.7	3.0

Table 1.1: 10-year career limits based on a 3% cancer mortality risk increase

Stochastic effects occur over long periods of time following the absorption of small doses over the natural background, and are represented by an increased probability of developing cancers and hereditary effects. The published [4] values for career-limit dose intakes are reproduced in table 1.1. They represent the whole-body dose equivalents received during a 10-year career, determined to generate a 3% excess lifetime risk of

mortality from cancer. Additional effects derived from the absorption of the respective dose equivalents are increases in the risks of occurrence of heritable effects (by 0.6%) and of developing forms of non-lethal cancers (by 0.6%).

Deterministic effects occur promptly after irradiation and are directly associated with it, following the absorption of larger doses. The medical symptoms of exposure to high doses can be brutal, and for large whole-body doses of more than 20*Gy* they include damage to the central nervous system, diarrhea, drowsiness, tremor, convulsions, incoordination and coma. Death occurs within hours or mostly days. Data obtained from research related to the 1986 Chernobyl accident indicate that doses of 2*Gy* to 5*Gy* produce a mortality of 80% even with the best available medical care [5].

The lethal effects on living cells follow as a consequence of the ionizations produced by the incident energetic particles (photons, charged particles, or neutrons). The specific mechanisms are still subject to debate. According to some authors [6, 7], an important effect is given by chemical interactions of the cell constituents with reactive radicals resulting from the ionization of the molecular solvent (water). Ionization of the cell constituents is also presumed to influence the extent of the damage.

The radiation sensitivity varies for different types of tissues. The general rules [7] are that the sensitivity increases with the oxygenation (vascularization) level and rate of division (reproductivity).

The destructive effects of the radiation on living cells constitute the biological basis for radiotherapy. The fact that certain types of malignant cells are more sensitive to radiation than normal cells [6] constitutes one of the principles of radiotherapy. A second widely accepted principle is that radiotherapy outcomes can be improved by the fractionation of

the dose. Rather than delivering a single large dose, modern treatments generally consist in delivering 30 to 40 daily fractions of approximately 2*Gy* each [6].

There is some controversy on the mechanisms leading to better results of fractionated therapy versus single-dose treatments. An explanation could reside in the regeneration processes aiding the preferential recovery of healthy tissue that has suffered sub-lethal damage [6]. Another reason can be related to the gradual re-oxygenation, and the subsequent radio-sensitization of the malignant cells undergoing radiotherapy [8].

Another fundamental strategy of radiotherapy is to irradiate the patient with beams capable of delivering a well-defined spatial distribution of radiation dose. The task is to deliver a large enough dose to destroy the tumor, and at the same time minimize the irradiation of the normal tissue. The procedure is known as conformal radiation therapy [9], and it employs several techniques to achieve selective dose delivery at the target.

When radiation passes through a medium, energy is not deposited uniformly along the path of the radiation beam. The absorbed dose increases with distance up to a point referred to as dose-maximum depth, after which it decreases.

For the same particle type, as the energy of the particles increases, the dose-maximum occurs deeper in the medium. Therefore, beams of higher energy can be effectively used to treat deep tumors. For a nominal dose at the tumor, the energy imparted to the skin and the superficial tissue will be smaller.

For different types of particles, the dose-depth profile has different shapes, with the steepness of the peak increasing with the mass of the particles. Photons penetrate in a medium deeper than ionized particles with the same energy, and present broad maxima in the dose deposition profile. Heavy charged particles (HCP) such as protons and heavy

ions present dose-deposition curves with highly localized maxima known as Bragg peaks. It is suggested [10] that such beams should be used for treatments requiring abrupt variations in the spatial dose distribution.

The different shape in the dose deposition profiles of different types of particles can be explained by differences in the physical mechanisms by which their energy is transferred to the medium [10].

Charged particles such as electrons and HCP gradually lose their energy while passing through a medium. Such particles directly transfer small fractions of their kinetic energy to each atom situated in the vicinity of their paths. As the incident particle loses its kinetic energy, the amount of energy that is transferred at each collision increases. Thus, most of the energy will be deposited toward the end of the particle's path, and will result is the previously described Bragg peak in the dose-depth profile.

In contrast, the energy from photons is not directly deposited in the medium. Collisions between photons and atomic constituents are probabilistic processes. When a collision takes place, the incident photon transfers a large fraction of its energy, or the entire amount, to secondary particles. These energetic charged particles then gradually lose their energy to the atoms situated in their path. As primary, uncharged radiation penetrates the material, the population of secondary particles builds up, as does the dose deposited by them. At some point, the attenuation of the primary radiation causes a decrease in the number of secondary particles, and thus determines a decrease in the absorbed dose. The broad peak in the dose deposition profile results from the convolution of the two processes involved in the energy transfer: the build-up of secondary particles and the exponential attenuation of the primary beam.

The effect of increasing energy on the dose-depth profile, as well as the difference between different particles (electrons and photons), is visible in figure 1.1. The graphs represent dose-depth deposition curves for beams of different radiation quality: 6*MV* photons, and 5, 6, 7, 10 and 12*MeV* electrons, generated by a Philips Elekta linear accelerator, measured with an ionization chamber in a water phantom (courtesy of Dr. J. Durham, Colorado State University).

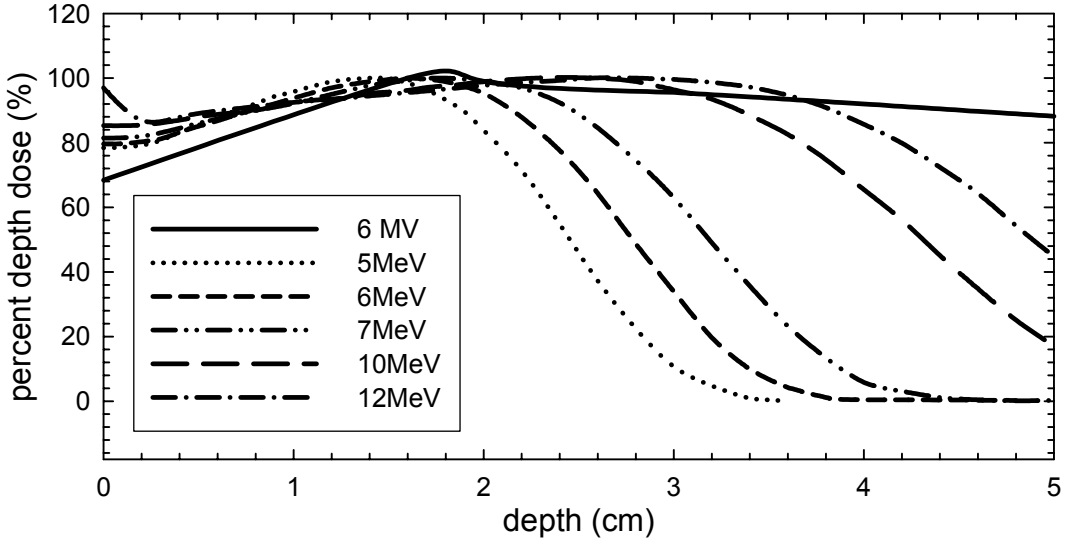

Fig. 1.1: Normalized dose-depth profiles in water for radiation beams of different quality generated by a Philips Elekta linear accelerator.

Shaping of the beam in the plane perpendicular to the irradiation axis is achieved by placing heavy radiation-absorbing materials between the irradiator and the target. Already in 1896, Grubbe used blocks of lead to shield the normal tissue from being irradiated. It is routine practice today to interpose lead alloy blocks in the path of the teletherapy beam to obtain the desired contour of the irradiated region.

Supplemental ways of delivering differential doses to the tissue in the path of the beam is provided by the so-called multiple-field technique. The beam is incident from different directions such that all beams intersect at the tumor. As a result, the tumor receives a large dose while the dose delivered to the healthy tissue is spread over an extended volume, as shown in the diagrams in figure 1.2 (reproduced from [6]).

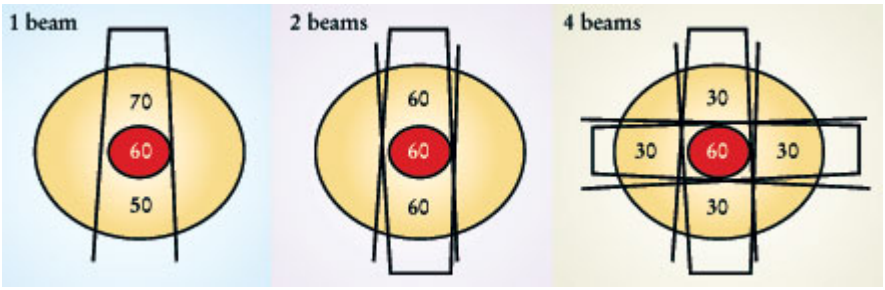

Fig. 1.2: Dose distribution achieved by using the multiple-field technique. As the number of beams increases, the relative dose delivered to healthy tissue decreases

The different available methods of controlling the dose distribution were used only to a limited extent before the middle 1950s, when computer technology reached a level where it could aid the development of treatments planning [9]. With new computational power it became possible to optimize the arrangement of multiple beams with different orientations so that the desired dose distribution at the tumor be obtained.

However, the input data available for computerized treatment planning was scarce. The computerized planning was not able to take into account individual variations in the anatomy and location of the tumor, which acted as perturbations to the standard models. The modern age of radiotherapy only started in the 1970s [9], after the introduction of the Computer Tomography (CT) scanner as an investigational tool.

Current 3-D planning systems import information on the anatomical structure from either CT scanners or Magnetic Resonance Imaging (MRI) devices. The imaging data are interpreted to give a 3-D map of the density of the region of the body that will be irradiated. With this information available, the treatment planning computer can predict an accurate dose-depth profile for a multitude of beams with different orientations and shapes. The shape of each beam can be controlled in real-time by a computerized multileaf collimator (MLC) system. A picture of a multileaf collimator is shown in fig. 1.3 (reproduced from the Varian web site [11]).

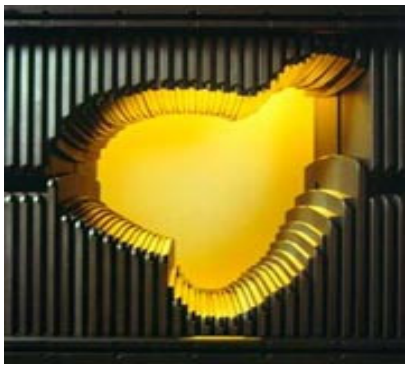

Fig. 1.3: Picture of a multileaf collimator, reproduced from the Varian web site

During the course of each treatment session, both the direction of incidence and the shape of the radiation beam can be quickly interchanged to irradiate the patient with the required spatial dose distribution. Besides acting as an on-off switch for radiation, multileaf collimators can be used to spatially modulate the intensity of each beam. Even though, in the historical perspective, the beam uniformity was considered one of the improvement goals, the idea of using beams of inhomogeneous intensity arose in the 1990s [6]. The technique is known as Intensity Modulated Radiation Therapy (IMRT). As

described by some authors [12], the technique consists in a series of steps, including:

i. Volumetric data from the CT scan is transferred to the planning system;
ii. The intensity of the treatment beams is optimized by inverse treatment planning;
iii. The dose distribution associated with the treatment beams is calculated;
iv. A functional relation relating the position of the leaves with the monitor units (mu) is generated and transferred to the MLC control unit on the linear accelerator;
v. The start-up parameters of the irradiation machine are checked;
vi. During irradiation, the correctitude of the position of the leaves is checked every 55*ms*. If the position is outside the tolerance limits, the beam pulses are delayed until the leaves reach the desired position;
vii. Prior to the first treatment on the patient, a test run is performed. Log files of the leaves position are compared to the intended values; in addition, flat-phantom film dosimetry is performed to obtain dose distributions for each beam.

1.3. Dosimetry issues

Regardless of the sophistication of the treatment planning machines and the computerized calculation procedures, only direct measurements can ultimately validate the correctitude of the treatment plan. It has been stated [9] that 'one of the keys to improved treatment technology is improvement in the measurement (…) of the dose distribution with which patients are treated'. Implementation of routine in-vivo dosimetry techniques during radiotherapy has been recommended by professional associations such as the American Association of Physicists in Medicine (AAPM) [13] and the International Commission on

Radiation Units and Measurements (ICRU) [14]. It is generally believed [15, 16] that the accuracy of delivering the dose distribution to the patient should be better than 3.5% (1S.D.).

The possibility of using diodes and Thermoluminescence Dosimeters (TLDs) for in-vivo radiation dosimetry at the location of the tumor has been investigated in a few studies [16, 17]. However, as of today there is no general method of performing in-vivo localized dose measurements during radiotherapy. Placing of the currently available dosimeters in the body is an invasive procedure and is generally avoided. Instead, measurements of the entrance and exit doses are performed, and from these measured values the midline dose is calculated according to several algorithms.

The entrance dose is defined as the dose deposited by the beam in a location situated at a distance equal to the depth of dose-maximum in the body, measured from the body surface exposed to radiation. The exit dose is the dose deposited at a distance equal to the depth of dose-maximum before the beam reaches the body surface opposite to the irradiation source. In order to measure the entrance and exit doses with dosimeters placed on the surface of the body (skin), build-up caps are needed. The mass thickness of the buildup caps is specific to different types of radiation quality in order to provide full Charged Particle Equilibrium (CPE) at the detector. The main disadvantage in using build-up caps is given by the perturbations they create in the dose-depth distribution in the body. Dosimeters equipped with build-up caps placed on the irradiated body surface will shift up the position of the dose maximum, resulting in larger doses delivered to the skin and smaller doses at the tumor.

The most common types of dosimeters used for in-vivo dosimetry are diodes, TLDs, and

radiosensitive (GAFChromic®) film. To a lesser extent are used ionization chambers. Lately, Electronic Portal Imaging Devices (EPIDs) have experienced an increase in popularity.

Table 1.2 summarizes the dosimetric properties of the routinely used types of dosimeters, with some observations related to their limitations.

Detector Type	Useful dose range (*Gy*)	Real-time readings	Observations
Ionization Chamber	2μ - 10	Yes	• Bulky
Semiconductor Diode	10m - 10	Yes	• Electrical connections • Frequent recalibrations
Radiochromic Film	3 - 100	No	• Surface dose measurements only
TLD	10μ - 20	No	• Complicated read-out procedure

Table 1.2: Dosimetric properties of the detectors used in radiotherapy

1.4. Optical fiber radiotherapy dosimetry

Both types of 'classical' dosimeters able to provide on-line (real-time) readings, ionization chambers and diodes, transfer their information to the processing units in the form of an electrical signal. Besides the lack of immunity to electro-magnetic noise and the shielding complications that would arise from implanting an electrical device into a patient, the size of these dosimeters prevent them from being used for dose determinations at the location of the tumor.

The optical transfer of information from dosimeter to the control unit arouse as a supplemental advantage when luminescent radiation detectors have been considered as in-situ dosimeters.

Several studies have been targeted at the possibility of using scintillator samples as

dosimeters in radiotherapy. Scintillators are materials that glow when exposed to radiation. The luminescence intensity is proportional to the irradiation dose rate. Extensive theoretical and experimental studies on water-equivalent plastic scintillators have been performed by Beddar et al. [18, 19]. Different varieties of scintillators with sizes (diameter/length) of 2.5*mm*/4.0*mm* and 1.0*mm*/4.0*mm* were exposed to electron and photon beam irradiation. The luminescence signal was guided along optical fibers with core diameters of 200μm, and measured with a photomultiplier tube (PMT). A consistent source of errors in the measurements was found to be the background signal generated in the optical, the so-called 'stem effect' attributed to Čerenkov radiation. Depending on the particles the irradiation was performed with, the Čerenkov signal is found to contribute with an additional signal of 3% (photon irradiation) or 12% (electron beam) to the luminescence generated in the scintillator. A previous paper by Beddar et al. [20] describes a pronounced angular dependence of the Čerenkov signal generated in a optical fiber on the angle between the fiber and the electron beam. The dynamic range of the intensity of the stem effect extends over two orders of magnitude.

In order to minimize the stem effect, it is proposed that a second un-terminated optical fiber be placed in parallel and in close proximity to the scintillator-terminated fiber. For radiation fields of low enough dose gradients, the amount of Čerenkov light would be equal in the two fibers. By subtracting the signals recorded in the two fibers, the scintillation signal can be isolated. Even when this background subtraction technique is applied, the measurement errors in brachytherapy radiation fields with large dose gradients are reported [21] to reach values of 10% at a distance of 12cm between the source and the scintillator.

An investigation on the possible use of thermoluminescence dosimeters as fiber detectors has been published in 1993 [22]. Thin samples of different TL phosphors ($CaSO_4$:Mn, CaF_2:Tm, CaF_2:Dy, $CaSO_4$:Dy) were attached to optical fibers. After irradiation, infrared (IR) light from an AlGaAs diode laser was sent through the fiber, heating the samples to a sufficiently high temperature. When heated, the samples emit luminescence which can be recorded over the duration of the process as a sequence of peaks known under the name 'glow curve'. The heating of the sample is performed twice after irradiation, the second measurement serving as a background reference. After background subtraction, the luminescence signal is integrated over the duration of the heating, and is found to be proportional to the absorbed dose. The authors state an achieved level of 1% accuracy (within the accuracy of the delivered dose) at doses larger than 1*Gy*. Improvements in the laser heated fiber dosimeters were later reported for different types of transparent TL glassy materials [23].

1.5. Proposed approach: Optically Stimulated Luminescence (OSL)

Derived from TL techniques, OSL consists in using light to stimulate the luminescence from the sample, rather than heat. When irradiated, part of the energy deposited by the incident particles in an OSL dosimeter is re-emitted promptly in the form of the radioluminescence (RL) signal. The mechanisms leading to the emission of RL are similar to the mechanisms of luminescence production in scintillators. Another fraction of the energy deposited by the radiation is stored in the OSL material in the form of charge carriers trapped by different lattice defects in the OSL crystal. Depending of the specific OSL material, the carriers can remain trapped for time intervals ranging from minutes to

geological ages. These carriers can be later stimulated with light of a suitable wavelength, which releases them in the crystal lattice, allowing them to relax to lower energy levels and emit the excess energy in the form of OSL. Most commonly, the stimulation is performed with light of constant intensity, and the luminescence from the sample is recorded as a signal with a decaying shape. The OSL intensity I obtained from a given amount of light stimulation is found to be proportional to the dose D absorbed in the sample and the sensitivity S of the sample, which is calibrated from irradiations at known doses.

$$I = S \cdot D \tag{1.6}$$

Research investigating potential uses of OSL fiber dosimetry as a remote radiation measuring tool, both for medical and other purposes, has resulted in several publications and U.S. patents. A patent was issued in 1992 [24] for a fiber dosimeter able to perform dose measurements during irradiation. The subtraction of the background signal (RL from the dosimeter and Čerenkov from the dosimeter and fiber) is made possible by the modulation of the stimulation light. Another patent was granted to Huston and Justus for a method using both RL during irradiation and post-irradiation OSL to perform remote OSL dosimetry [25, 26].

Different natural and synthetic materials exhibit OSL properties [27]. Starting from the year 2000, the use of synthetically grown Al_2O_3:C as a fiber OSL dosimetry material has been subject to side-by-side studies performed at Oklahoma State University and the Risø National Lab in Roskilde, Denmark. The initial approach was the one suggested by Huston and Justus, and the results revealed both advantages and the limitations of the method [28, 29].

1.6. This thesis

The purpose of the research presented in this thesis was to investigate further improvements in the functioning of the real-time, fiber OSL dosimetry system. It was desired to obtain dose estimates from the OSL signal only, after the subtraction of the RL / Čerenkov background.

Research was simultaneously conducted in two main directions: development of instrumentation, and design and implementation of data processing algorithms. The steps that were performed are presented in the chronological order in the following list:

i. Building a functioning prototype of the reader and preparing the fiber samples;
ii. Performing a basic characterization of the available dosimeters in terms of the OSL properties of interest;
iii. Developing proper algorithms for data acquisition and processing;
iv. Based on the proposed algorithms, writing the software used for data acquisition and instrument control;
v. Testing the system under a variety of conditions, and make the necessary adjustments.

Because of their different properties, the strategies used in approaching the two types of materials, Al_2O_3:C and KBr:Eu, were different, as were the solutions ultimately adopted.

The two portable fiber OSL readers, each custom-built for a specific OSL material, were extensively tested in lab conditions, using radiation sources delivering dose-rates in the range of interest for radiotherapy.

The systems were also tested under clinical conditions, in water phantom measurements with specific irradiation sources (LINACs), and the results were compared to

measurements performed with reference dosimeters (ionization chambers).

Initially intended for in-vivo and in-situ radiotherapy measurements only, the fiber OSL system shows promising signs for its use in other areas, such as dosimetry for investigative medical procedures (X-ray, CT), in-vitro mapping of brachytherapy source or 2-D dose mapping applications.

In order to preserve the logical flow of this thesis, separate chapters will be devoted to Al_2O_3:C and KBr:Eu, and each chapter will describe all the aspects related to the respective type of material, from basic characterization to laboratory evaluation of the final device.

The results of the clinical tests for both readers will be presented in a separate chapter, as will the alternative applications of the fiber reader, in areas other than teletherapy.

CHAPTER TWO

MODELS FOR OPTICALLY STIMULATED LUMINESCENCE (OSL)

2.1. Luminescence of Solids

Crystalline solids are materials consisting out of regular arrangements of atoms [30]. The interaction of the atoms in the crystalline lattice leads to the splitting of their discrete energy levels into quasi-continuous regions. Thus, possible energies for the electrons are situated in two energy bands, denoted as the valence band (V.B.) and the conduction band (C.B.), and separated by a forbidden region of width *Eg*, known as the band gap. The situation is pictured in figure 2.1.

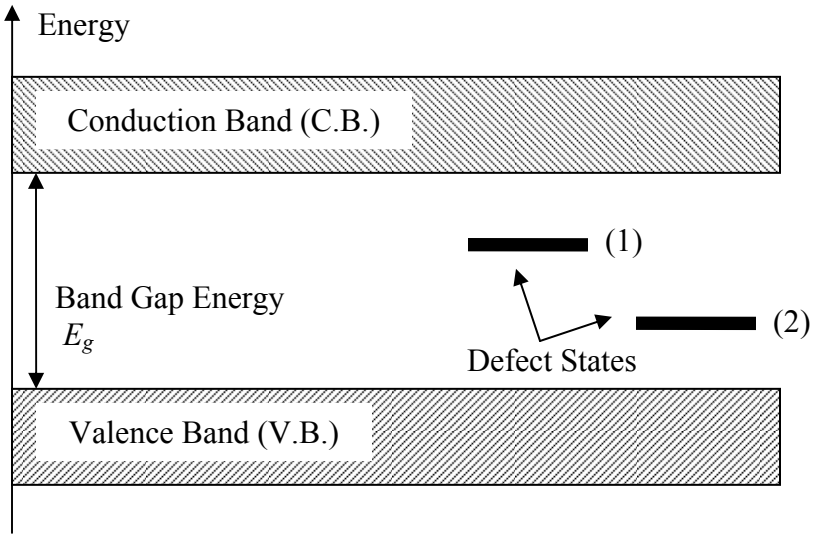

Fig. 2.1: Energy-band diagram

Energies situated in the valence band correspond to bound electronic states. If an electron absorbs a supplemental amount of energy $E > E_g$, then it becomes free to migrate through

the lattice. According to the second law of thermodynamics, the excited electron will eventually perform a spontaneous transition to a level of lower energy. The excess energy lost by the relaxing electron will be transferred to the crystal in the form of lattice vibrations, or, in case of a radiative transition, will be emitted as a quantum of electromagnetic radiation (a photon).

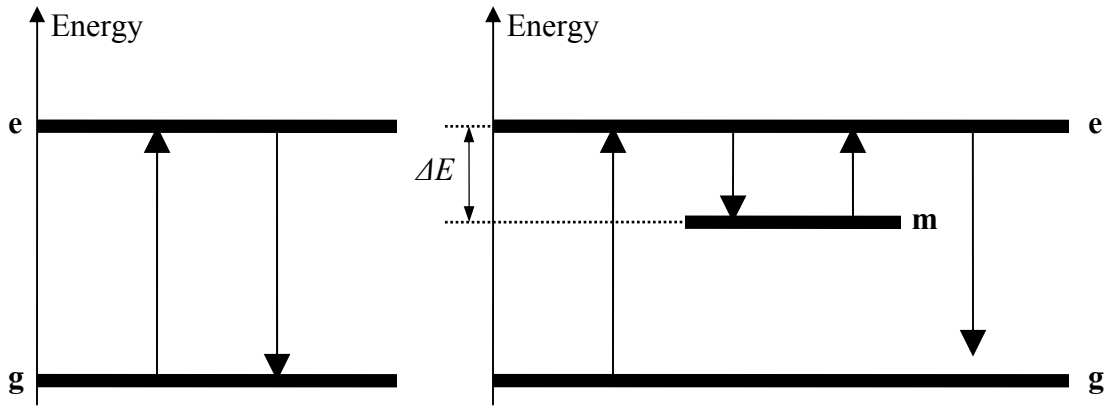

Fig. 2.2: Mechanisms of luminescence production

In the case of an ideal crystal, the states between which a transition occurs have to be situated in the allowed regions defined by the conduction and valence band. In a real crystal, the transitions can also involve energy levels situated within the band gap, induced by defects of the lattice such as dislocations, impurity atoms or vacancies.

The effect of emission of visible electromagnetic radiation, following absorption of energy from an external source, is known as luminescence [31]. Depending on the production mechanisms, luminescence can be classified as either fluorescence or phosphorescence, as shown in figure 2.2.

Suppose absorption of energy from an external source excites an electron from the

ground level **g** to an excited level **e**. If the relaxation occurs via a radiative transition from the excited level **e** directly to the ground level **g**, the emitted luminescence will be denoted as fluorescence or prompt luminescence.

In a different scenario, we consider an additional energetic level **m**, situated at a depth ΔE under the excited level. The electron previously excited on level **e** relaxes on the metastable state **m**, and remains there until, following the absorption of thermal or optical energy, it is once again excited to the level **e**. The luminescence emitted during the subsequent radiative transition to the ground level **g** is known as phosphorescence. Thermal processes are statistical in nature, and the probability of detrapping from state **m** depends upon the relative energies of the levels **e** and **m**. For a large energy depth ΔE the detrapping probability can become negligible at room temperature, and the electron can remain in the metastable state for indeterminately long periods of time.

In an attempt to construct a more realistic picture of the processes involved in a luminescence dosimetry crystal, let us now revisit the energy-band diagram represented in figure 2.1 and make some additional assumptions. If the energy level of the defect state (1) is situated sufficiently deep under the conduction band, but still above the Fermi level, the defect (1) will act as an electron trap. Also, we postulate that there exists a defect (2), associated with an energy state below the Fermi level. Thus, at thermal equilibrium, defect type (2) will be filled with electrons, and will act as a potential hole trap or recombination center. Finally, let us assume that the recombination of an electron from the conduction band with a hole from the recombination center (2) is the only radiative relaxation process taking place in the sample.

When the dosimeter is irradiated, ionizing radiation excites electrons from the valance

band into the conduction band. A fraction of them are trapped by defects of type (1), while others promptly recombine with holes previously captured at the recombination center. The recombination process is radiative and results in the emission of the so-called radioluminescence (RL).

If, after irradiation, the dosimeter is exposed to light of a suitable wavelength, the trapped electrons undergo a transition toward the conduction band, and subsequently recombine at the hole trap (2). The light emitted during this last process is referred to as Optically Stimulated Luminescence (OSL).

OSL radiation dosimetry is based on the observation that the amount of OSL emitted for a fixed amount of stimulation is proportional to the dose absorbed by the dosimeter from the radiation. 'Traditional' OSL is a two-step process, consisting in the irradiation of the sample, followed by optical stimulation. During the time stimulation is applied, the luminescence from the dosimeter crystal is measured with a suitable detector. One of the stimulation strategies is to illuminate the sample with light of constant intensity, and to record the OSL as a function of time. The absorbed dose is estimated from subsequent integration of the OSL signal over a given time interval. This procedure is known as continuous-wave OSL (CW-OSL).

2.2. The mathematical model of CW-OSL

A mathematical model for CW-OSL can be constructed by considering the electronic transitions taking place in the dosimeter during each of the two steps – irradiation and stimulation of OSL – as represented in figure 2.3.

The effect of trap filling (step 1) is described [32] by the following set of differential

equations:

$$\frac{dn_c}{dt} = f - n_c A_r n_h - n_c (N - n) A \tag{2.1a}$$

$$\frac{dn}{dt} = n_c (N - n) A \tag{2.1b}$$

$$\frac{dn_v}{dt} = f - n_v (N_h - n_h) A_h \tag{2.1c}$$

$$\frac{dn_h}{dt} = n_v (N_h - n_h) A_h - n_c n_h A_r \tag{2.1d}$$

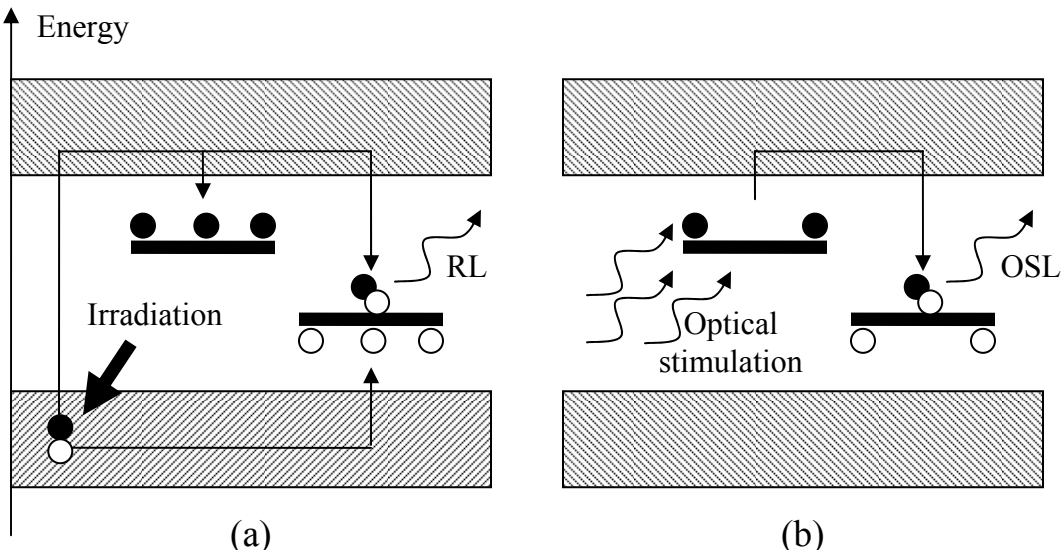

Fig. 2.3: Electronic processes in the two steps of 'traditional' OSL: (a) irradiation and (b) post-irradiation stimulation

where n is the concentration of filled electron traps, n_c and n_v are the concentrations of electrons and holes in the conduction and valence bands, respectively; N is the concentration of available electron traps; n_h is the concentration of the trapped holes (at

the recombination centers); N_h is the concentration of available hole traps; A is the trapping probability for electrons; A_h is the trapping probability for holes; A_r is the probability of electron-hole recombination (at the recombination center), and f is the electron-hole generation rate, proportional to the irradiation dose rate.

The system of equations (2.1) does not have an analytical solution. Thus, the introduction of simplifying assumptions is needed in order to obtain closed-form solutions. As an alternative solving approach, numerical calculations [32] have revealed a good proportionality between the filled trap concentration achieved after irradiation n_0 and the total charge generation $R = f \cdot t$, where t is the total irradiation time.

From the charge neutrality condition

$$n_c + n = n_h \tag{2.2}$$

the rate equation that governs the optical detrapping processes and the emission of OSL can be derived as:

$$\frac{dn_c}{dt} = -\frac{dn}{dt} + \frac{dn_h}{dt} \tag{2.3}$$

Under quasi-equilibrium conditions:

$$\frac{dn_c}{dt} << \frac{dn}{dt}, \frac{dm}{dt}; \qquad n_c << n, m \tag{2.4}$$

and negligible retrapping, the OSL intensity given by

$$I_{OSL} = C \cdot n_c n_h A_r \tag{2.5}$$

where C is a constant that accounts for the energy and spatial distribution of the photon emission rate $n_c n_h A_r$ can be rewritten in the form

$$I_{OSL} = -C\frac{dn}{dt} = C \cdot n \cdot p \qquad (2.6)$$

The rate p at which the electronic excitation events occur is dependent on the intensity of the monochromatic stimulation light of wavelength λ at the sample $\Phi(\lambda)$ and the photoionization cross-section at the respective wavelength $\sigma(\lambda)$:

$$p(\lambda) = \Phi(\lambda) \cdot \sigma(\lambda) \qquad (2.7)$$

The solution of equation (2.6) indicates an exponentially decaying shape for the time evolution of the OSL signal:

$$I_{OSL}(t) = C \cdot n_0 p \cdot \exp(-pt) = I_0 \exp(-pt) \qquad (2.8)$$

where n_0 is the concentration of trapped electrons in the sample after irradiation and at the time $t = 0$ of the stimulation process, and I_0 is the initial intensity of the OSL signal.

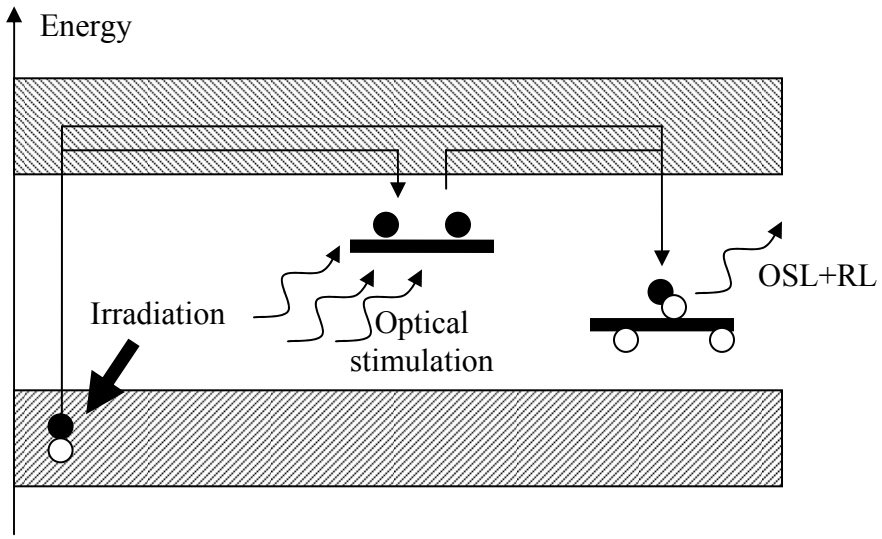

Fig. 2.4: Electronic process for simultaneous irradiation & stimulation processes

It can be noticed that the results obtained from the simple one-trap-one-recombination

center confirm the experimental results indicating a proportionality relation between the OSL signal and the total charge generation (i.e. the dose D).

Next, we will try to use the same simple model to predict the behavior of the system in the situation in which the sample is simultaneously irradiated and optically stimulated. In this case, all the previously described electronic transitions take place concomitantly, as shown in figure 2.4.

The luminescence signal measured from the sample contains both the prompt luminescence (RL) and the photostimulated (OSL) component. Our interest lies in describing the behavior of the OSL signal only. Modalities of separating the two signals – RL and OSL – will be discussed later in this thesis.

We will assume that the two recombination paths, one through direct relaxation and the other one involving trapping followed by optical stimulation, can be treated individually for the purposes of a theoretical model. Furthermore, we will consider that the concentration of the filled traps varies due to two processes: filling with a probability r proportional to the irradiation dose rate, and emptying with a probability p as defined by equation (2.7). With all the quantities previously defined, the equation describing the process is given as:

$$\frac{dn}{dt} = r(N - n) - pn \tag{2.9}$$

Assuming all the detrapped electrons recombine and result in luminescence emission, the number of recombination events, and thus the intensity of the OSL signal, will be given by the detrapping events:

$$I_{OSL} = C \cdot pn \tag{2.10}$$

With the initial condition given by the number of filled traps at the beginning of the

measurement,

$$n(t=0) \equiv n_0 \tag{2.11}$$

the general solution to equation (2.9) has the expression

$$n(t) = n_0 \cdot e^{-(p+r)t} + N\frac{r}{r+p}\left[1 - e^{-(p+r)t}\right] \tag{2.12}$$

Substituting the result (2.12) in (2.10), the OSL intensity can be obtained as

$$I_{OSL}(t) = C \cdot n_0 p \cdot e^{-(p+r)t} + C \cdot N\frac{pr}{r+p}\left[1 - e^{-(p+r)t}\right] \tag{2.13}$$

The first term in the expression of I_{OSL} appears due to a trapped electronic population pre-existing in the sample before the beginning of the experiment, and can be immediately compared to the expression obtained for a post-irradiation OSL, as described by equation (2.8). The irradiation of the sample during the stimulation process appears to modify the characteristic time of the exponential decay. The validity of our model is confirmed by the fact that, in the absence of irradiation ($r = 0$), equation (2.13) reduces to the classical expression (2.8).

The other term in the equation has the form of an exponential rise to a maximum, the amplitude of which is given by the number of available electron traps N, and is proportional to both the stimulation intensity p and, through the coefficient r, to the dose rate.

At this point, it is appropriate to summarize the results obtained from mathematical OSL models presented so far:

1. The 'traditional' CW-OSL technique consists in optically stimulating the luminescence response from a previously irradiated sample with light of constant intensity, to obtain an OSL signal with an exponentially decaying shape. The OSL

intensity is proportional to the initial number of filled traps, which in turn is proportional, as long as $n << N$, to the absorbed dose.

2. The OSL from a sample being irradiated at a constant dose rate, and stimulated with light of constant intensity, has mathematical form of a sum of two components – an exponential decay and an exponential rise to the maximum. The specific time of the exponentials depends both upon the dose rate of the irradiation and upon the stimulation intensity. The relative magnitude of the two components is dictated by the relation between the initial number of trapped electrons, and the number of the available electron traps.

CHAPTER THREE

DEVELOPMENT OF GENERAL REAL-TIME OSL PROCEDURES

3.1. Traditional OSL: practical aspects

As previously mentioned, traditional OSL is performed in two distinct steps: irradiation and read-out. Prior to irradiation, the dosimeter has to be 'reset'; this can be achieved by either thermal annealing or optical bleaching of the crystal

At any temperature *T*, there is a probability (per unit time) p_T that a trapped charge will be released in a thermal excitation process [31]:

$$p_T = s \cdot e^{-\frac{E}{kT}} \tag{3.1}$$

where *E* is the energy depth of the trap, *k* the Boltzmann constant and *s* is a constant with dimensions of inverse time.

If the sample is exposed to a temperature *T* for sufficiently long periods of time, the vast majority of the traps having energy depths smaller than kT will suffer thermal ionizations and the charge initially residing on them will be essentially depleted. The process is known as thermal annealing, and the temperature *T* at which the procedure is performed when used as a resetting technique depends on the type of material used.

Besides emptying the main dosimetric trap, thermal annealing is also supposed to reestablish the thermodynamical equilibrium in the dosimeter crystal.

For example, in the case of Al_2O_3:C, following the absorption of large doses, the recommended annealing temperature is higher than $800^{o}C$, even though the main dosimetric traps are situated at a thermal depth around $200^{o}C$. The high-temperature

annealing is required in order to empty the deep traps and thus reestablish the original equilibrium in competition processes [31]. For materials such as LiF:Mg, Ti [31], thermal annealing also serves the purpose to restore the sensitivity by resetting the clustering level of the defects responsible for charge trapping.

The energy required to ionize the filled traps can sometimes be provided by electromagnetic radiation in the form of light being absorbed in the crystal. As stated in chapter 2, the probability of depleting a certain type of traps by exposing the dosimeter to monochromatic radiation is given by [31]

$$p(\lambda) = \Phi(\lambda) \cdot \sigma(\lambda) \qquad (2.7)$$

where $\Phi(\lambda)$ is the flux of the monochromatic radiation of wavelength λ, and $\sigma(\lambda)$ is the wavelength-dependent photoionization cross-section of the trap.

According to (2.7), exposure of a sample with an optically active trap to light results in a depletion of the trap population. It is thus suggested that the 'resetting' of the sample can also be achieved by illumination. However, the procedure is not as efficient as thermal annealing in restoring the original properties of the dosimeter. Some of the traps / dosimetry materials are extremely insensitive to optical stimulation. Using higher energy photons to stimulate the deep traps, for example in the UV range, can actually result in trap filling, due to band-to-band excitations, rather than in trap depletion. Still, optical bleaching is reported as being sufficiently effective in erasing pre-existing information induced by small absorbed doses in Al_2O_3:C [31].

Following the annealing procedure, the dosimeter is exposed to ionizing radiation, which causes charge trapping, in an amount proportional to the absorbed dose.

Depending on the energy depth of a particular defect type, at room temperature (RT) the

trapped charges are released with a certain probability due to thermal excitation, the process being known as thermal fading. In the case of 'unstable', shallow traps, the pronounced fading causes dramatic changes in the concentration of trapped charges over relatively short time intervals, and the certain material is deemed unsuitable for traditional dosimetry purposes. Dosimetry-grade materials present at least one type of traps that is 'stable' at room temperature. For such defects, and in the absence of extreme thermal variations, the trap population does not vary significantly over periods of time extending up to geological intervals.

Dosimetry materials that are optically sensitive also incur post-irradiation information losses due to bleaching, if exposed to light between irradiation and read-out. Al_2O_3:C is an example of such material, which needs to be protected from natural light after irradiation. In the particular case of Carbon-doped sapphire, the wavelength-dependent photoionization cross-section has a very low value in the red-yellow region of the spectrum. Therefore, it is possible to handle the irradiated Al_2O_3:C dosimeters under illumination with an appropriate light color, without significantly depleting the luminescence signal stored on them. Other dosimetry materials, such as LiF:Mg, Ti and other alkali halides are essentially insensitive to light. The luminescence from such materials can be stimulated only by thermal processes. However, the impurification of these materials with certain dopants can drastically change their response to optical stimulation.

The same processes of thermal and optical excitation constitute the physical basis of the readout procedure of the dosimeters. Since all the defects can be thermally excited to release the trapped charge, Thermoluminescence (TL) or, more correctly, Thermally

Stimulated Luminescence (TSL), is a universal readout technique that can be applied for storage phosphors. It consists in measuring the intensity of the luminescence emitted by the sample while heating it in a controlled manner – usually involving a linear temperature increase. The luminescence recorded as a function of temperature presents a number of peaks, corresponding to traps at different depths being depleted. The quantity of interest is the luminescence intensity, integrated over a certain temperature range, which is found to be proportional to the radiation dose absorbed in the dosimeter.

Alternatively, the stimulation can be performed by illuminating the dosimeter with light in a wavelength range corresponding to a maximum in the photoionization cross-section of the investigated type of traps.

In order to measure the OSL from a luminescence dosimeter, the weak luminescence constituting the signal of interest has to be separated from the intense background light used for stimulating the sample. Assuming a typical value of 10mW for the optical power of the stimulation source and a measurable photon flux of 10^6 photons/second from the luminescence, emitted at a wavelength $\lambda = 420nm$, the order of magnitude of the relative intensity of the two signals can be calculated as

$$\frac{I_{OSL}}{I_{Stimulation}} \cong 10^{-10} \qquad (3.2)$$

Different methods have been developed to allow the separation of the OSL from the stimulation light. The method using temporal discrimination is known under the name of 'Pulsed OSL' (POSL) [31]. In the case of Al_2O_3:C, the principal mechanism of luminescence production is given by the capture of an electron by an F^+ center. The excited F^* center resulting from this capture relaxes through a radiative process, during

which the excess energy is emitted as a photon of wavelength centered at $\lambda = 420nm$.

$$e^- + F^+ \rightarrow F^* \rightarrow F + h\nu \qquad (3.3)$$

The lifetime of the excited F center is about $\tau \cong 35ms$. The OSL can be stimulated for short time intervals with light emitted by a pulsed laser (pulse width $w \cong 100ns$), and the luminescence can be measured between pulses only.

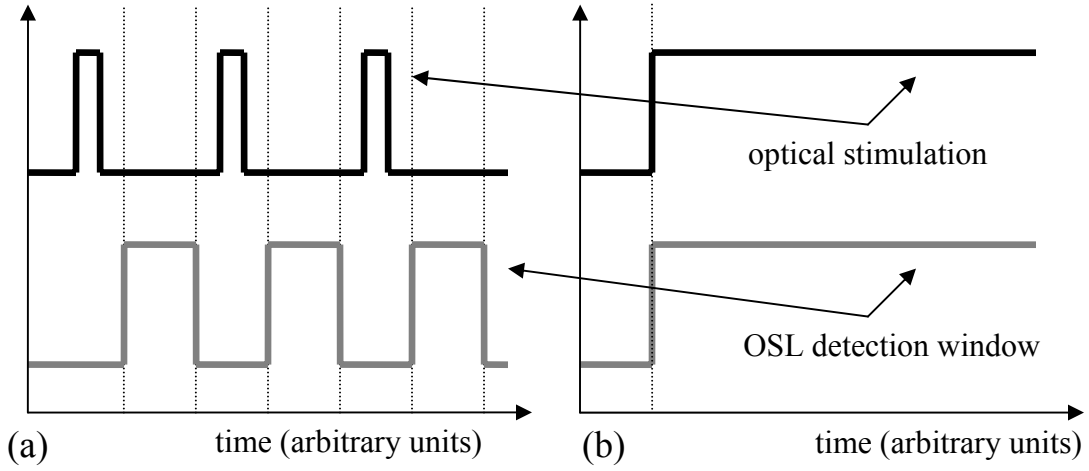

Fig. 3.1: Timing diagram for (a) POSL and (b) CW-OSL experiments with Al_2O_3:C

Alternatively, if the spectral separation between the stimulation and the emitted light is large enough, the discrimination can be performed in the wavelength, rather than in the time domain. The technique is known as continuous-wave OSL (CW-OSL). In this case, the optical stimulation is applied in a continuous manner (not in pulses) to the sample. The luminescence signal is separated by suitable filtration from the stimulation light, and is measured while the dosimeter is optically stimulated. The timing differences (not to scale) between a POSL and a CW-OSL experiment are pictured in figure 3.1.

In the case of Al_2O_3:C, the stimulation can be applied in the green region of the spectrum,

either with light emitting diodes (LEDs) at wavelength $\lambda \cong 525nm$ or with light from a frequency-doubled Nd:YAG laser ($\lambda = 532nm$). The bleaching efficiency would increase with the shift in toward shorter wavelengths, but the spectral overlap the stimulation light would make the filtration of luminescence much more difficult to achieve.

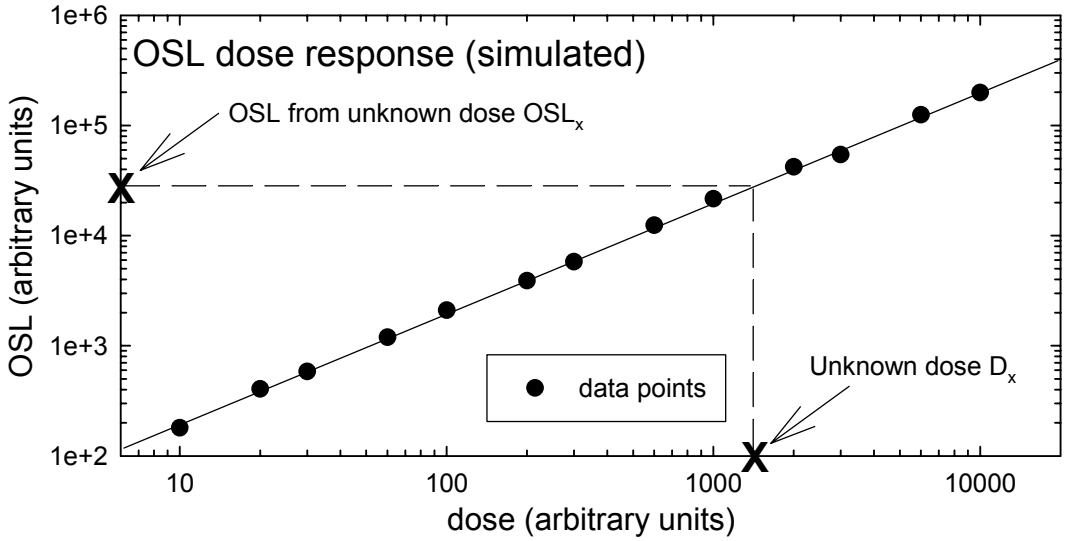

Fig. 3.2: OSL dose response; estimation of unknown dose from the OSL response

Prior to obtaining a dose estimate from the OSL signal, a calibration of the sample/system has to be performed. Known doses in the range of interest are delivered to the dosimeter, and the decaying OSL signal corresponding to each dose is measured. The data points are defined as the amount of OSL integrated over a fixed amount of time, starting from the moment when the stimulation is first applied. Afterwards, the data points are plotted on a graph, as shown in figure 3.2, and are fitted with some function. Materials commonly used as dosimeters show linear responses for doses within certain ranges, i.e. the OSL is proportional to the absorbed dose.

3.2. Real-time OSL (RT-OSL): The Creager approach

Instead of measuring the accumulated OSL after the irradiation, Creager suggested [24] an OSL method of measuring the dose during the irradiation procedure. Stimulation light is provided by an infrared (IR) source, and is directed along an optical fiber toward the dosimeter sample situated at a remote location. The dosimeter is held at the tip of the fiber probe, as depicted in figure 3.3. The luminescence from the dosimeter being irradiated is transported through the same fiber to a visible light detector.

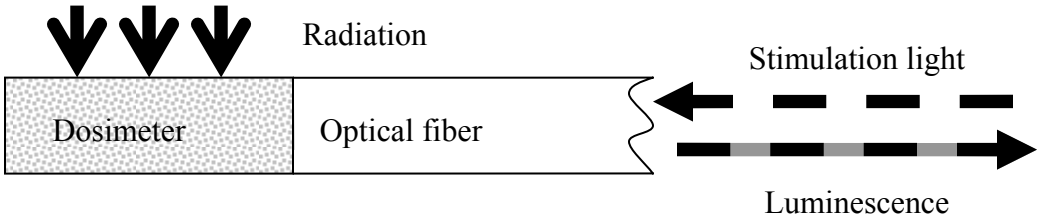

Fig. 3.3: Schematics of the fiber sample, as described by Creager

During the irradiation, the light intensity from the IR source is modulated. In the absence of optical stimulation, the light detector measures a fluorescence background from the dosimeter. If the irradiation is performed with beams customarily used in radiotherapy, the fluorescence background consists in the RL component (see figure 3.3a) and the so-called 'stem effect' signal generated in the light guide, as described in chapter 1. While the RL from the dosimeter sample is a proportional to the local value of the dose rate, the 'stem effect' unacceptably alters the spatial resolution of the dosimeter.

When, during irradiation, the sample is additionally illuminated with IR stimulation light, the OSL emitted by the dosimeter is added to the luminescence background, transmitted

through the fiber and measured at the light detector. By subtracting the fluorescence background from the total signal measured while IR stimulation is applied, the OSL from the sample can be separated from the luminescence background, and is found to increase linearly with the radiation output.

3.3. Defining the OSL signals: a necessary digression

The general procedure suggested by Creager suffers from lack of specificity in defining the OSL signals. As will be proven, the claim that the dosimeter is working in integrating mode, and returns a signal proportional to the concentration n_0 of filled traps is only valid for particular definitions of the OSL signal.

Even though it has been long known that the amount of light is a discrete physical quantity given by the flux and the energy of photons with a given spectral distribution, it is universally accepted that an instantaneous value for the light intensity can be defined.

However, the quantity obtainable through direct measurements is not instantaneous light intensity, but rather light intensity integrated over a specific time interval.

The general question we are raising at this point is – how will integrating the 'instantaneous' OSL signal affect the linearity of the dose response? In other words, should we expect to be able to interpret the OSL signal and relate it to the absorbed dose in a unique fashion, regardless of the OSL integration time?

The question can be easily answered in the case of post-irradiation stimulation, at least in the case of the simple 'one trap one irradiation center' model described here. In the absence of irradiation during optical stimulation, relation (2.13)

$$I_{OSL}(t) = C \cdot n_0 p \cdot e^{-(p+r)t} + C \cdot N \frac{pr}{r+p}\left[1 - e^{-(p+r)t}\right] \qquad (2.13)$$

simplifies to the form

$$I_{OSL}(t) = C \cdot n_0 p \cdot \exp(-pt) = I_0 \exp(-pt) \qquad (2.8)$$

Then, integrating the OSL intensity over an arbitrarily long time interval, starting from the application of stimulation ($t = 0$) and extending until a time τ results in the following expression for the integral OSL:

$$OSL(0,\tau) = \int_{t=0}^{\tau} I_{OSL}(t)dt = C \cdot n_0\left(1 - e^{-p\tau}\right) \qquad (3.4)$$

indicating a proportional dependence of the integral OSL on n_0.

In the more general case (2.13), the OSL integrated over the same interval ($0..\tau$) has the expression of the form

$$OSL(0,\tau) = C \cdot \frac{n_0}{p}\left(1 - e^{-p\tau}\right) + C \cdot \frac{Npr}{r+p}\tau - C \cdot \frac{Npr}{(r+p)^2}\left[1 - e^{-(p+r)\tau}\right] \qquad (3.5)$$

and its proportionality with n_0 is compromised.

Still, in a particular situation when the OSL integration time τ is small enough, so that the approximation $(p+r)\tau << 1$ holds,

$$\frac{Npr}{(r+p)^2}\left[1 - e^{-(p+r)\tau}\right] \xrightarrow{(p+r)\tau<<1} \frac{Npr}{(r+p)^2}\left[1 - 1 - (r+p)\tau\right] = \frac{Npr}{r+p} \qquad (3.6)$$

the last two terms in the right-hand side of (3.5) cancel each other, and the proportionality of the integral OSL signal with n_0, and thus with the absorbed dose is restored.

At this point, we can reconsider Creager's approach, and specify what changes are

needed in order to implement it for use:

1. The OSL integration time needs to be short. Since it is desired that the OSL from the dosimeter is completely depleted, the actual stimulation intervals may be relatively long.
2. From relation (2.13), even for infinite optical stimulation interval, the OSL from a sample under irradiation will not go to zero, and nor will the concentration of filled traps. Rather, both will reach an equilibrium level. Then the additional dose absorbed in the absence of stimulation, when the dosimeter works in integrating mode, will be given not by the maximum in the next OSL, but rather by the OSL increase from the equilibrium level to the maximum value.
3. When the optical stimulation is applied, the dosimeter does not function in integrating mode, as the concentration of the trap population does not increase proportionally to the absorbed dose. Thus, in order to obtain an acceptable 'duty cycle' from the reader, i.e. in order for the reader to spend a reasonably large fraction of time in integrating mode, it is desired that the optical stimulation intervals be as short as possible.

The changes described at the points 1. and 2. in the list above have been implemented with our OSL reader based on Al_2O_3:C, and some results obtained from it will be presented in section 4.3.5.

Solving the third issue – bleach the OSL to equilibrium levels with short stimulation intervals – is by far more difficult to achieve. Not only the duty cycle is an issue here, but also the frequency at which OSL data points (or updates in the dose estimation) can be obtained.

A typical clinical irradiation procedure is performed over time intervals on the order of tens of seconds. Ideally, from the requirement precision on the order of 1% needs to be achieved in delivering the prescribed dose, the number of measurements performed during this time should be on the order of 100. Accordingly, the frequency at which measurements are taken should be larger than a few *Hz*, or data points should be taken every a few hundred milliseconds.

Achieving complete OSL depletion, in a material like Al_2O_3:C, in a matter of a few hundreds of milliseconds, following the absorption of relatively high doses, poses serious difficulty. The time required to bleach the OSL from the dosimeter can be shortened if more laser power is applied. However, too large an optical power transmitted through the optical fiber and the associated optics is likely to alter their properties. Thermal effects will probably induce misalignments in the optics of the system, and the increase in the stimulation background will involve the use of additional filtration in front of the light detector (PMT) to separate the luminescence component. Also, according to the simple model we described for OSL, the characteristic exponential decay time of the OSL signal is inversely proportional to the laser power. Thus, reducing the decay time by one order of magnitude implies increasing the laser power by one order of magnitude, and may be prohibitive in price.

3.4. Real-time OSL with incomplete OSL depletion

As an answer to the issues described above, we suggest a method during which only partial depletion of the OSL signal is performed during each stimulation interval. Not having to wait for the complete resetting of the OSL signal increases the rate at which

successive measurements can be taken, and thus the number of data points that can be obtained during a fixed-time irradiation. As mentioned before, being able to perform fast updates of the total absorbed dose allows for an increased accuracy in delivering the prescribed amount of radiation to the patient.

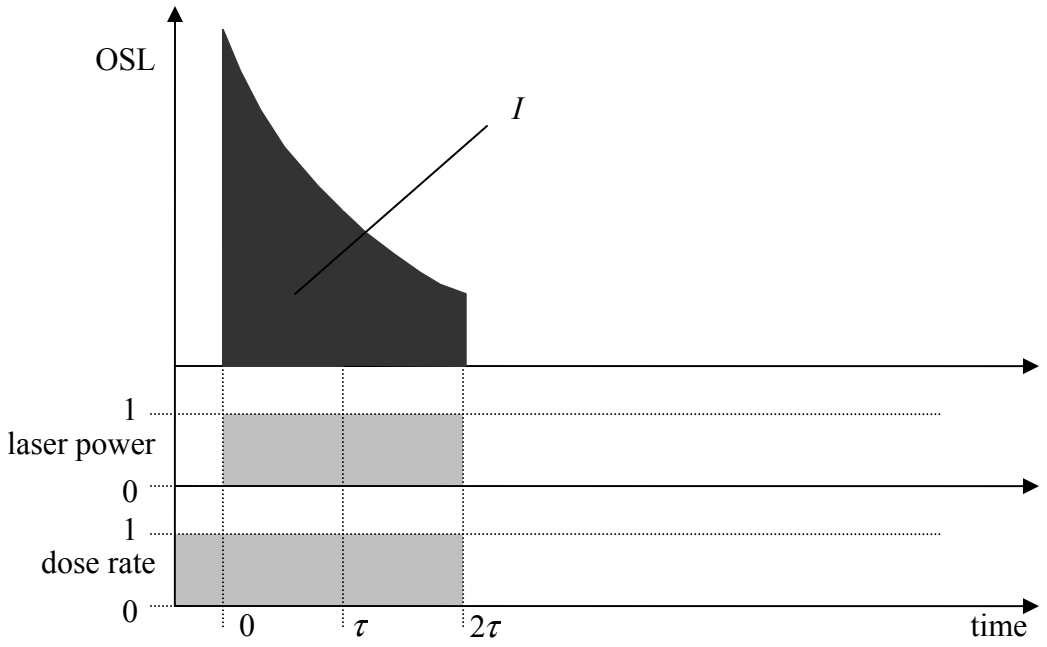

Fig. 3.4: OSL signal as a function of time

Because of the incomplete bleaching of the previous signals, each OSL signal will reflect, besides the dose delivered since the last laser stimulation, fractions of the doses that had been previously absorbed. In order to restore the linear dose response of the dosimeter, correcting procedures are required in order to perform the separation of the newly added dose from the artifacts.

Consider a sample under irradiation. Starting from the moment $t = 0$, optical stimulation

is applied for a time 2τ, and the luminescence is measured. After subtracting the previously measured RL, the value of the integrated OSL intensity is obtained as I. The time dependence of the OSL signal, given by the expression

$$I_{OSL}(t) = C \cdot n_0 p \cdot e^{-(p+r)t} + C \cdot N \frac{pr}{r+p}\left[1 - e^{-(p+r)t}\right] \qquad (2.13)$$

has a possible shape as represented in figure 3.4. Also shown in the picture is the time behavior of the stimulation laser, and of the dose rate (in arbitrary units).

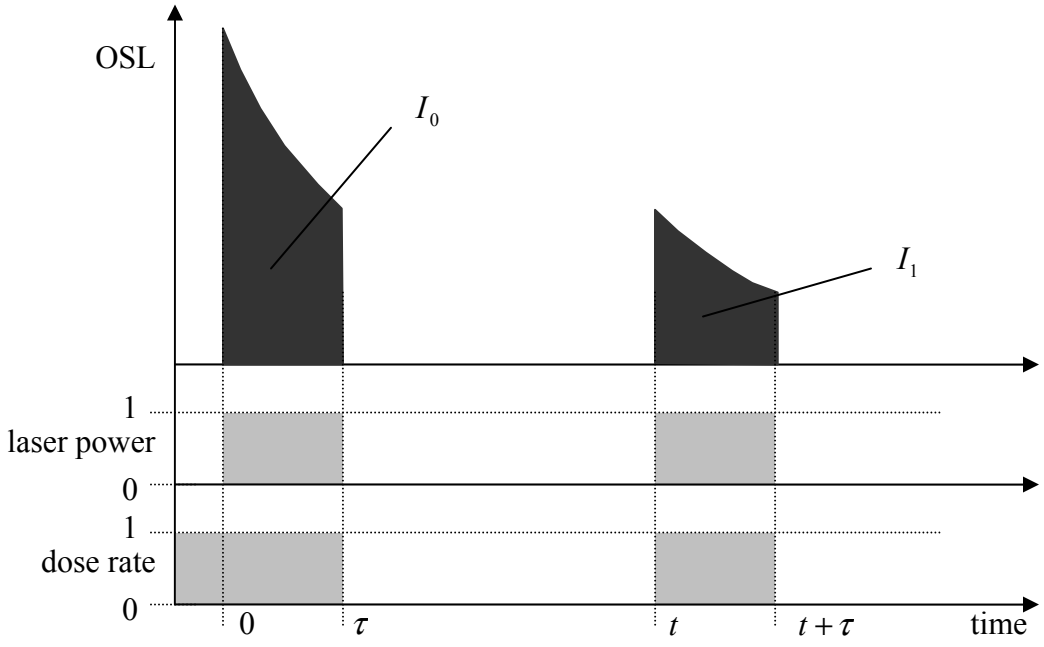

Fig. 3.5: Fractionated OSL signal w/o in-between irradiation

It is further understood that the time interval τ over which the OSL is integrated is taken to be as short as possible – usually on the order of 100*ms*. Still, the OSL signal of interest is represented by the area under the dark grey curve shown in figure 3.4, i.e. OSL integrated over a certain time interval.

Now let's assume that both the irradiation and the laser stimulation are sharply turned off at the time $t = \tau$, and then simultaneously turned on again at a later time t, for an additional duration τ. As a result, the OSL decay will be effectively split into two equally wide curves, of integrated intensities I_0 and I_1. Still, each of the two fractions will maintain its original shape, as shown in figure 3.5.

The two OSL signals I_0 and I_1 can be related by a factor that will be referred to in what follows as the 'Shape Coefficient' K_S:

$$K_S = \frac{I_1}{I_0} \tag{3.7}$$

In an alternate but equivalent interpretation, K_S can be regarded as quantifying the shape of the original OSL decay of duration 2τ.

Depending on the relative values of the quantities that appear in expression (2.13), K_S can only take positive values, both smaller and larger than 1. Sub-unitary values for K_S denote a decaying shape for the real-time OSL, as depicted in figures 3.4 and following. Supra-unitary of K_S values refer to an increasing OSL signal, which can occur if the initial concentration of filled traps is lower than the equilibrium value at a particular dose rate. In this case, the second term – the exponential rise to a maximum – will prevail in the shape of the signal given by (2.13).

It should be pointed out once more that K_S is defined for the case when the dosimeter is irradiated during the optical stimulations, but not between them. Thus, the time elapsed between the two stimulations, or the dose delivered between the successive stimulations are irrelevant for the value taken by K_S. However, according to relation (2.13), K_S is

dependent, through the value of the coefficient r, on the dose rate of the radiation absorbed during stimulation.

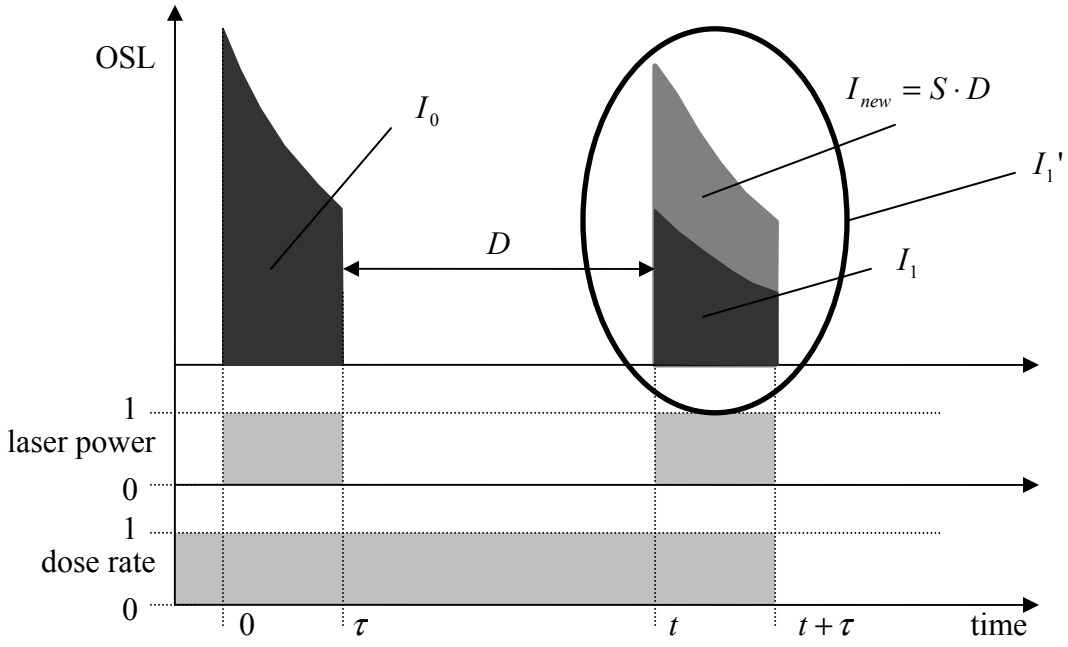

Fig. 3.6: Fractionated OSL signal with in-between irradiation

If the sample is irradiated between the two successive stimulations, the second OSL measurement of duration τ and started at time t will have a value I_1', larger than the previously defined I_1 by an amount I_{new}, proportional to the dose D absorbed between the two measurements:

$$I_1' = I_1 + I_{new} = I_1 + S \cdot D \qquad (3.8)$$

where S is the OSL sensitivity of the sample, defined for the particular timing conditions used in the experiment. The situation is described by figure 3.6.

After developing the formalism and defining the quantities of interest, we are now at the

stage where we can define the steps of a measurement procedure for the dose D delivered between stimulations, provided the values of the shape factor K_S and the sensitivity S of the sample are known. They consist in:

i. with the laser stimulation turned off, measure the luminescence background integrated over a time τ to obtain the value RL_0;

ii. turn the laser stimulation on for an equally long interval τ, during which time measure the luminescence as the sum of the background and the OSL to obtain $(RL + OSL)_0$;

iii. calculate the integral OSL signal alone as

$$I_0 = (RL + OSL)_0 - RL_0 \tag{3.9}$$

iv. from relation (3.4), estimate the value I_1 of the next OSL signal expected for the case in which no dose were absorbed in the sample between measurements:

$$I_1 = K_S \cdot I_0 \tag{3.10}$$

v. wait an arbitrarily long time interval;

vi. repeat steps i. to iii. to obtain the second OSL intensity I_1'

vii. calculate the newly absorbed dose fraction D from the difference between the actual OSL intensity I_1' and the expected value I_1, according to the relation:

$$D = \frac{I_1' - I_1}{S} = \frac{I_1' - K_S \cdot I_0}{S} \tag{3.11}$$

The procedure of calibrating the sample sensitivity S is straight-forward and can be performed as a traditional OSL measurement following irradiation with known doses, provided the timing (OSL integration time) and stimulation parameters (laser power) are

the same as for the real-time OSL (RT-OSL) measurement.

The estimation of the shape coefficient K_S is a more tedious procedure. Already the relation (2.13), derived from a simple one-trap-one-recombination-center model, predicts a shape dependence of the OSL signal on both the stimulation laser power and dose rate. The immediate observation that the characteristic time of the exponentials describing both the decaying and the rising parts of the OSL signal is of the form

$$\tau_C = \frac{1}{p+r} \tag{3.12}$$

suggests that the dependence of τ_C on the dose rate can be minimized by employing stimulation sources with higher optical power. Under such circumstances, a constant value for K_S should be used in the correction. As will be shown in the next chapter (figure 4.15), even in the case when high laser power justifies the use of a dose-rate independent K_S value, the approach cannot correct for different mixing of the OSL components in the total signal.

CHAPTER FOUR

REAL-TIME OSL (RT-OSL) OF Al_2O_3:C

4.1. OSL reader setup and sample preparation

The schematic diagram of the portable fiber reader based on OSL of Al_2O_3:C is presented in figure 4.1. All the electrical and optical components used in building the reader are commercially-available parts.

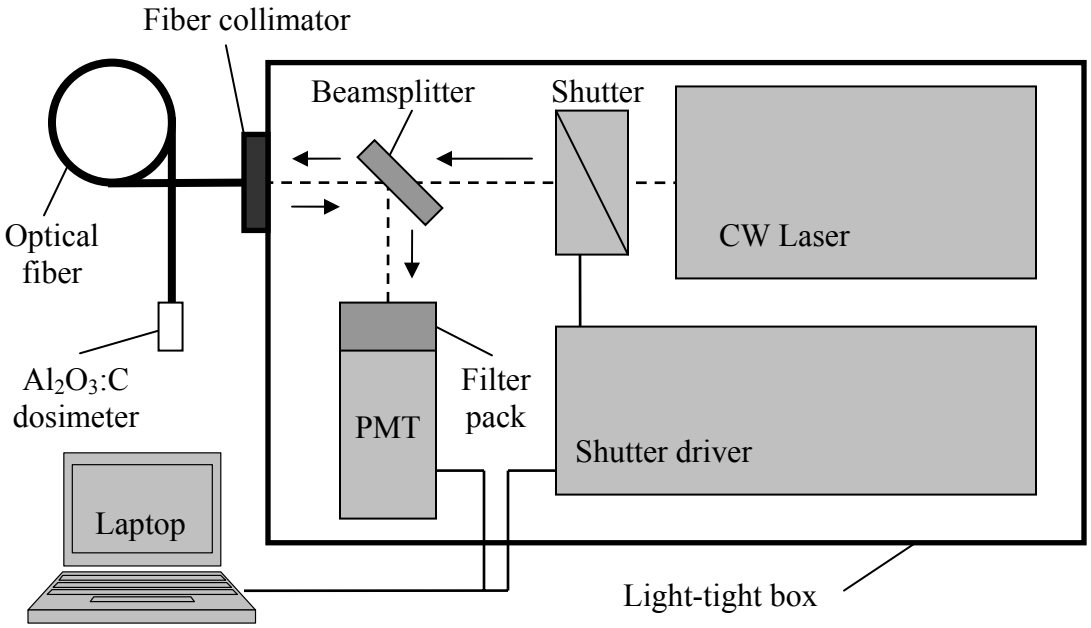

Fig. 4.1: Schematic diagram of the Al_2O_3:C fiber reader

The main optical components, the laser and the light detector (PMT) are contained in a light-tight box. A fiber-optics cable is connected to the reader and to the dosimeter. Stimulation light from the laser is collimated into one end of the optical fiber cable. The

dosimeter is situated in a remote location, and is attached to the distal end of the optical guide. The laser stimulation can be modulated by an optical shutter and is guided down the fiber to the dosimeter.

The luminescence light emitted by the Al_2O_3:C crystal is transported back to the light-tight box through the same optical fiber. The blue luminescence is deflected through 90º by the beamsplitter, separated from the laser background by the filter pack, and measured by the PMT.

Both the PMT and the electronic board controlling the shutter are connected to a DAQ card contained in a laptop computer. One of the DAQ card's counters indexes the PMT output, and a digital output port is used for the software-controlled modulation of the laser beam. Another digital port gates the power supply of the PMT.

Additional components not represented in the diagram are the power supplies for the laser and the optical shutter.

The detailed specifications of the components are listed below:

• Laser: Extreme Lasers HPM-100, frequency-doubled Nd:YAG, $\lambda = 532nm$, continuous wave (CW) operation, optical power $p = 100mW$, thermoelectric cooling (TEC) for increased stability in the output power. The optical power measured at the sample exceeds the value $p_S = 60mW$.

• Optical modulator/shutter: EOPC CH-61, operated by a DCH-60 driver, the frequency stability quoted by the manufacturer is ±0.005%. Due to the laser beam having a non-zero thickness, the transitions of the shutter blade induce an effective rise-time of approximately $1ms$ in the beam intensity (measured with a Thorlabs DET210 Si PIN photodiode, rise-time $1ns$, on a LeCroy 9400A $175MHz$ oscilloscope).

• Photomultiplier (PMT): Electron Tubes P10PC Ultra High Speed Photon Counting Detrector, $10^8 s^{-1}$ count rate capability, TTL output, $5V$ input voltage

• Optical fiber: Different types have been used, as shown in Table 4.1:

Fiber Type	Material	Typ. core diameter (μm)	Core refractive index
Mitsubishi ESKA	plastic	486	1.492
Thorlabs FT-600-EMT	silica	600	1.46 (typ)
Thorlabs FT-600-UMT	silica	600	1.46 (typ)
Thorlabs FG-550-LER	Silica	550	1.46 (typ)

Table 4.1: Optical fiber types used in OSL experiments with Al_2O_3:C

• Fiber collimator: Thorlabs F220-FC-A or F230-FC-A (300-600*nm* wavelength range)

• Beam splitter: OptoSigma 079-0040 (long-pass 510*nm*)

• Filter pack: Contains multiple filters, as described in Table 4.2:

Filter type	Description	Number used
CVI CP-SM-550-1.00	magenta subtractive	1
Optosigma 079-0010	short-pass 520*nm*	3
Delta BP395440 (DK)	band-pass 395-440*nm*	2

Table 4.2: Optical filters used in the Al_2O_3:C portable OSL fiber reader

• Data acquisition and control (DAQ) hardware: National Instruments DAQCard 6062E, PCMCIA bus, installed on a ProStar 2200 laptop (1*GHz* Intel Pentium III CPU).

• DAQ software: Various applications required by different types of experiments were written and run in National Instruments LabVIEW 6.1.

Optical cables with lengths between 1.5*m* and 15*m* were used. In order to increase their mechanical stability, and to minimize the influence of the ambient light on the

luminescence signal, they were covered by appropriate jackets.

One end of the fiber cable was terminated with an FC connector. The connector was attached to the fibers with commercially available, general-use two-component epoxy. Both ending surfaces of the fiber cable were fine-polished with sapphire abrasive film of granulation as fine as $1\mu m$.

The Al_2O_3:C dosimeters are manufactured by Landauer, Inc. as fiber-shaped single crystals. Individual samples of lengths on the order of $1cm$ were cut from the bulk single crystal fibers, and fine-polished on both ends.

A segment of plastic tubing, matched to the diameter of the optical fiber, was permanently sealed at one end. After the dosimeter sample was placed into the resulting enclosure, the free end of the optical fiber was forced through the same opening of the plastic tube, until it came into contact with the crystal sample. When required by the ambiental illumination conditions, the dosimeter and the adjacent fiber were covered with light-tight plastic caps. The resulting structure, schematically described in figure 4.2, showed good mechanical stability under normal operating conditions. Also, the sample could be repeatedly disconnected and reconnected to the fiber cable, allowing for direct sample comparisons using the same optical guide.

The wall thickness of the plastic tubing was measured at approximately $200\mu m$. Under low-voltage X-ray irradiation, it is expected that part of the energy of the incident photons will be absorbed in the tubing, and only the remaining fraction will be measured in the Al_2O_3:C dosimeter. Thus, direct comparison of the OSL signals resulted from irradiations under X-rays and higher energy irradiation would require additional calibration of the X-ray tube, which takes into consideration the dose attenuation at the

sample due to the plastic layer surrounding it. Still, for X-ray irradiations, the dose rate at the sample is proportional to the tube current.

At irradiations with particles of higher energy, the shielding effect of the plastic tubing becomes negligible. Even the beta particles resulted from the radioactive decay of $^{90}Sr/^{90}Y$, having energy on the order of $1MeV$, can penetrate over ranges of a few millimeters in water (or in plastic, which has a comparable mass density). At the energy ranges commonly used in radiotherapy, the perturbation induced by the plastic tubing on the dose absorbed in the dosimeter is effectively zero.

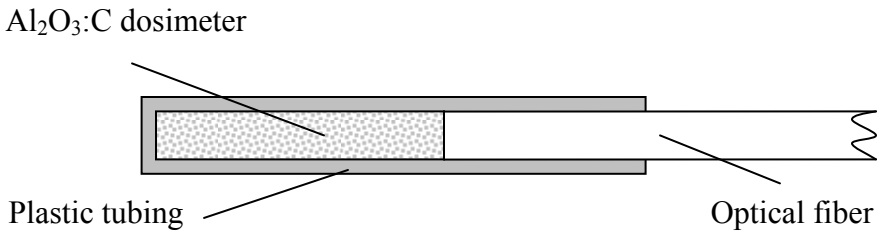

Fig. 4.2: Schematic fiber-sample connection diagram

Since the indices of refraction of sapphire ($n = 1.79$) and silica ($n = 1.46$) differ, some inherent losses will occur in the light intensity transmitted between the two media. Since the luminescence is generated in the dosimeter in all spatial directions with the same probability, and because of the higher refraction index of Al_2O_3, some of the blue light is likely to go through the process of total reflection at the sapphire-silica interface.

The use of an index-matching gel to maximize light transmission from dosimeter to fiber was considered early in the project, but due to concerns related to its stability under relatively high laser power being transmitted through the fiber, a 'dry' connection method

was ultimately preferred. A photograph of the system components, and of the fiber sample, is reproduced in figure 4.3.

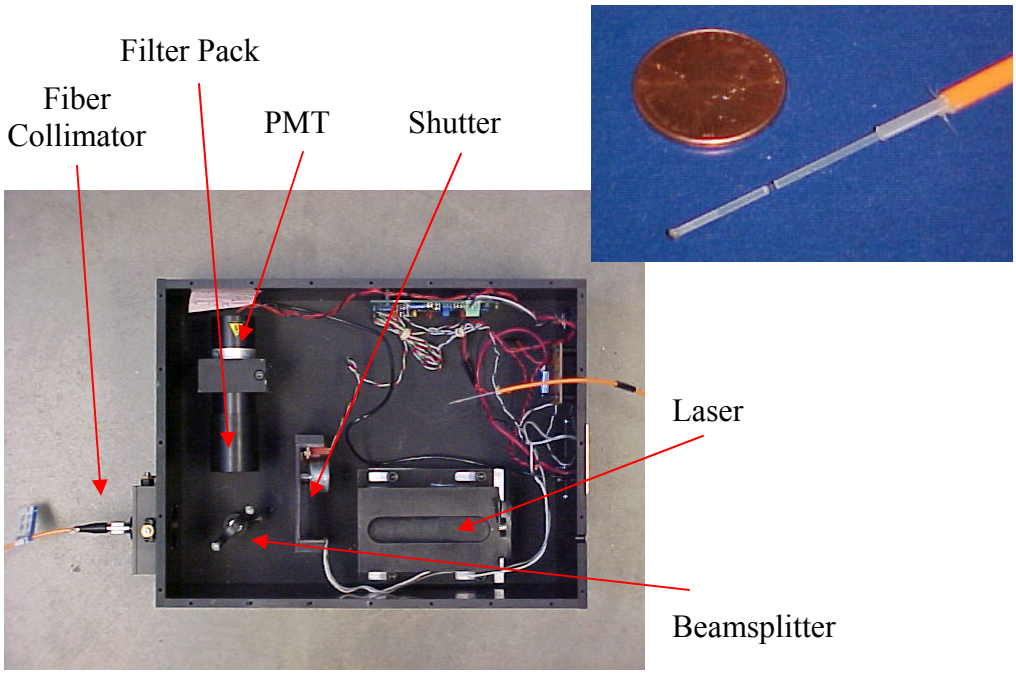

Fig. 4.3: Experimental setup & Al_2O_3:C fiber probe

4.2. Basic OSL properties of the Al_2O_3:C samples

The investigated dosimeters were supplied by the Crystal Growth Division of Landauer, Inc. Single crystal samples grown in fiber-like shapes, and having diameters ranging from $125\mu m$ to $2mm$ were available. For medical dosimetry purposes, the size of the dosimeter has to be a compromise between the smallness required by the comfort of the patient during the procedure and the size necessary to achieve an acceptable sensitivity. It was considered that the study should concentrate on fiber guides / fiber dosimeters with diameters of about $500\mu m$.

Growth processes performed under different conditions resulted in fibers with different OSL properties, in terms of sensitivity, bleachability, and afterglow. The data presented in this thesis were obtained from different samples of Fiber 31 and Fiber 52, the dimensions of which are given in table 4.3.

Sample name	Diameter (μm)	Length (mm)
F31	440	6
F52-1, F52-2	480	5

Table 4.3: Dimensions of the Al_2O_3:C dosimeters

4.2.1 The OSL decay

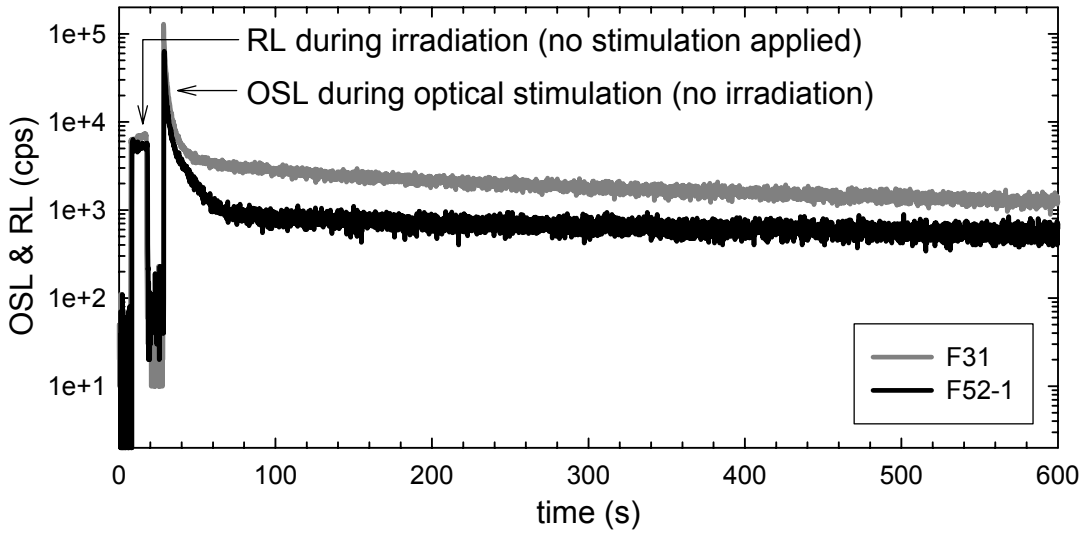

Fig. 4.4: OSL decay curves from F31 and F52-1 after 0.554Gy of β radiation

The signals in figure 4.4 represent traditional OSL decays obtained from both F31 and F52-1. The thoroughly bleached samples were irradiated for 10 seconds, at a dose rate of

55.4*mGy/s*, with β radiation from a ^{90}Sr radioactive source. During irradiation and in the absence of optical stimulation, the samples emitted prompt luminescence (RL). After irradiation, the optical stimulation was turned on, and OSL of a decaying shape was recorded. Figure 4.5 shows in detail the RL signals and the first part of the decays.

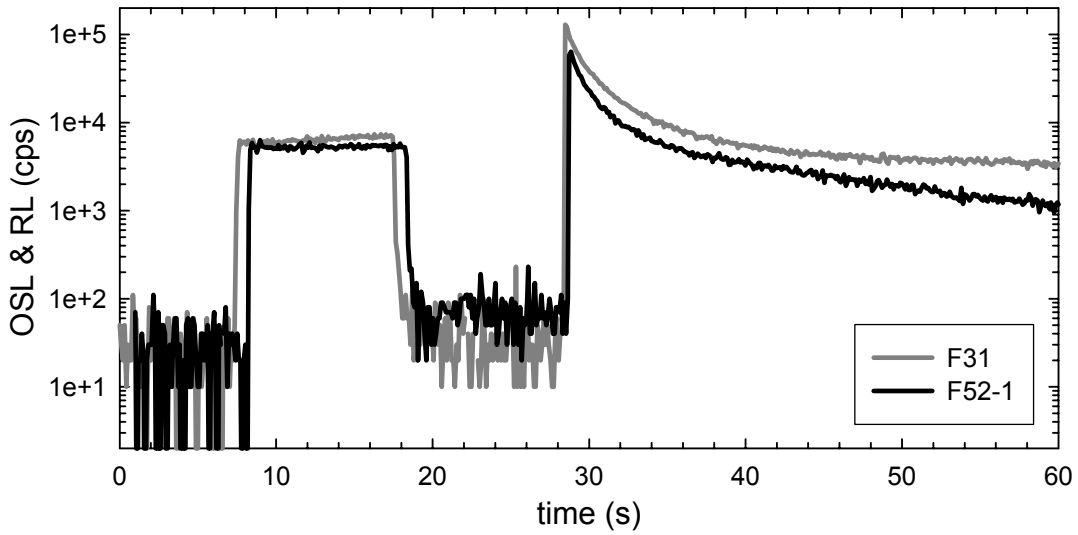

Fig. 4.5: OSL decay after 0.554*Gy* of β radiation – detail

It appears evident that the OSL does not decay exponentially, as predicted by expression (2.4). Our simple mathematical model only considered a single type of defects as potential electron traps. In reality, electrons can be trapped by a multitude of types of defects, which are not equally sensitive to stimulation light. At constant stimulation intensity, optical detrapping of the captured electrons takes places at different rates for different traps, as described by the equations (4.1) and (4.2) for a case in which two optically active traps are present in the material:

$$\frac{dn_1}{dt} = -n_1 \cdot p_1(\lambda)\,;\ p_1(\lambda) = \Phi(\lambda) \cdot \sigma_1(\lambda) \qquad (4.1)$$

$$\frac{dn_2}{dt} = -n_2 \cdot p_2(\lambda);\ p_2(\lambda) = \Phi(\lambda) \cdot \sigma_2(\lambda) \qquad (4.2)$$

Here, the subscripts "1" and "2" refer to the different types of traps, having different photoionization cross-sections σ at the wavelength λ of the stimulation light, and all coefficients refer to the same physical quantities as previously defined.

Solving the equations (4.1) and (4.2) indicates that each type of traps contributes to the total OSL with an exponential signal with a particular decay time. The measured OSL originates in both types of traps, and therefore should be expected to decay as a double exponential. In a more general case, when more than two distinct types of traps are present, a larger number of components will appear in the OSL decay, one for each particular type of trap.

An additional complication is added to the picture by the presence of the so-called shallow traps. The energy levels corresponding to the shallow traps lie close to the lower edge of conduction band. Even at room temperature, there is a significant probability that the trapped electrons will be thermally released, as shown in the equation:

$$p = s \cdot e^{-\frac{E}{kT}} \qquad (4.3)$$

where p is the probability of release, s is a constant with dimensions of inverse time, E is the depth of the trap, k is the Boltzmann constant and T the absolute temperature at which the process takes place. As a result, a slowly decaying luminescence signal known as afterglow or phosphorescence is emitted.

From figure 4.5, it can be noticed that the luminescence background presents an increases in intensity after the irradiation, for both samples. However, the effect is larger for sample F52-1 than for F31. This effect is to be interpreted as phosphorescence, and

indicates a larger relative concentration of shallow traps in sample F52-1 than in F31.

Figure 4.6 shows the results of a similar experiment performed on two samples of Fiber 52, both produced during the same growth run, at a larger irradiation dose rate (uncalibrated). Unlike F52-1, sample F52-2 emits a phosphorescence signal with a visible decaying shape. The experiment is indicative of the large variability in the characteristics of samples obtained during the same growth run, and suggests that the suitability of a sample for RT-OSL use should be determined through individual assessments rather than by bulk characterizations.

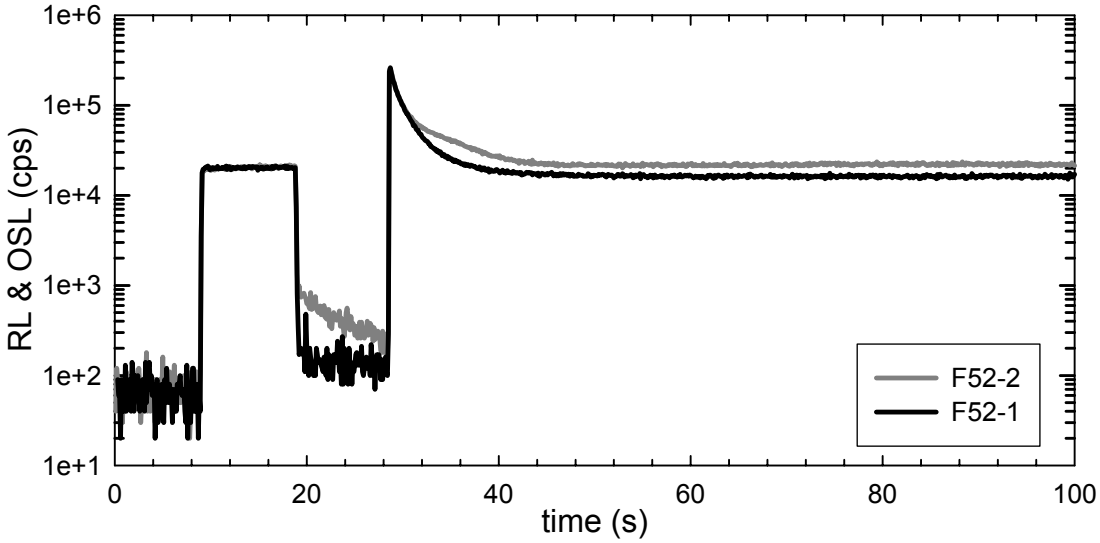

Fig. 4.6: Traditional OSL of different samples of Fiber 52

Another observation that can be made from figure 4.5 is that the RL of F31 presents a slightly increasing trend, at a constant dose rate. This apparent RL 'sensitization' effect occurs as a result of competition effects between different types of traps. In order to explain this effect, we will reconsider the energy-band diagram shown in figure 3.3 (a). We will add to the picture an additional electron trap, which will act as a competitor for

the main trap responsible for OSL. The resulting energy-band diagram is schematically represented in figure 4.7.

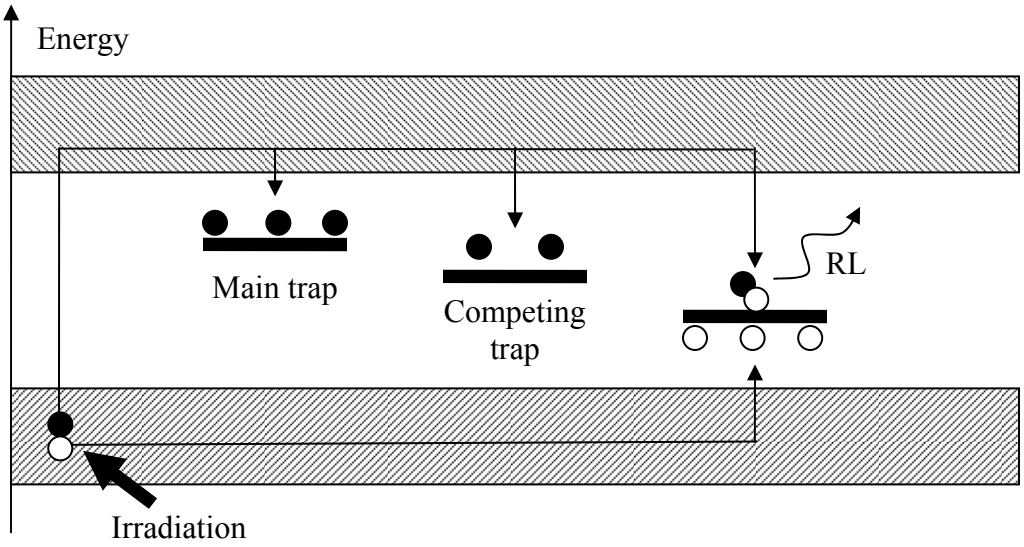

Fig. 4.7: Band diagram showing the main OSL trap and a trap responsible for competition effects

As previously described, during the irradiation, following ionization processes, electrons from the valence band are excited to the conduction band. The rate at which the process takes place is proportional to the irradiation dose rate. Once the electrons reach the conduction band, they lose the excess energy by way of one of the three possible processes shown in fig. 4.7: relaxation on either the main or the competing trap, or direct recombination followed by emission of RL. The relative probabilities at which these three processes take place depend upon the concentration of the charge already trapped at either type of defects. The phenomenon can be mathematically described by a relation of the form (2.1b), for each type of trap.

If electrons choose a particular relaxation path, they do so at the expense of the remaining two. If at the beginning of the irradiation process the competing traps are empty, they will capture electrons at a high rate. Consequently, the number of electrons that will be captured by the main trap and the number of electrons that will directly recombine and emit RL will decrease. Thus, the competition induced by additional traps results in an effective de-sensitization of the luminescence dosimeter, both from the RL and the OSL points of view.

As the competing traps fill up, fewer electrons will get captured by them, and more electrons will relax via the other two paths: trapping at the main OSL trap, or direct recombination leading to emission of RL. Thus, the apparent sensitization indicated by the increase in the level of the RL signal in figure 4.5 represents in fact a decrease in the de-sensitization induced by competition effects.

Also resulted from the presence of multiple types of traps in the material is the presence of a very slow component in the OSL of F31, as shown in figure 4.4. This can be attributed to a type of deep traps which are relatively insensitive to optical stimulation (at the wavelength normally used). Comparing the two samples in figure 4.4, it can be immediately noticed that sample F52-1 reaches must faster an essentially constant background, and thus it can be concluded that it presents a smaller concentration of deep traps than its predecessor F31.

4.2.2. Traditional OSL dose response

The OSL dose response for F31 and F52-1 is shown in figure 4.8. At large doses, both fibers show supralinear responses. Similarly to the increase in RL sensitivity, the

supralinearity of the dose response should be attributed to a decrease in competition, as the competing traps get filled.

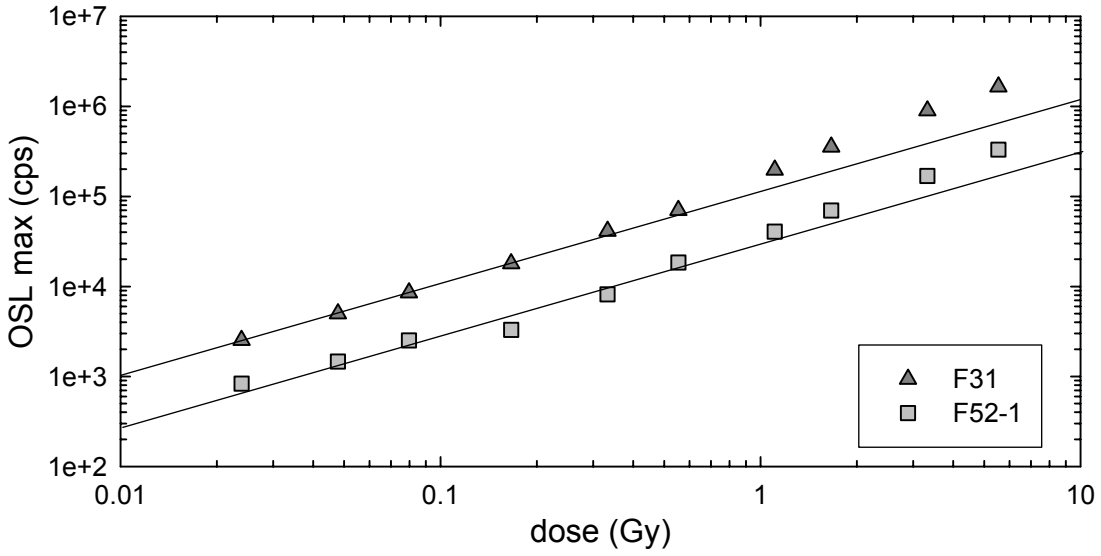

Fig. 4.8: Traditional OSL dose response from F31 and F52-1

There is an apparent discrepancy between the data shown in figures 4.4 and 4.8, respectively. We concluded from the shape of the OSL decays in figure 4.4 that F31 had contained a larger concentration of deep traps than F52-1. However, we cannot extract the same conclusion from the data in figure 4.8, where both fibers show a comparable degree in supralinearity, suggesting a comparable amount of competition effects.

The answer can be given in terms of the optical activity of different types of traps: sample F52-1 might contain a concentration of deep traps comparable to F31; however, the deep traps in F52-1 are much less responsive to optical stimulation than the deep traps of F31. Thus, the slow component noticed in the OSL decay of F31 appears as an essentially constant background in the OSL of F52-1.

4.2.3. Delayed OSL

During an RT-OSL experiment, the laser light used to stimulate the OSL from the Al_2O_3:C fiber dosimeter is modulated while the sample is being irradiated. It has been noticed that after the stimulation is abruptly turned off ($\tau<1ms$) the OSL signal fades away slowly, with a lifetime much larger than the lifetime of the recombination center ($35ms$ in Al_2O_3:C). The slowly-decaying signal is known as 'delayed OSL' (DOSL), and occurs due to the presence pf shallow traps in the material. When stimulation light ionizes the electrons to the conduction band, a fraction of them will be captured on shallow traps, instead of radiatively relaxing at the recombination center. They will subsequently be thermally released, and thus a slow phosphorescence-type of luminescence signal will be emitted by the sample even after optical stimulation ceases.

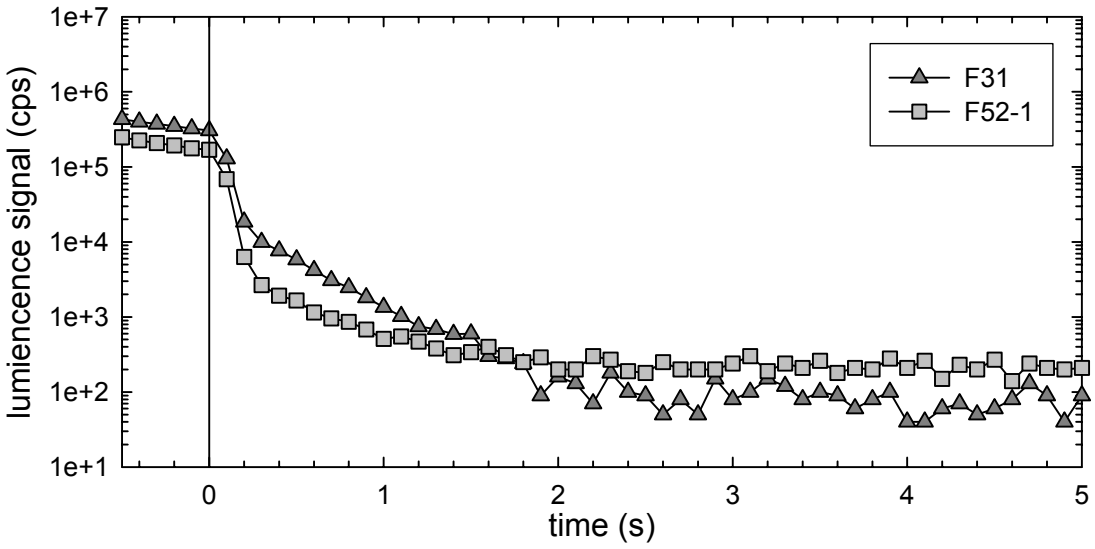

Fig. 4.9: Delayed OSL from samples F31 and F52-1, irradiated at 55.4*mGy*/*s*

Figure 4.9 contains DOSL measured from the samples F31 and F52-1. The experiment

was performed under β irradiation at a dose rate of 55.4mGy/s. The samples were irradiated in order for the trap population to build up, and then were optically stimulated for brief periods of time. At the moment $t = 0$ the laser stimulation was turned off. The OSL-to-RL transition extends over a period of time of about 2 seconds.

DOSL represents one of the most important factors limiting the speed of the real-time OSL measurements. The delayed OSL needs to completely fade away before the next background luminescence measurement is performed. Otherwise, the measured RL will be larger than the real RL by an amount corresponding to the DOSL intensity integrated over the respective time interval. Accordingly, the parameters of the growth process need to chosen so that the concentration of shallow traps be kept to a minimum.

4.3. Real-time OSL (RT-OSL)

A short recapitulation of the known aspects of RT-OSL will prove useful at this point.

According to the simple theory developed in chapter 2, the OSL from a sample being irradiated should behave like a sum of an exponential decay and an exponential rise to the maximum. Both exponentials should have the same characteristic time τ, dependent on both the stimulation power, which can be held constant during the experiment, and on the irradiation dose rate. If the sample is initially bleached, than the RT-OSL will have the shape of an exponential rise to a maximum. In this case, the coefficient K_S can be immediately obtained as a function of the exponential constant τ and other parameters describing the timing of the experiment, from a simple mathematical analysis involving the integration of the OSL signal over successive time intervals.

With a known K_S, we would be able to use the algorithm described in chapter 3 to

determine the dose absorbed between successive stimulations.

At this point we are facing a circular dilemma: the dose rate is needed to predict K_S, but K_S is needed to calculate the dose rate.

Fortunately, relation (3.8) suggests that the dependence of K_S with the dose rate can be minimized by using a high enough laser power. However, at this point, we do not have any indication about the stimulation intensity that would allow us to reasonably approximate K_S as a dose-rate-independent parameter.

Also, from the previous sections in this chapter, we know that the shape of OSL is given by an overlapping of multiple components.

In the next sections, we will look for a possibility to predetermine the value of K_S. This investigation will try to answer two different questions:

i. Can each component' characteristic time τ be considered independent of the dose rate $\dot{D}$?
ii. Does the relative intensity of the different components in the total OSL signal remain constant during the experiment?

Both of the above questions have to be answered affirmatively in order for us to be able to predict the value of K_S, and subsequently use it to determine the dose / dose rate from the step-by-step algorithm described in chapter 3.

4.3.1. The theoretical model revisited

If an initially bleached sample ($n_0 = 0$) is simultaneously irradiated and optically stimulated, equation (2.13) predicts the shape of the RT-OSL as an exponential increase

to a maximum:

$$I_{OSL}(t) = C \cdot Np \frac{r}{r+p}\left[1 - e^{-(p+r)t}\right] \tag{4.4}$$

The intensity level eventually reached by the luminescence signal will be denoted as the 'Equilibrium intensity' $I_{OSL}(\infty)$, and will be dependent on the concentration of available traps N, the laser power and the dose rate. For a given sample, and under constant optical stimulation, the equilibrium intensity will be proportional to the dose rate, through the parameter r.

$$I_{OSL}(\infty) = C \cdot \frac{N \cdot p \cdot r}{r+p} \tag{4.5}$$

If two kinds of optically active traps are present in the material, the OSL will not rise to the maximum level as a single exponential, but as a sum of two exponentials.

$$I_{OSL}(t) = C \cdot N_1 p_1 \frac{r_1}{r_1 + p_1}\left[1 - e^{-(p_1+r_1)t}\right] + C \cdot N_2 p_2 \frac{r_2}{r_2 + p_2}\left[1 - e^{-(p_2+r_2)t}\right] \tag{4.6}$$

The parameters p and r will be proportional to the laser power P and dose rate $\dot{D}$, respectively, with different constants of proportionality for each component:

$$p_1 = \alpha_1 \cdot P\,,\ r_1 = \beta_1 \cdot \dot{D} \tag{4.7a}$$

$$p_2 = \alpha_2 \cdot P\,,\ r_2 = \beta_2 \cdot \dot{D} \tag{4.7b}$$

The equilibrium intensity will be then given by:

$$I_{OSL}(\infty) = C \cdot \left[\frac{N_1 \cdot p_1 \cdot r_1}{r_1 + p_1} + \frac{N_2 \cdot p_2 \cdot r_2}{r_2 + p_2}\right] \tag{4.8}$$

An equivalent form for expression (4.8) is

$$I_{OSL}(\infty) = C \cdot \left[N_1 \frac{r_1}{1+\frac{r_1}{p_1}} + N_2 \frac{r_2}{1+\frac{r_2}{p_2}} \right] \tag{4.9}$$

For sufficiently high stimulation intensity, and for dose rates not exceeding a certain value, the following approximation can be made:

$$\frac{r_1}{p_1} << 1 \quad \Rightarrow \quad 1+\frac{r_1}{p_1} \to 1 \tag{4.10a}$$

$$\frac{r_2}{p_2} << 1 \quad \Rightarrow \quad 1+\frac{r_2}{p_2} \to 1 \tag{4.10b}$$

Substituting (4.10) in (4.9), we get

$$I_{OSL}(\infty) = C \cdot \left(N_1 \cdot r_1 + N_2 \cdot r_2\right) = C \cdot (N_1 \cdot \alpha_1 + N_2 \cdot \alpha_2) \cdot \dot{D} \tag{4.11}$$

We now have two possible methods for obtaining the relative magnitudes of the r and p coefficients. One of them would be to fit RT-OSL curves obtained at different dose rates with sums of exponentials of the form (2.13). Then, the dose rate dependence of the fitted values of the characteristic times of the exponentials could be obtained. However, the presence of multiple components will induce a large degree of uncertainty in the results. Alternatively, as suggested by equation (4.11), we could consider the function relating the OSL equilibrium intensity with the dose rate, i.e., the dose rate response of the equilibrium intensity $I_{OSL}(\infty)$. According to expression (4.11), a low degree of sublinearity in the function $I_{OSL}(\infty) = f(\dot{D})$ would confirm the validity of approximation (4.10), regardless of the number of individual components with different decay times that show up in the OSL curve.

4.3.2. Estimation of the relative value of the *r* and *p* parameters

The function $I_{OSL}(\infty) = f(\dot{D})$ was obtained by recording the RT-OSL of F52-1 at three different dose rates, previously calibrated as 7.97, 55.4 and 177mGy/s. Before each experiment, the sample was bleached for extended periods of time, in order to deplete the deep trap population to a maximum. While the sample was irradiated, stimulation light modulated by a square-wave signal was applied to the dosimeter. During the time intervals the stimulation was turned off, the RL was measured. Stimulation light was then turned on, and a luminescence signal containing both the RL and the OSL intensity was detected at the PMT. By subtracting the former signal form the latter, the OSL signal alone was isolated. As shown in figure 4.10, the RT-OSL signals have the general shape of a rise to a maximum, as predicted by relation 4.6.

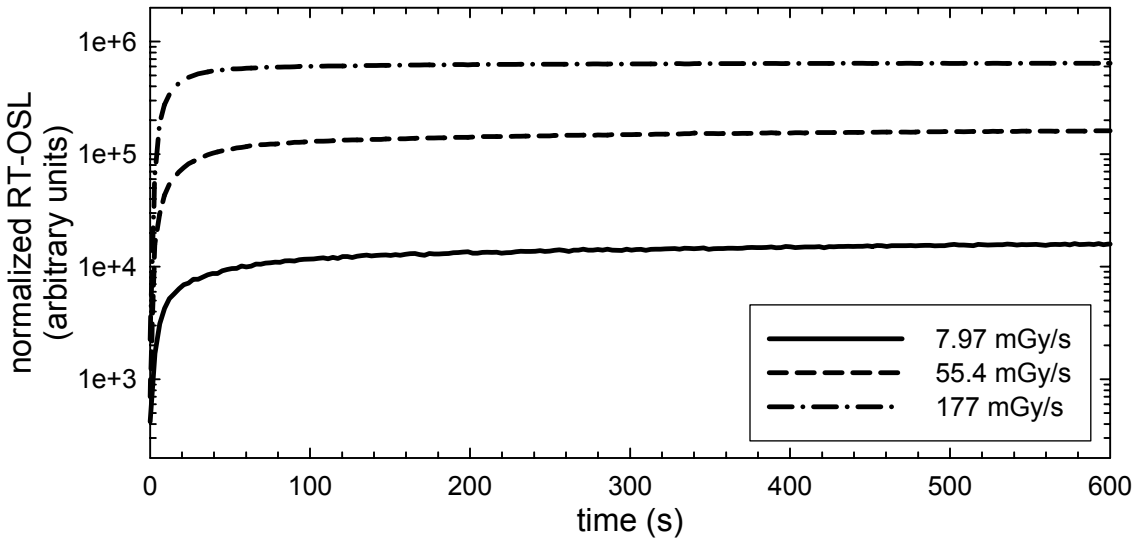

Fig. 4.10: RT-OSL from initially bleached F52-1, at different dose rates

The equilibrium intensity was calculated as the average of the last 10 OSL measurements

at each dose rate, and was represented as a function of the dose rate at which the irradiation is performed in figure 4.11.

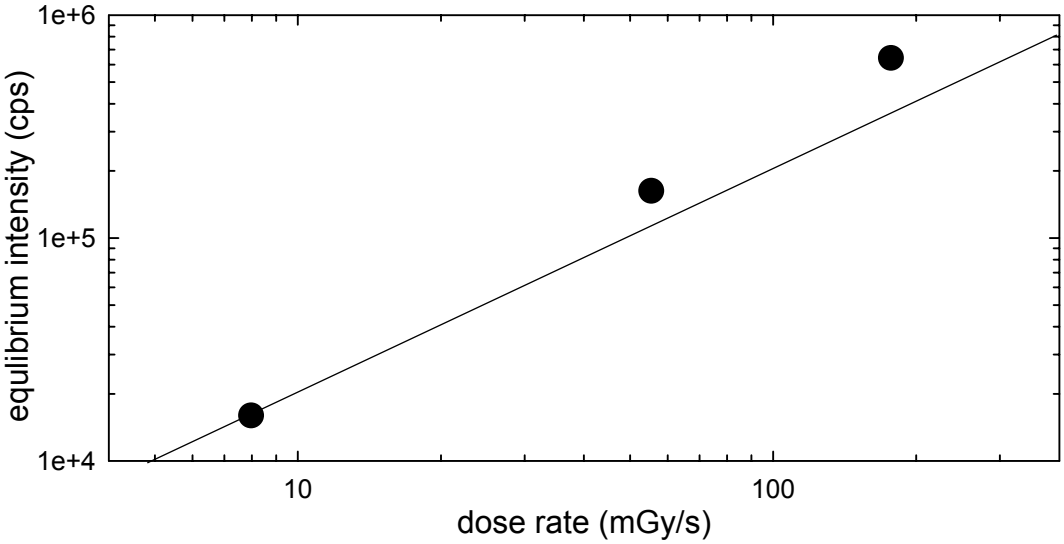

Fig. 4.11: The equilibrium intensity $I_{OSL}(\infty)$ as a function of dose rate

The sublinear behavior suggested by (4.9) cannot be seen in the experimentally-obtained shape of $I_{OSL}(\infty) = f(\dot{D})$. Oppositely, the function shows a certain degree of supralinearity, which can be attributed to the supralinearity in the dose response of F52-1. We can now give an affirmative answer to the first question raised in the beginning of section 4.3. Since experimental data seem to confirm the validity of approximation (4.10), it safe to affirm that does rate variations within the investigated range affect only slightly the shape of the individual exponential components.

4.3.3. Mixing of different components in the OSL signal

The next question we have to answer to is related to the relative magnitudes of the

different components forming the OSL signal. The RT-OSL curves from figure 4.10, normalized to their maximum intensity, are represented in figure 4.12.

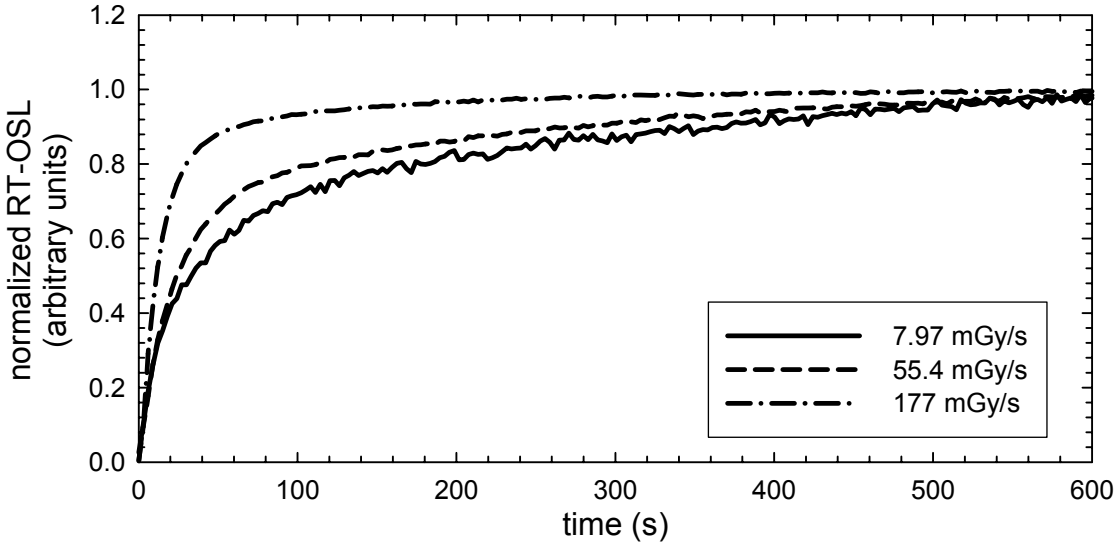

Fig. 4.12: Normalized RT-OSL from F52-1, at different dose rates

The OSL curves have different shapes, showing a tendency toward steeper rises to the maximum value with increasing dose rate.

According to the results from the previous section, the differences in shape come from different magnitudes of the components, rather than from intrinsic differences in their individual shapes. Therefore, our assumption is that irradiating the same sample at two different dose rates would lead to a different mixing of the components in the OSL signal. In an attempt to verify this statement, relation (4.6) was used to simulate the OSL rise to maximum in two different cases, given by the two different sets of parameters indicated in table 4.4.

The parameters were chosen in order to reflect a 5 times decrease in the dose rate at

which a sample is irradiated. According to our previous findings, the parameters r and p also have to satisfy the constraint $r << p$. The parameters describing the available trap concentrations in the sample and the stimulation intensity were kept at the same value in both calculations.

parameter	N_1	p_1	r_1	N_2	p_2	r_2
Set 1	100000	0.05	0.001	50000	0.02	0.005
Set 2	100000	0.05	0.0002	50000	0.02	0.001

Table 4.4: Parameters of the double exponential RT-OSL simulation

The normalized OSL signals are represented in figure 4.13 (a). The time evolution of the ratio of the OSL components is plotted in figure 4.13 (b). The preferential build-up of the slow component predicted at both dose rates can be explained by a lower bleaching efficiency for the corresponding type of traps. This leads to a gradual increase in the 'slow trap' population, and thus an increase in the intensity of the slow component.

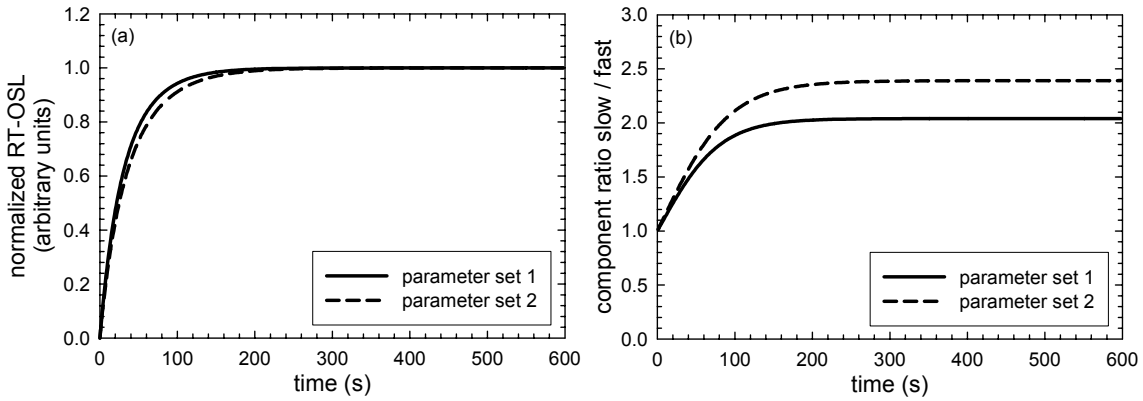

Fig. 4.13: Simulation result showing different mixing of the exponential components of the RT-OSL signal

Even during irradiations at the same dose rate, the shape of the RT-OSL is expected to vary according to the sample history. The graph in figure 4.14 shows the RT-OSL measured for the sample F52-1 being irradiated with a β dose rate of 55.4*mGy*/*s*. Prior to the first irradiation, the sample was bleached for a time interval longer than 1 hour. The second OSL measurement is taken after a short bleaching on the order of a few minutes.

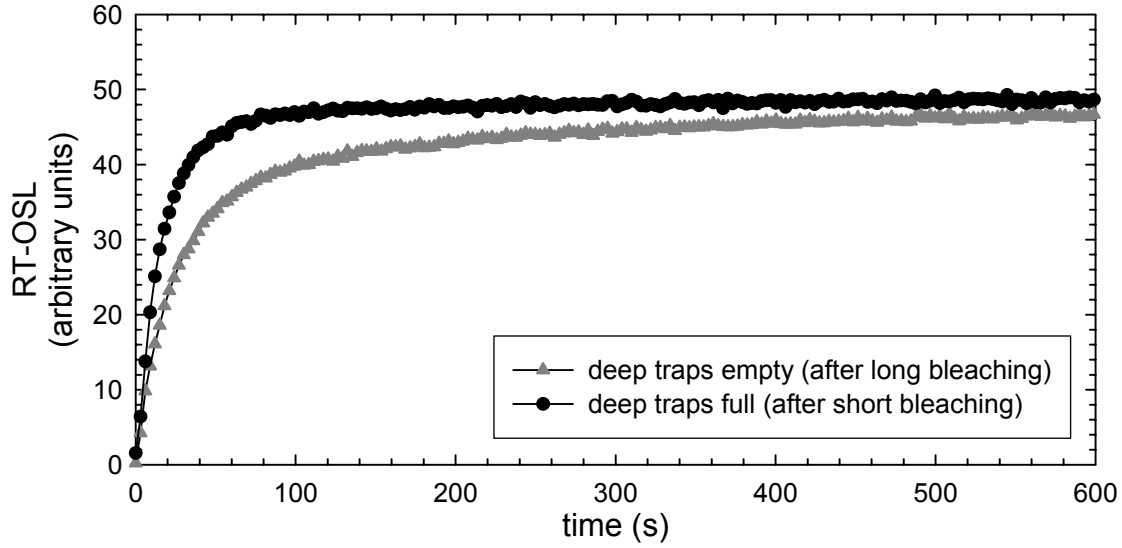

Fig. 4.14: Different RT-OSL shapes given by different sample history

The time needed by the RT-OSL signal to reach the equilibrium intensity $I_{OSL}(\infty)$ increases with the duration of the previous bleaching. Like in the case of RL, the gradual sensitization is the result of a decrease in competition as the 'slow trap' trapped electron population grows.

After short bleaching only, the competing traps are already filled at the beginning of the experiment, and the population of the fast component quickly reaches the equilibrium level.

We can now answer the second question regarding the shape of the RT-OSL.

The relative intensity of the different OSL components changes between different experiments, as well as during a single experiment. The time evolution of the component mixture is difficult to predict, and it is dependent on the irradiation dose rate and sample history.

4.3.4. Simple correction using a constant shape coefficient K_S

In the next step, we will try to estimate the errors that would be induced by using a constant shape coefficient K_S in the algorithm described earlier, applied on the data from figure 4.14. Figure 4.15 (a) presents the dose rate – understood as the dose delivered between successive stimulations divided by the time between stimulations - calculated with $K_S = 0.83$. The particular value of K_S was chosen so that a constant value of the dose rate would be obtained from the data collected in the second RT-OSL measurement (following short bleaching) in figure 4.15 (a).

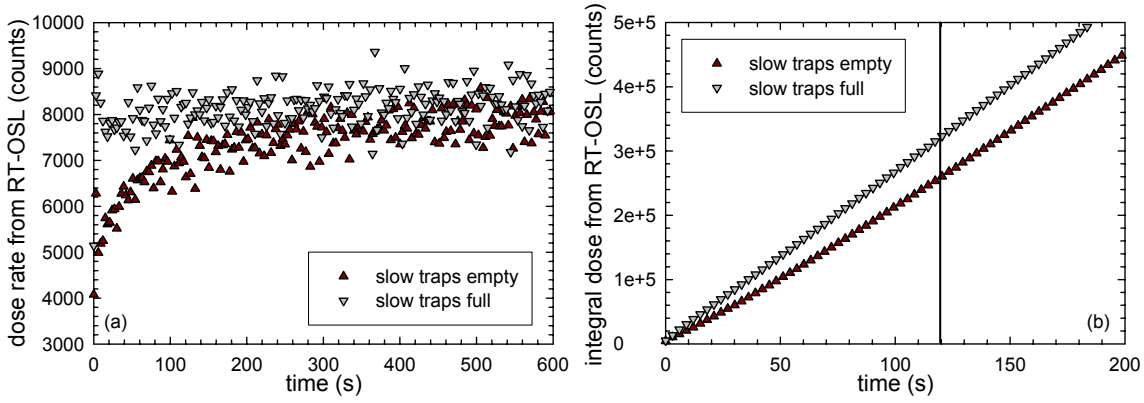

Fig. 4.15: Results of the simple (constant K_S) correction performed on the data from figure 4.14: (a) average dose rate and (b) integral absorbed dose

The time evolution of the dose rate calculated from the first OSL signal (slow traps empty) with the same K_S results in an obviously incorrect shape, indicating a false gradual increase of the doses absorbed between pairs of successive stimulations.

The total dose can be estimated by adding all the fractional doses up to a given moment of time. An equivalent statement would be that the data points represented in figure 4.15 (a) represent the local slopes of the two functions describing the evolution of the integral dose with time. The integral dose calculated from the two data sets in 4.15 (a), is represented as a function of time in figure 4.15 (b).

The error in the estimation of the integral dose delivered after the first 120*s* of the procedure (comparable in terms of dose rate and irradiation time with a typical radiotherapy irradiation) accumulates to a value of 20%, totally unacceptable for medical dosimetry.

4.3.5. Controlled depletion approach

In this section, we will present the results obtained from the implementation of the modified Creager procedure, as presented in section 3.3 of this thesis.

The outline of the procedure follows:

i. This procedure involves depleting the OSL signal from the Al_2O_3:C dosimeter to the maximum possible extent.
ii. As justified in section 3.3, the OSL integration time needs to be short. Values normally used are on the order of 100*ms*.
iii. Maximum depletion does not mean total extinction of the OSL signal. As shown by relation (2.13), in the case of simultaneous irradiation and optical stimulation,

the OSL signal eventually reaches a constant value, proportional to the irradiation dose rate.

iv. It is possible, if the initial trap population of the sample is low enough, that the OSL signal will not have a decaying shape, but rather an increase to a maximum. As in the case of the OSL depletion, the OSL signal reaches the same constant value, proportional to the irradiation dose rate.

As a consequence of (iii.) and (iv.), we need to restate (i.) as:

v. The procedure involves allowing the OSL signal to reach the equilibrium value corresponding to the particular dose rate at which the irradiation takes place.

vi. Then, the newly added dose fraction has to be calculated NOT as being proportional to the OSL signal, but rather to the increase in the OSL signal, as compared to the last measured value of the equilibrium level $I_{OSL}(\infty)$.

An alternative, but equivalent justification for employing this procedure is given by relation (3.11)

$$D = \frac{I_1' - I_1}{S} = \frac{I_1' - K_S \cdot I_0}{S} \tag{3.11}$$

for the special case

$$K_S \to 1 \tag{4.12}$$

when (3.11) becomes

$$D = \frac{I_1' - I_0}{S} \tag{4.13}$$

In order to apply this procedure, we needed to devise a criterion indicating the completion of the OSL depletion (or build-up) process. Therefore, during the entire duration of optical stimulation, the luminescence signal containing the sum of RL and

OSL is continuously recorded, as a series of data points representing the luminescence integrated over short time intervals (on the order of 100*ms*). As the luminescence approaches the equilibrium level, the local slope determined dynamically from the most recently measured points of the OSL curve approaches a value of 1. In order to minimize the experimental errors the local slope is typically determined from the last 5 points of the OSL curve. When the local slope reaches a value situated sufficiently close to 1, the stimulation is turned off and, as a result of the continued irradiation, the trap population increases.

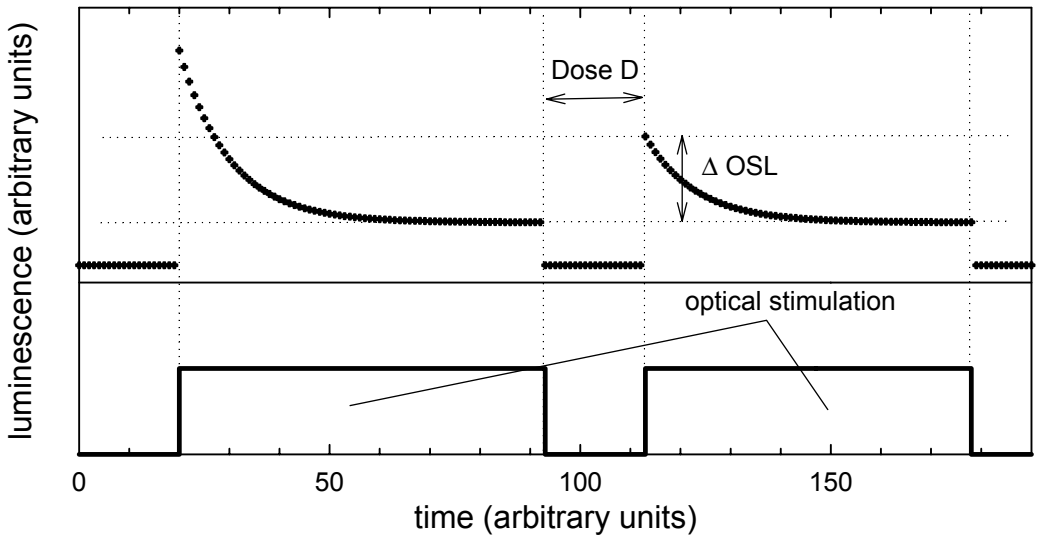

Fig. 4.16: Pictorial description of the controlled depletion procedure

After a certain amount of time with no stimulation applied to the sample (typically 3*s*), the laser is turned on, and the dose absorbed during the laser-off interval is determined by the increase in the OSL signal Δ_{OSL} incurred between the last OSL data point in the previous decay and the first OSL data point in the current data set.

Since the RL is measured during the laser-off time intervals, and is subtracted from the following data points measured with applied optical stimulation, the dose estimations are performed only from the OSL part of the luminescence signal. Thus, the stem effect does not affect the precision of the measurement.

The procedure, graphically described in figure 4.16, has been incorporated in a LabVIEW virtual instrument (VI). A snapshot of the user interface of the VI is shown in figure 4.17.

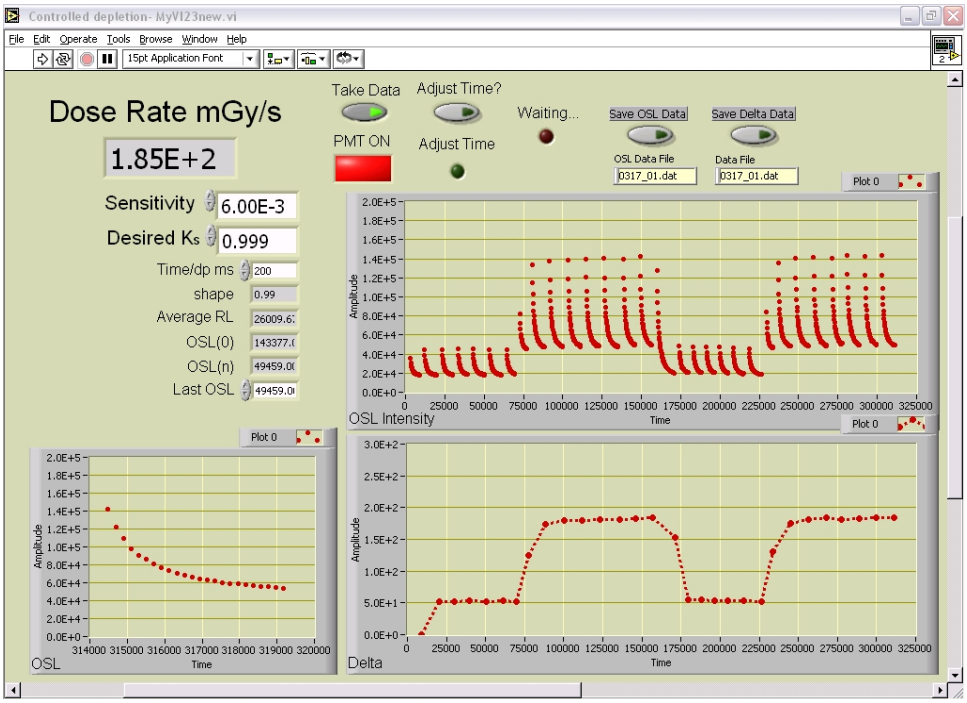

Fig. 4.17: User interface of the controlled depletion VI

For this particular experiment, the desired slope of the OSL was set at 0.999. During stimulation, the OSL intensity is integrated over 200*ms* time intervals, resulting in a sampling frequency of about 5*Hz*.

The sample used was F52-1, attached to a 5*m*-long ESKA cable (diameter 0.5*mm*). The dose rate was switched between the values of 55.4 and 177*mGy*/*s*. The dose absorbed

between successive stimulations, calculated as the increase in the OSL signal, is plotted as 'Delta' on the front panel of the VI as a function of time (in *ms*). It can be noticed that Δ_{OSL} promptly reaches the new value after changing the dose rate. The average time interval needed for the acquisition of 1 dose data point can be estimated from the graph as approximately 10 seconds.

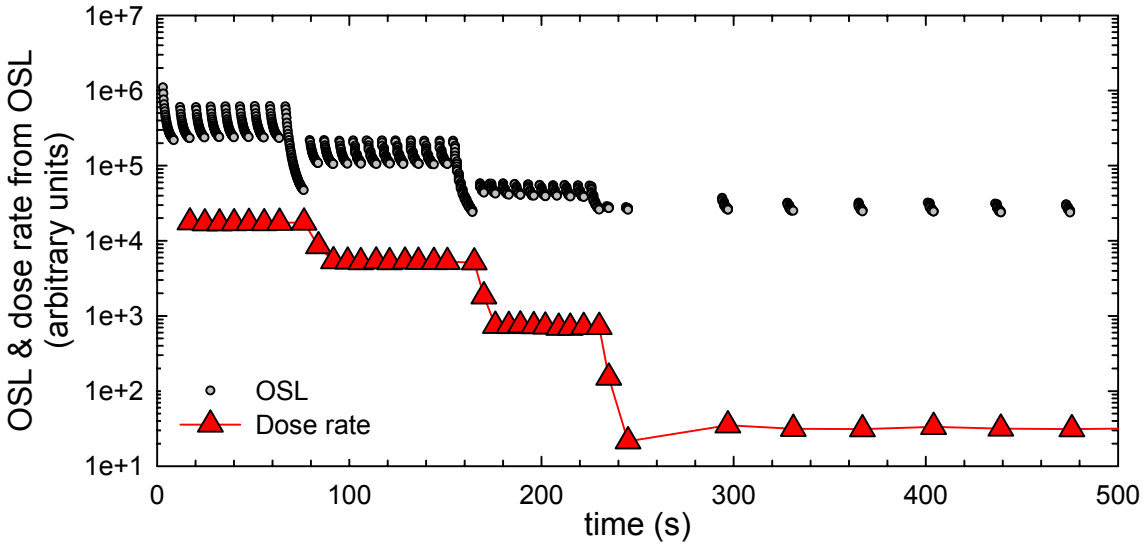

Fig. 4.18: Controlled depletion experiment performed on F31

In order to increase the precision of the measurements at low dose rates, the irradiation (laser-off) time is automatically increased in the case the previous reading returns a value situated below a certain limit. This ensures that, at low irradiation dose rates, the increase Δ_{OSL} in the OSL signal has a high enough value to allow an accurate estimation of the absorbed dose.

Experimental data are shown in figure 4.18. The sample F31 was irradiated in a 250*mCi* ^{90}Sr β source, at dose rates extending over three orders of magnitude: 177, 55.4, 7.97 and

0.344mGy/s. The time between successive stimulations was set at 3s, and increased by a factor of 10 (to 30s) at the lowest dose rate.

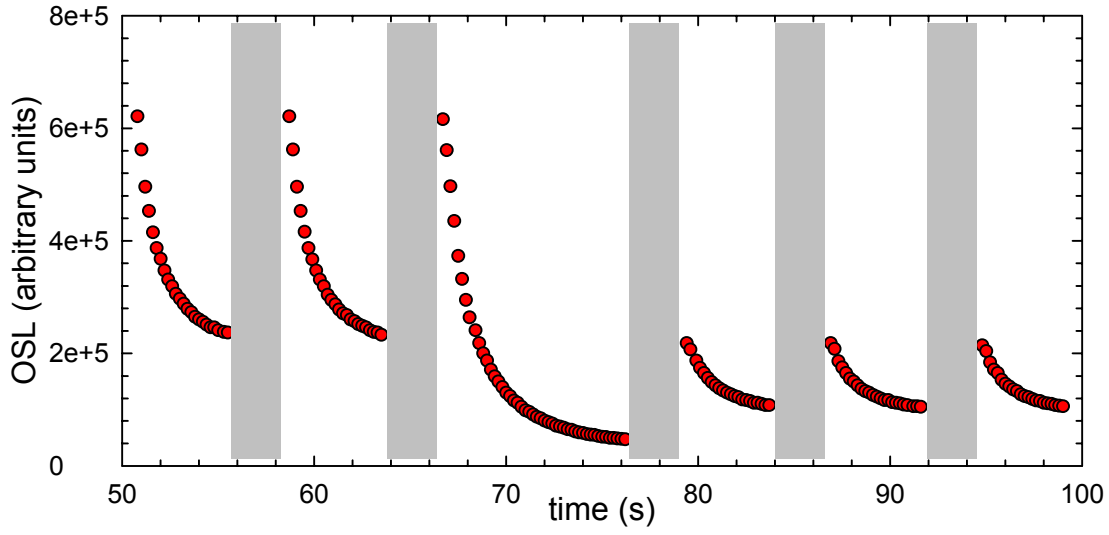

Fig. 4.19: Detail of the controlled depletion experiment showing variability in the depletion time induced by a dose rate transition

As a consequence to terminating each stimulation when OSL reached a particular shape, the depletion time varied, especially when transitions between dose rates occur. The phenomenon is visible in figure 4.19, which represents a detail of the data in 4.18, corresponding to the transition from $\dot{D} = 177 mGy/s$ to $\dot{D} = 55.4 mGy/s$. Also represented in figure 4.19, as shaded areas, are the 3-seconds time intervals when the trap population of the dosimeter is increasing proportionally to the absorbed dose.

The good linearity of Δ_{OSL} calculated from the signal in fig. 4.18 and the actual dose rate is shown in figure 4.20. The 'dose rate from OSL' data points in fig. 4.20 were calculated as the average of all the fractional doses estimated during irradiation at a given dose rate

(the red triangles in fig. 4.18), with the exception of the transitional points caused by non-abrupt transitions in the dose rates. The standard deviation of the sets of measurements corresponding to different dose rates was found to lay in the 1.07% to 4.45% range, with the larger errors corresponded to smaller dose rates.

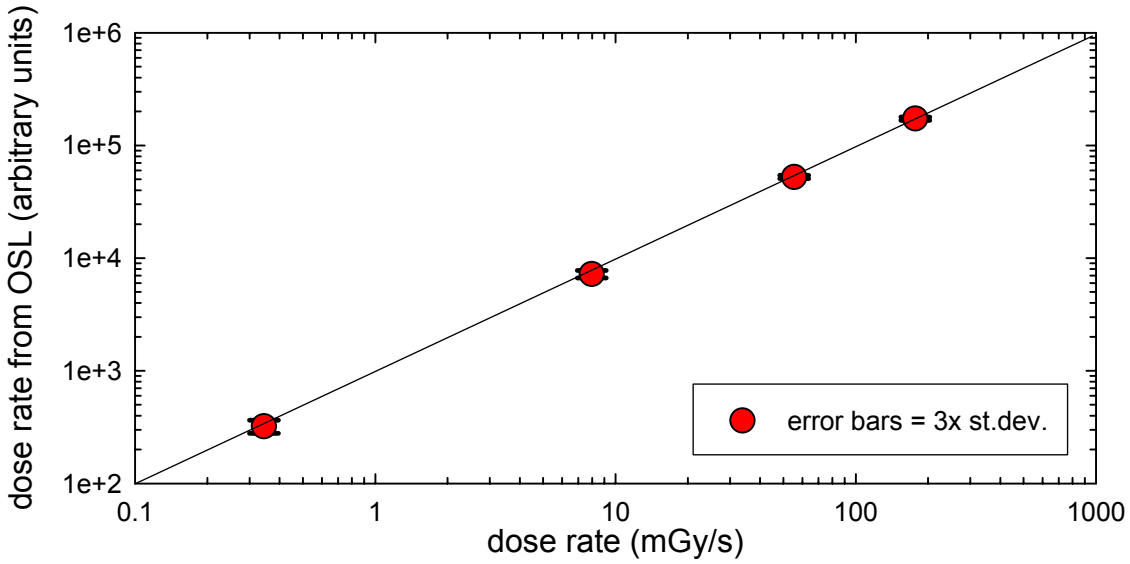

Fig. 4.20: Dose rate response of F31 under the controlled depletion algorithm

4.3.6. Estimating the shape coefficient K_S from direct measurements

The 'controlled depletion' approach is resulted from modifications performed on Creager's initial concept, as described in section 3.3 of the previous chapter. The main limitation of the method is presented by having to completely bleach the OSL from the sample. The next step, presented in section 3.4, and consisting in estimating the newly absorbed dose fraction following an incomplete depletion of the OSL signal, poses the important difficulty of determining the right value of the shape coefficient K_S.

In this section we will investigate a new approach in determining the value of K_S:

instead of trying to predict a value for the shape coefficient, we will try to obtain its value from direct measurements on the shape of the OSL signal.

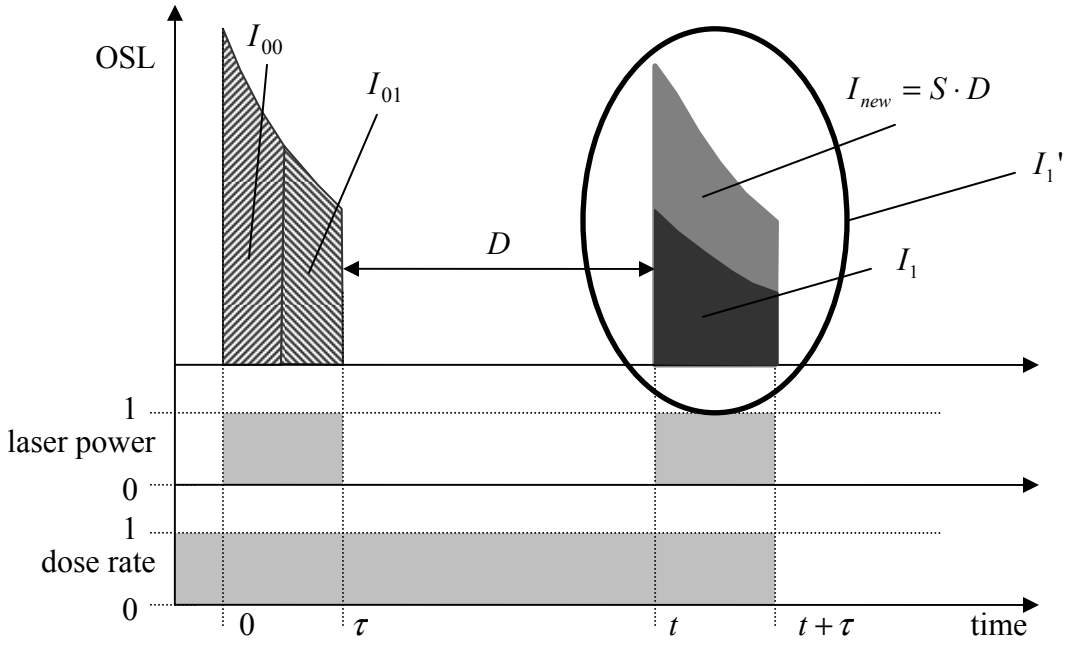

Fig. 4.21: Measuring principle of the shape coefficient K_S

The principle is represented in figure 4.21, which differs only slightly from fig. 3.6. Initially, one data point denoted as I_0 was obtained by integrating the OSL over the whole duration of the laser stimulation. Now, the OSL will be separately integrated over both $\tau/2$ halves of the stimulation interval, to obtain two data points I_{00} and I_{01}.

It is evident that I_0 can be obtained as the sum of I_{00} and I_{01}:

$$I_0 = I_{00} + I_{01} \tag{4.11}$$

Additionally, information about the shape of the decay can be obtained in the form of the

surrogate shape coefficient K_S', defined as:

$$K_S' = \frac{I_{01}}{I_{00}} \tag{4.12}$$

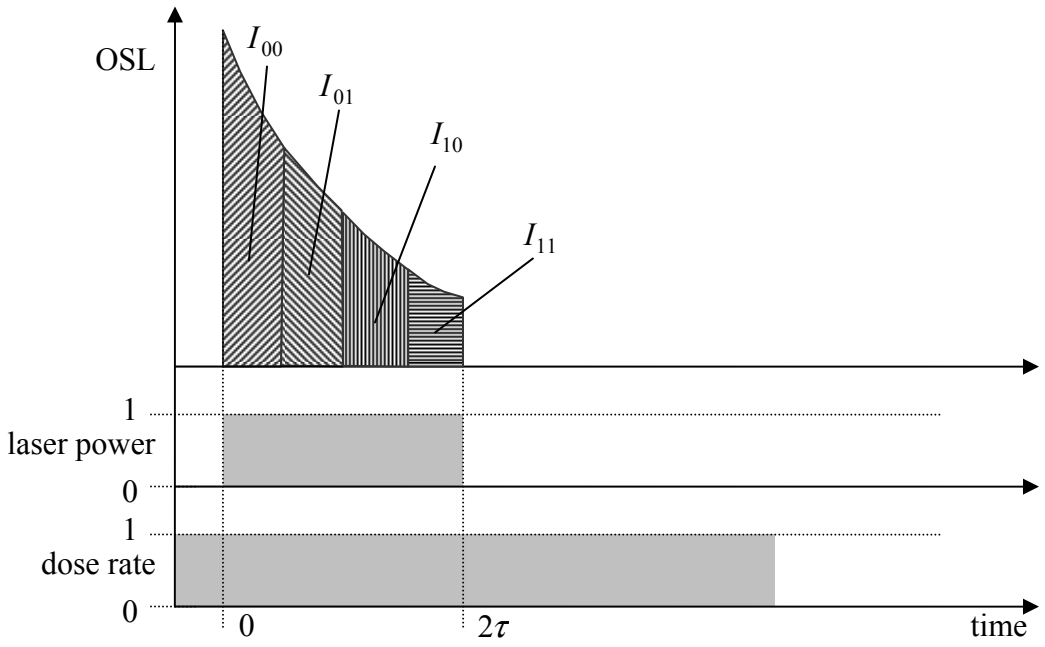

Fig 4.22: Experiment used for determining the function relating K_S and K_S'

For a single exponential decay, K_S can be obtained straight forward from K_S' via

$$K_S = (K_S')^2 \tag{4.13}$$

For the real case of a multiple exponential decay, the function connecting the two shape coefficients was empirically determined from experimental data. The experiment was performed by stimulating the OSL from a sample for an amount of time equal to 2τ - twice the stimulation interval used in the real RT-OSL experiment. The stimulation interval was split into 4 equal periods of time $\tau/2$, and 4 corresponding OSL data points

were measured, as described in figure 4.22.

In this experiment, both K_S and K_S' could be calculated from the measured OSL signals, according to (4.12) and

$$K_S = \frac{I_{10} + I_{11}}{I_{00} + I_{01}} \tag{4.14}$$

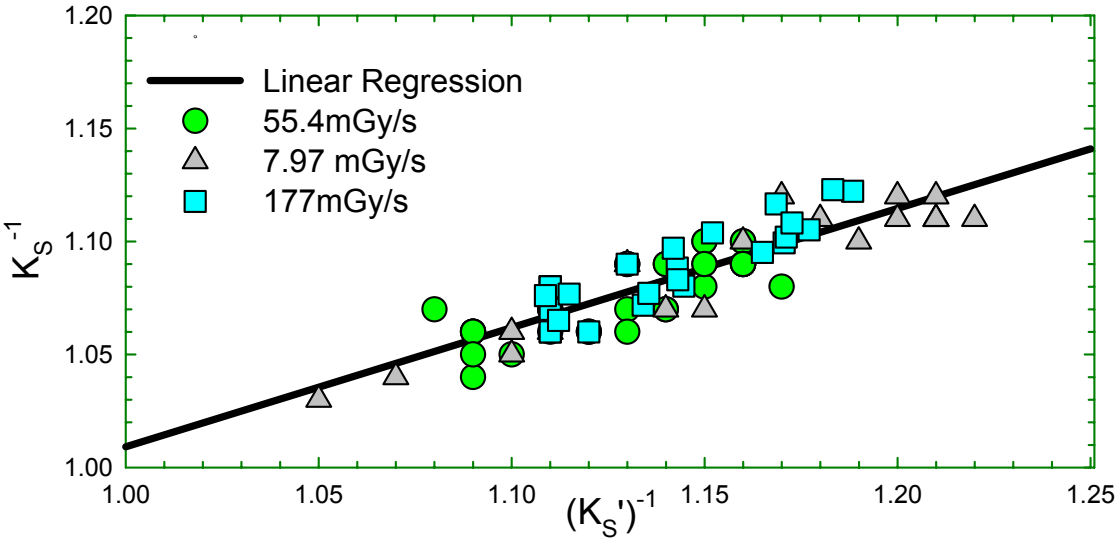

Fig. 4.23: Correlation between the two shape coefficients K_S and K_S'

The sample was irradiated for random amounts of time between the successive stimulations of duration 2τ in order to obtain a broad distribution of the OSL shapes. Different sets of data were taken for irradiations at different dose rates, and they were plotted in figure 4.23:

The graph indicates a linear dependence between the inverses of the two shape coefficients considered, of the form

$$K_S^{-1} = a + (K_S')^{-1} \cdot b \tag{4.15}$$

The two free parameters a and b of the linear dependence have been empirically calibrated to obtain the best correlation between the calculated and the actual dose rates.

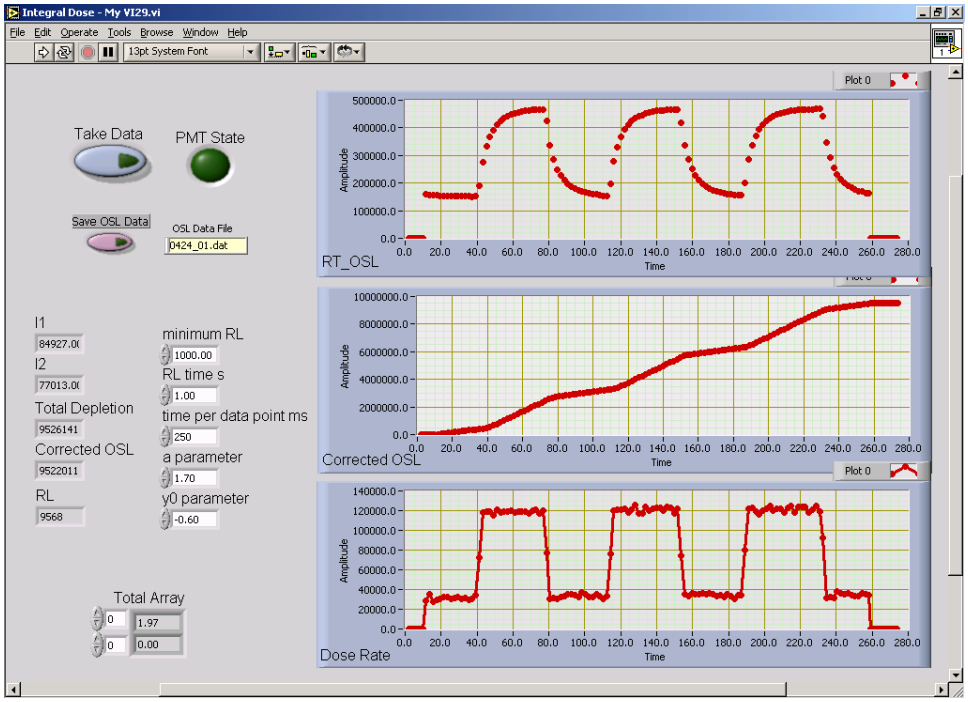

Fig. 4.24: Front panel of the 'variable shape coefficient' VI

The front panel of the VI employing the 'variable shape coefficient' algorithm is given in figure 4.24. The OSL is measured for two successive time intervals of 250*ms* each. From their ratio, K_S' is obtained. Then, with the known a and b values, K_S is obtained, and the algorithm described in chapter 3 is carried on. The evolution of the OSL signal, integral dose and dose rate from RT-OSL are all plotted in real-time. The time needed for obtaining 1 dose rate data point is approximately 3 seconds, depending on the DOSL fading speed in the particular sample.

An additional feature is presented by an automated On/Off switch, which prevents the

overbleaching of the sample in the absence of irradiation. When the program is running, the level of the background luminescence (RL) is continuously monitored. Optical stimulation is only applied when the measured RL exceeds a pre-set level (100*counts*/*data point*, in this case).

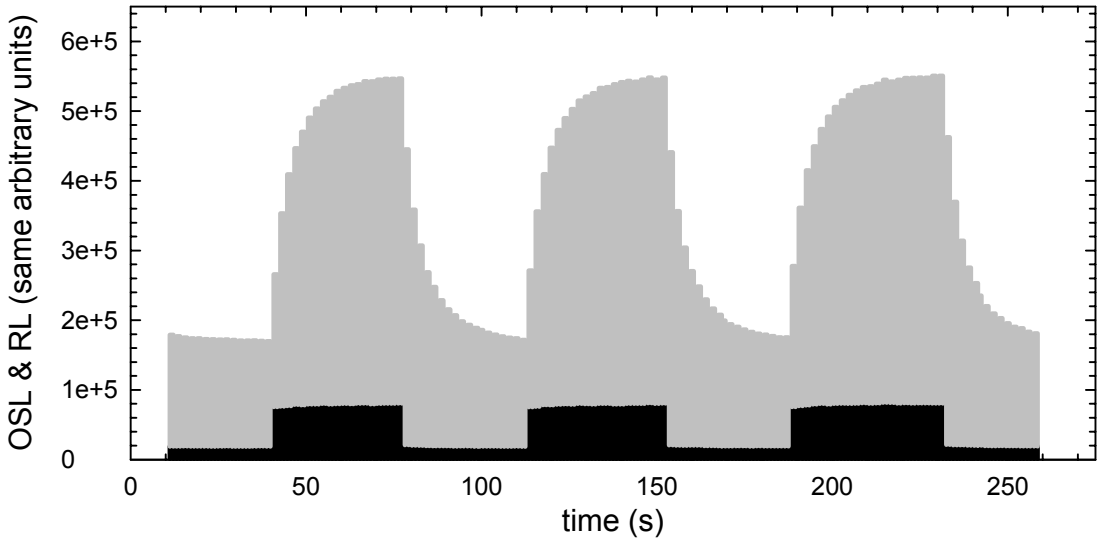

Fig. 4.25: Raw luminescence data obtained in an RT-OSL experiment on F52-1

The experiment pictured in fig. 4.24 was performed by irradiating F52-1, connected to a 1.5*m* long FT-600-UMT optical fiber, in a 250*mCi* ^{90}Sr β source. The dose rate was abruptly switched between the values of 55.4 and 177*mGy*/*s*. In spite of the long times needed by the RT-OSL to reach the equilibrium value corresponding to the new dose rate, the transitions in the calculated dose rate are sharp, as indicated by the bottom graph. The complete luminescence data, containing both the RL and the OSL components, are plotted in figure 4.25.

The precision in estimating the integral dose delivered during each of the 7 irradiations at

constant dose rate is best suggested by the standard deviation of the mean dose rate calculated from the 7 sets of data points. The values lie between 1.06-1.72% at a dose rate of 55.4*mGy*/*s* and 0.254-0.473% at 177*mGy*/*s*.

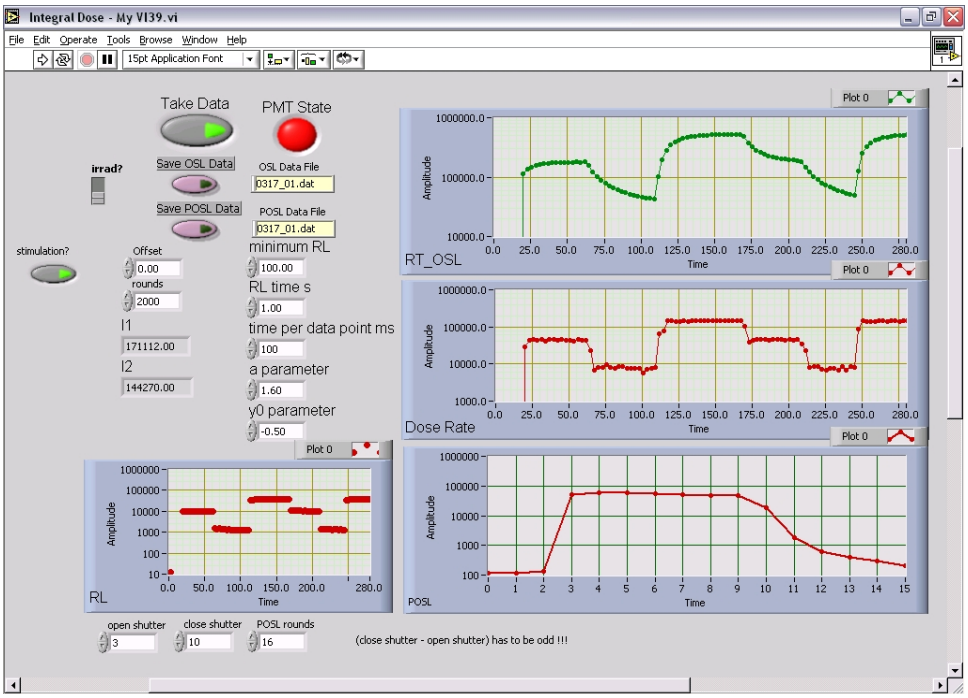

Fig. 4.26: Front panel of the 'variable shape coefficient' VI, alternate version

Later versions of the software are able to measure more than two data points during each stimulation interval. As shown in fig. 4.26, the VI was set to perform seven 100*ms*-long measurements during the stimulation interval. The surrogate shape coefficient K_S' is calculated as the ratio of the last three measurements to the previous three measurements. Due to uncertainties related to the long rise-time of the OSL signal from Al_2O_3:C, the first 100*ms*-long measurement is not used in the shape determinations.

By visualizing the shape of OSL during every stimulation interval, it can be assured that

the DOSL signal decays to an acceptable level before the next laser stimulation of the sample occurs.

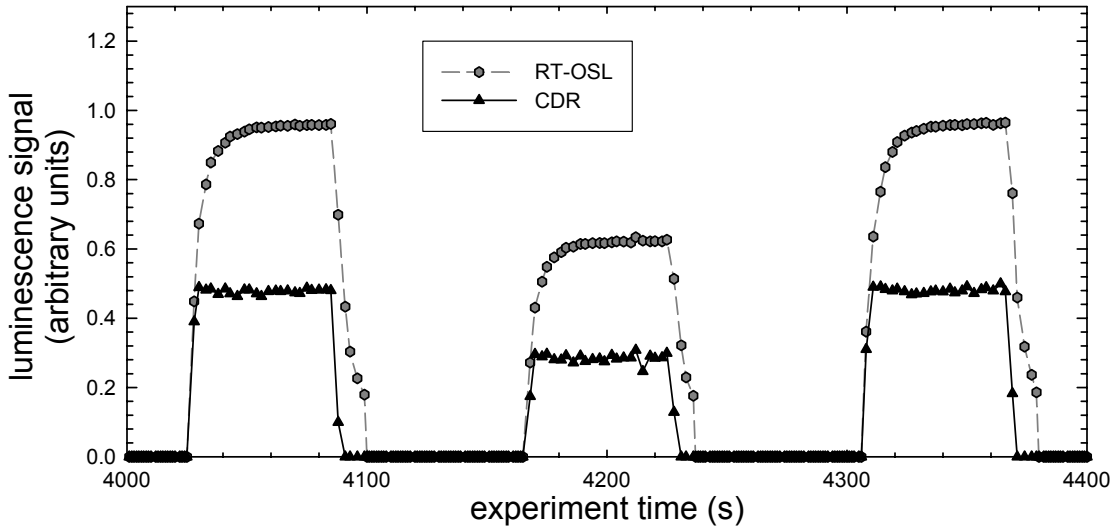

Fig. 4.27: RT-OSL and CDR signals from X-ray irradiation of F52-1

In order to evaluate the performance of the algorithm, an experiment was performed with 50*kV* X-ray irradiation. At constant voltage applied to the X-ray tube, the dose rate delivered to a fixed sample is proportional to the tube current. Sample F52-1, attached to a 1.5*m* FG-550-LER fiber, was irradiated multiple times for a duration of 1 minute. The tube current was held constant during each irradiation, at a value of 0.2, 0.4, 0.6, 0.8 or 1*mA*. The currents were randomly alternated from irradiation to irradiation. The dose rate was estimated from the intensity of the RL signal to have an order of magnitude of tens to hundreds of *mGy*/*s*, but was not calibrated exactly. The quantity of interest in the measurements was the integral dose absorbed during each 1-minute irradiation, obtained as the sum of the individual calculated dose rates (CDR) obtained from the 'variable

shape coefficient' algorithm. A fragment of the data obtained during the experiment is shown in figure 4.27. Both the RT-OSL signal and the calculated dose rate (CDR) are pictured (normalized).

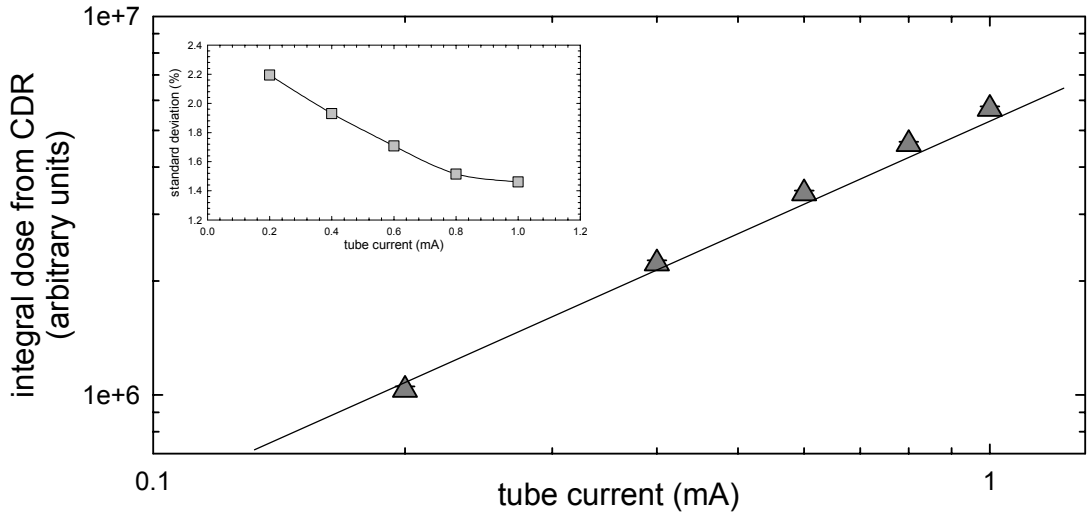

Fig. 4.28: Dose rate response of F52-1 when used with the 'variable shape coefficient' algorithm

Since all the irradiations were performed for a time of 1 minute, the data can be represented as a function of tube current to obtain the dose rate response of F52-1. As shown in figure 4.28, the supralinearity of the traditional OSL dose response of F52-1 is maintained by the variable shape coefficient algorithm. We attribute this effect to the fact that, even if the dose delivered between stimulations is small, and corresponds to the linear part of the dose response, the average trap filling level in the sample during operation at a large dose rate is high, corresponding to the supralinear region of the dose response. Therefore, a small additionally absorbed dose would cause a supralinear

response in the OSL signal.

The percent standard deviation of the integral doses measured at the same tube current (minimum 8 irradiations / tube current) are shown in the inset of fig. 4.28, and vary between approximately 1.4% and 2.2%.

While the RT-OSL shows a 'lag' in following the changes in the dose rate as indicated by the RL signal, the dose rate calculated from the algorithm promptly follows the increase and decrease of RL.

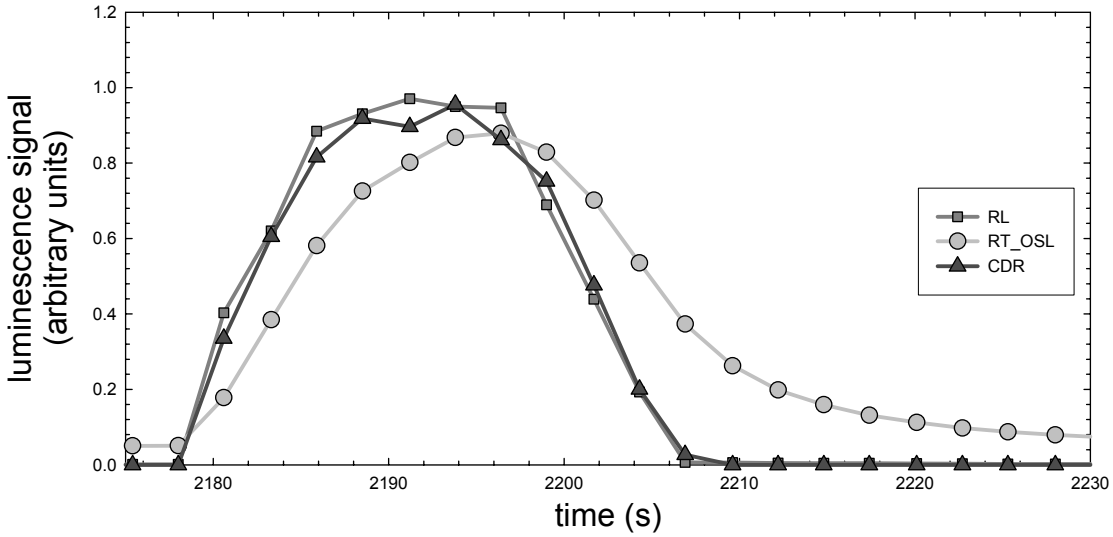

Fig. 4.29: Results from the variable K_S algorithm during an irradiation at variable dose rate

4.4. Conclusions related to the real-time OSL of Al_2O_3:C

i. Several algorithms for the acquisition and processing of the OSL signal measured while irradiating the dosimeter have been developed and integrated with the portable reader.

ii. Individual dose fractions can be acquired in time intervals as short as 2-3 seconds.

iii. The acquisition speed is limited by material properties. Among these, delayed OSL (DOSL) sets a minimal delay time required between successive stimulations. Also, the relatively long rise-time of the OSL (35*ms*) induces errors in measuring the shape of the RT-OSL if the luminescence is integrated over periods of time shorter than a few hundreds of milliseconds. Also, deviations from linearity in the traditional OSL dose response map into non-linear dose responses of the processed signals.

iv. Due to the stimulation light being in spectral proximity to the luminescence, heavy filtration is required to separate the latter, inducing important losses in the signal of interest.

CHAPTER FIVE

REAL-TIME OSL OF KBr:Eu

5.1. Background information on the dosimetric use of KBr:Eu.

Alkali halides are some of the most commonly used materials for thermoluminescence (TL) dosimetry [32]. Both KCl:Eu^{2+} and KBr:Eu^{2+}, as well as mixtures of the form KCl_xBr_{1-x}:Eu^{2+} have been investigated as dosimetry materials for UV, X-ray and β-radiation. The emission spectra have been studied for radioluminescence (RL) under X-ray irradiation [33], thermoluminescence (TL) after UV and β irradiation [34, 35] and optically stimulated luminescence (OSL) after UV-irradiation [36]. In all cases, the luminescence peaks at a wavelength around 420*nm*, and is attributed to the $4f^6 5d - 4f^7$ transition in Eu^{2+}.

The OSL stimulation spectra are reported [37] to peak at wavelengths around 560*nm* for KCl:Eu and around 620*nm* for KBr:Eu.

The TL dose response of KCl:Eu^{2+} (0.015 *mol%* Eu) at UV irradiation is found [34] to be linear over 4 orders of magnitude. A higher concentration of europium (0.049 *mol%*) induces strong supralinear behavior in KCl:Eu^{2+} for β doses on the order of 4*mGy* [35]. At the same doses, KBr:Eu^{2+} (0.078 *mol%*) is reported to have a sublinear dose response.

Buenfil et al [38] find the TL dose response of KBr:Eu (0.1*%*) irradiated with β- and γ-rays to be linear between $3*10^{-4}$ and 10^{-1}*Gy* after a thermal treatment consisting out of repeated annealing at 450˚C followed by rapid cooling to room temperature (RT).

While some authors [37] report excellent fading characteristics for the OSL signal obtained from samples of KBr:Eu (0.01 *mol%* Eu^{2+}), others [35] describe a very fast fading TL signal during the first 10-20*s* after irradiation for KCl_xBr_{1-x}:Eu^{2+}, for all the investigated

samples having composition coefficients x ranging from 0 to 1 (concentrations ranging between 0.049*mol%* and 0.078*mol%* Eu). The fading of TL from KBr:Eu (0.1*%*) has been confirmed by other investigators [38] – 2 orders of magnitude over 10,000 minutes. The lifetime of the 420*nm* OSL luminescence center is given [36] as $1.6\mu s$.

5.2. Initial experiments with Eu-doped alkali halides

OSL experiments were performed on different Europium-doped alkali halide crystals grown in the Crystal Growth Lab of the Physics Department at OSU between 1975 and 1987 by Dr. J.J. Martin et al.: NaCl:Eu, KCl:Eu and KBr:Eu. The concentration of Eu in the starting mix from which the crystals were grown is given in table 5.1.

Material	Date grown	Eu concentration (*mol%*)
KBr	01/05/1987	0.0183
KCl	03/17/1975	0.00317
NaCl	06/30/1975 or 07/09/4975	0.00123 or 0.00770

Table 5.1: Concentration of the Europium dopant in the starting mix from which the studied crystals were grown

It is estimated that the concentration of Eu in the growth product is about one order of magnitude lower than in the starting material [39] and shows a gradient along the growth axis of the crystal.

The OSL fiber samples have been prepared by cleaving the supplied crystals into rectangular prisms, having lengths (heights) of about 4*mm*, and square transversal areas of about $300\mu m \times 300\mu m$. The resulting dosimeters have been attached to the fiber

guides with plastic tubing, according to the same method used for the Al_2O_3:C fiber-shaped crystals.

The spectral distribution of the luminescence light from the samples was obtained by investigating the RL from the dosimeters during β irradiation at a dose rate of 177*mGy/s*. The spectrum was measured with an Ocean Optics S2000 fiber spectrometer, and is reproduced in figure 5.1.

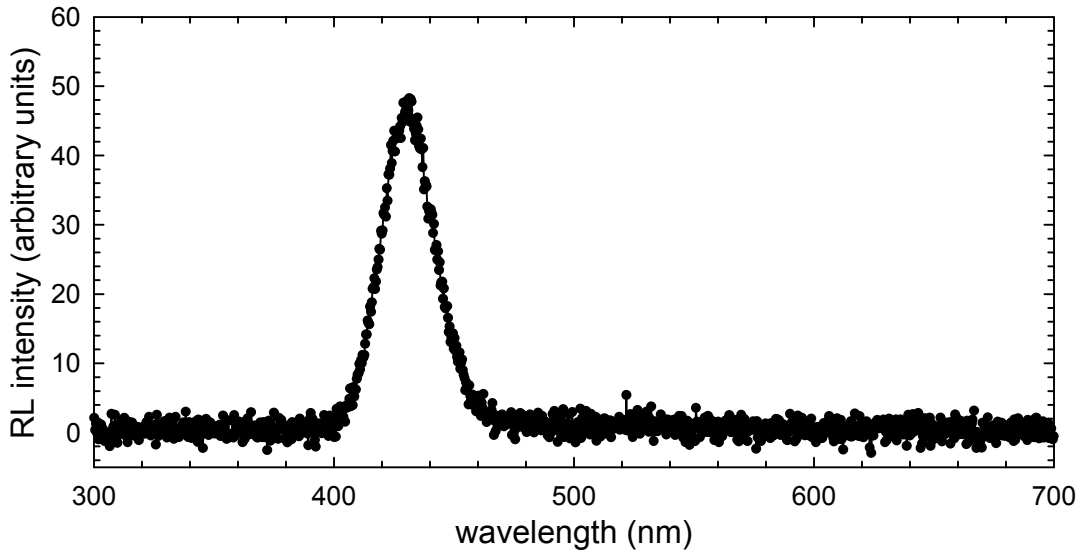

Fig. 5.1: RL emission spectrum of a KBr:Eu sample, irradiated at 177*mGy/s*

The calibration coefficients of the spectrometer were factory-specified; however, since no additional calibration has been performed by using a reference light source, the data presented in fig 5.1 should not be regarded as being extremely precise; still, the spectrum confirms the location of the luminescence peak from KBr:Eu in the blue region of the spectrum, around 430*nm*, in the same spectral region as the *F* center emission in Al_2O_3:C. Therefore, the filter pack used to discriminate the luminescence signal from the

stimulation background in the Al_2O_3:C portable reader is fully compatible with the new material, and comparative measurements using green Nd:YAG stimulation can be performed without any modifications to the portable system.

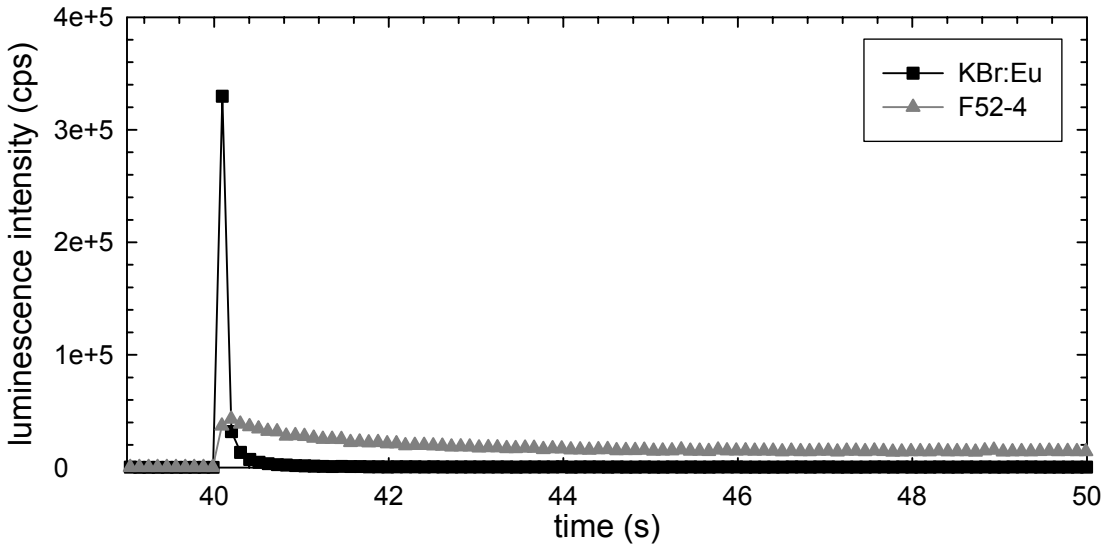

Fig. 5.2: Comparison of the OSL decay of F52-1 and KBr:Eu-1 samples under green laser stimulation (100*mW*)

A comparison of the traditional OSL decays of the F52-1 (Al_2O_3:C) sample and of a KBr:Eu sample denoted as KBr:Eu-2 is shown in figure 5.2. The two samples, having comparable sizes, were successively attached to a 5*m*-long, 0.5*mm* diameter Mitsubishi ESKA plastic optical fiber, and irradiated with 23.9 *mGy* of β radiation. The stimulation light was applied in both cases approximately 30*s* after the end of irradiation.

The maximum OSL intensity measured from the KBr:Eu sample is one order of magnitude larger than the OSL maximum from F52-1. The OSL bleaches much faster (decay time less than 50*ms* under the described conditions), to a lower background.

In order to take advantage of the OSL characteristics of the new material, a dedicated reader was built specifically for KBr:Eu. The stimulation wavelength was chosen to be in the red region of the spectrum, in order to maximize the bleaching efficiency. Since the stimulation light was applied in a spectral region situated further away from the luminescence signal than in the case of Al_2O_3:C, it was possible to use less demanding filtration to separate the latter from the former. Besides eliminating the costs associated with expensive dichroic filters, the new spectral distribution of the stimulation light insures a minimal leakage into the photomultiplier tube used for measuring the luminescence signal, thus decreasing the OSL background and increasing the signal-to-noise ratio of the measurement.

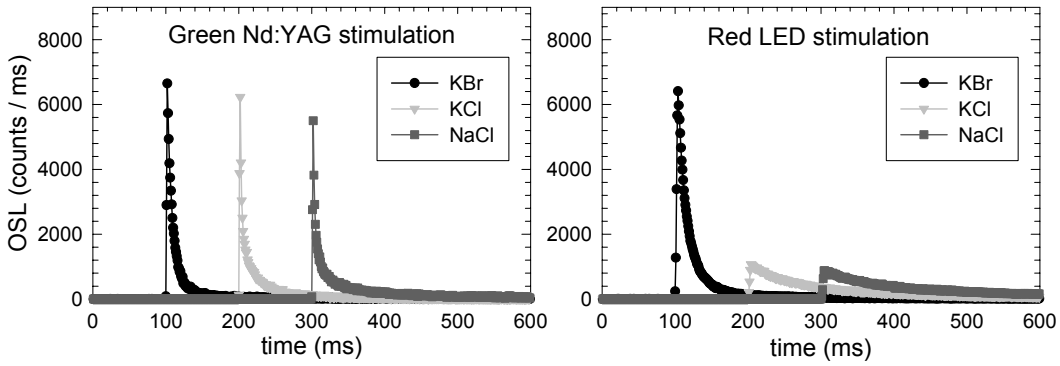

Fig. 5.3: Traditional OSL from different alkali halides under different colors (green and red) of laser stimulation

Switching to red stimulation consecrated KBr:Eu as the material of choice. Even though all the investigated alkali halides reacted similarly under green stimulation, KBr:Eu was the only material to respond favorably to red light. A comparison of the OSL from different materials, under both green and red stimulation, is shown in figure 5.3.

5.3. Architecture of the OSL fiber reader used with KBr:Eu

The schematic diagram of the reader is given in figure 5.4.

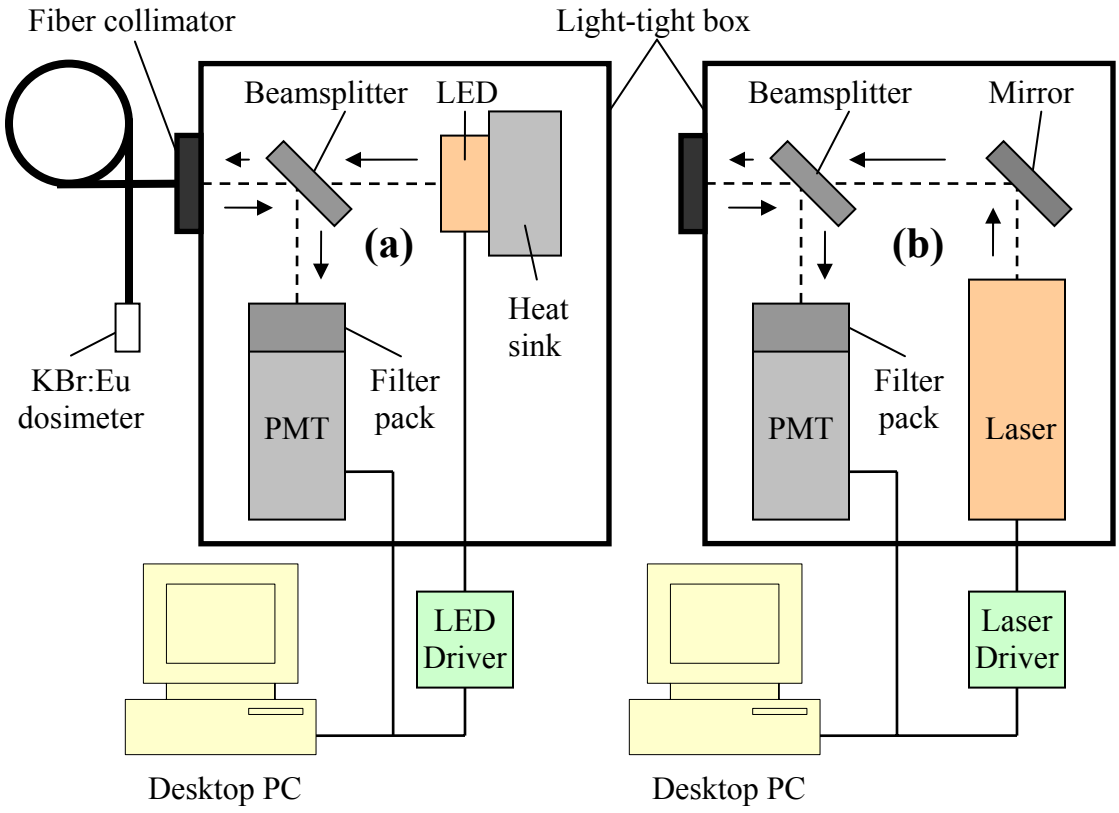

Fig. 5.4: Schematic diagram of the KBr:Eu fiber OSL reader: (a) with red LED stimulation; (b) with red diode laser stimulation

In an early stage of the project, the stimulation light was provided by a 44 lumen red light emitting diode (LED) manufactured by LUXEON (type LXHL-ND98, $\lambda max = 625nm$). The LED was supplied by the manufacturer with integrated optics for collimation of the output beam. The optical power of the stimulation light, coupled into a $15m$ long FT-600-EMT Thorlabs optical fiber, was measured at the sample as approximately $1.2mW$. The

modulation of the red light was achieved by using an electronic driver, controlled by TTL pulses generated by the DAQ card. The rise time of the LED output was measured at approximately $3\mu s$ with a Thorlabs DET 210 photodiode detector and a LeCroy 9400A oscilloscope.

Later, the red LED was substituted by a semiconductor laser of the type PPMT-LD1360, manufactured by Power Technology Inc. The emission wavelength is specified as $\lambda = 658nm$ and the maximum optical power as $p = 50mW$. To insure an extended lifetime of the laser diode, the power was set (by the manufacturer) at approximately $35mW$, and consequently the power at the sample was measured to be approximately $20mW$. For stability of the optical power output, a Peltier thermo-electrical cooling system maintains the diode temperature at a constant value. The laser can be TTL modulated by an external signal with a frequency up to $20MHz$ via the supplied driver. The rise-time of the laser output (zero to full power) was measured as $50ns$.

Stimulation light from either of the two possible light sources is coupled into the optical fiber by a Thorlabs collimator similar to the one used for the Al_2O_3:C system, and is conducted to the KBr:Eu dosimeter.

The OSL from the sample is collected through that same optical fiber and reflected by a beamsplitter (Edmund Industrial Optics, NT52-543 yellow subtractive) toward a PMT (Electron Tubes, Inc., P10PC). The filter pack in front of the PMT consists out of a set of 5-58 filters ($410nm$ maximum transmission, $60nm$ width) of a total thickness of $13mm$. The amount of filtration is actually limited by the brightness of the sample, rather than by the large background level. Measurement of larger dose rates requires additional filters in front of the light detector in order to avoid reaching the nonlinear region of the PMT.

A picture of the KBr:Eu reader is reproduced in figure 5.5.

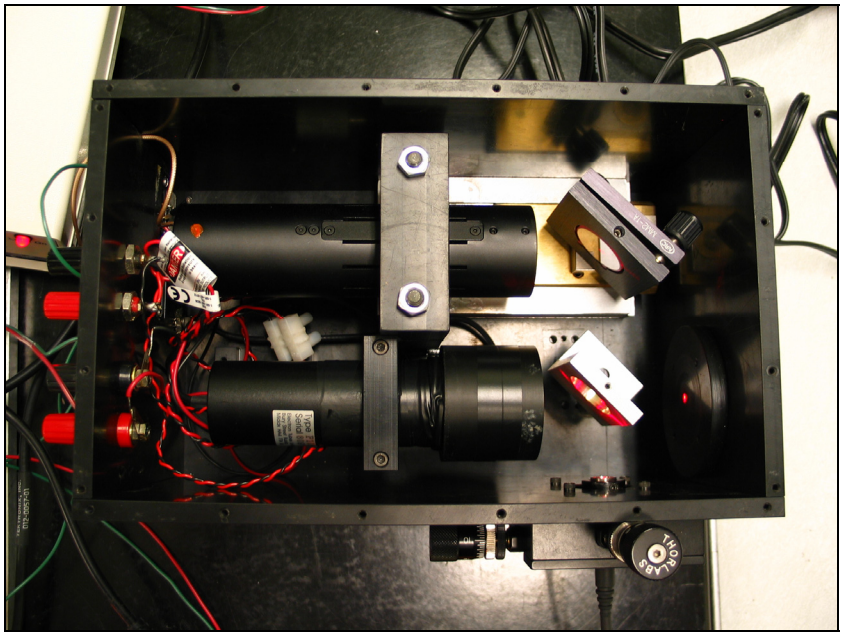

Fig. 5.5: Picture of the KBr:Eu fiber reader

The portability of the system was traded off for higher computation power required to take advantage of the faster material. Data acquisition and control is achieved by a National Instruments 6602 PCI Counter Card, which contains 8 counters that can be hardware-triggered. Thus, the measurement of the OSL signal can be synchronized with intervals of laser stimulation applied for periods on the order of tens of milliseconds. With the counter card installed on a dual-processor $1GHz$ desktop PC, it is possible to measure the luminescence signal with resolutions as high as $10\mu s/d.p.$ Under normal operation conditions, the OSL is measured at lower resolutions on the order of hundreds of $\mu s/d.p.$ For small doses, stimulation intervals of $20ms$ suffice to bleach the OSL to the background level.

The synchronization of the data acquisition sequence is achieved by inter-correlating the counters of the DAQ (counter) card, as described by the diagram in figure 5.6

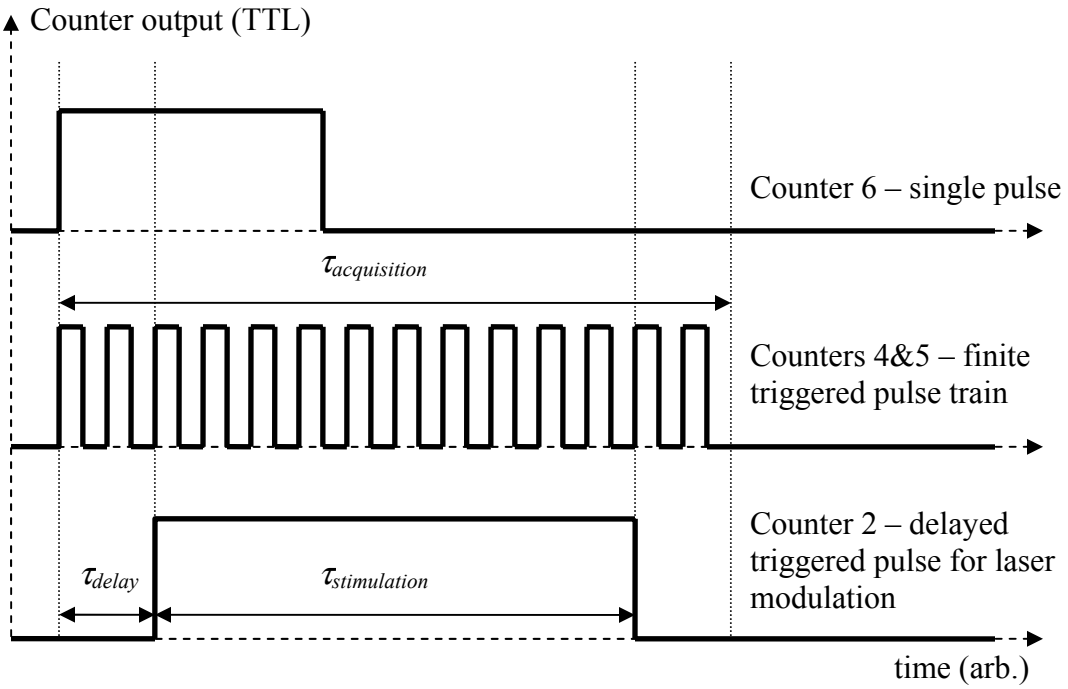

Fig. 5.6: Data acquisition sequence for the Counter Card 6602

At the beginning of each data acquisition sequence, a TTL pulse output by counter 6 simultaneously triggers a finite train of pulses on the counter 5, and a delayed pulse on counter 2. The PMT output is connected to the counter 1, which continuously increments its value with each photon detected by the PMT. At each low-to-high transition in the pulse train generated by counter 5, the instantaneous value at counter 1 – equal to the total number of photons detected by the PMT in the current acquisition sequence - is dumped into a memory buffer. After the number of measurements specified by the length of the pulse train has been performed, the buffer is written into an array containing the

incremental number of counts. By taking the difference between pairs of successive readings in the array, the OSL measured between every two successive pulses in the finite train can be determined. The total time of the signal acquisition $\tau_{acquisition}$ is given by the number of pulses and the frequency of the pulse train.

At a predetermined time τ_{delay} after the acquisition is initiated, the delayed pulse from counter 2 turns on of the stimulation light for an amount of time $\tau_{stimulation}$.

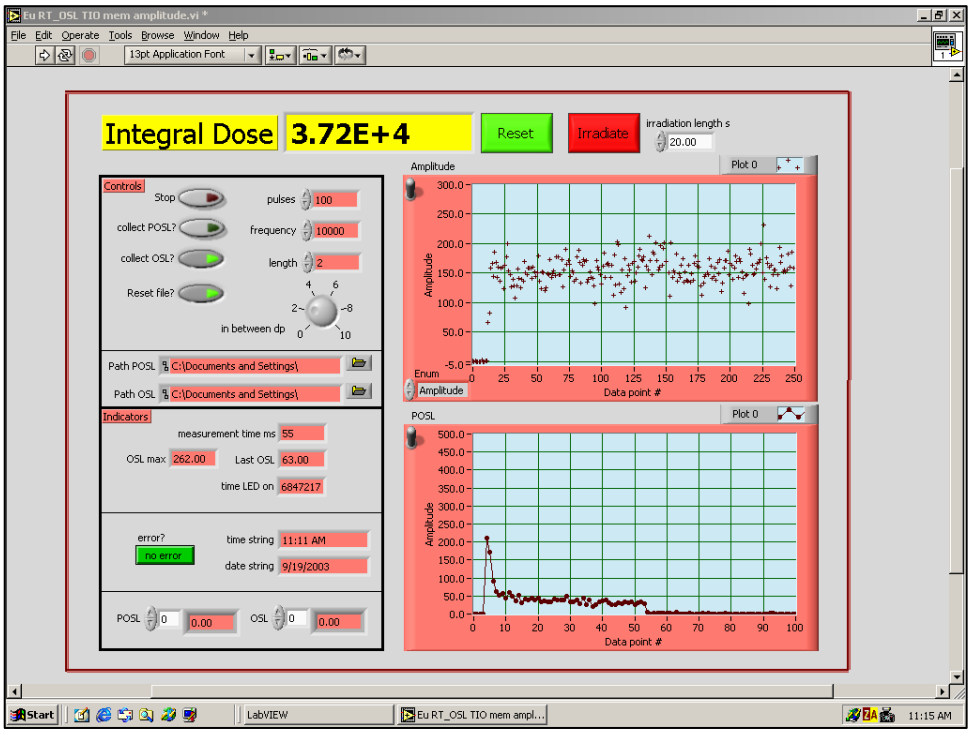

Fig. 5.7: Front panel of the VI used for RT-OSL measurements with KBr:Eu

All the timing variables can be set by the user in the front panel of the VI controlling the data acquisition and the subsequent processing of the OSL data. The parameters used in the measurement described in figure 5.7 are:

- OSL integration time: $100\mu s$ (10,000 *Hz* data acquisition frequency);
- Number of data points / decay: 100;
- $\tau_{delay} = 500\mu s$ (5 data points)
- $\tau_{stimulation} = 5ms$ (50 data points)
- $\tau_{acquisition} = 10ms$ (100 data points)

Due to the heavy amount of data processing, the time required by the computer to analyze an OSL decay and to perform the associated graphical computations is 55*ms*. Thus, the dose absorbed during an irradiation can be updated at a frequency of about 18*Hz*.

The data acquisition procedure works equally well with LED and laser stimulation. The TTL output of counter 2 can be used for modulating either the laser or LED driver. Experiments performed with both LED and laser stimulation will be presented in the next sections, and the type of stimulation and timing parameters will be specified each time.

5.4. Basic OSL properties of KBr:Eu

5.4.1. Traditional OSL

A typical 'traditional OSL' decay of KBr:Eu under red laser stimulation is shown in figure 5.8. The KBr:Eu-2 sample was irradiated for 3*s* at a dose rate of 7.97*mGy/s* of β radiation from a ^{90}Sr source, resulting in a total absorbed dose of 23.9*mGy*. The stimulation light was applied at 1*s* after the end of irradiation. Each data point represents the OSL integrated over $100\mu s$.

The OSL decay time can be estimated from the graph at about $500\mu s$. However, the same OSL data represented in log scale indicate a decreasing trend due to a slow

component, still present in the decay after 90*ms* of stimulation.

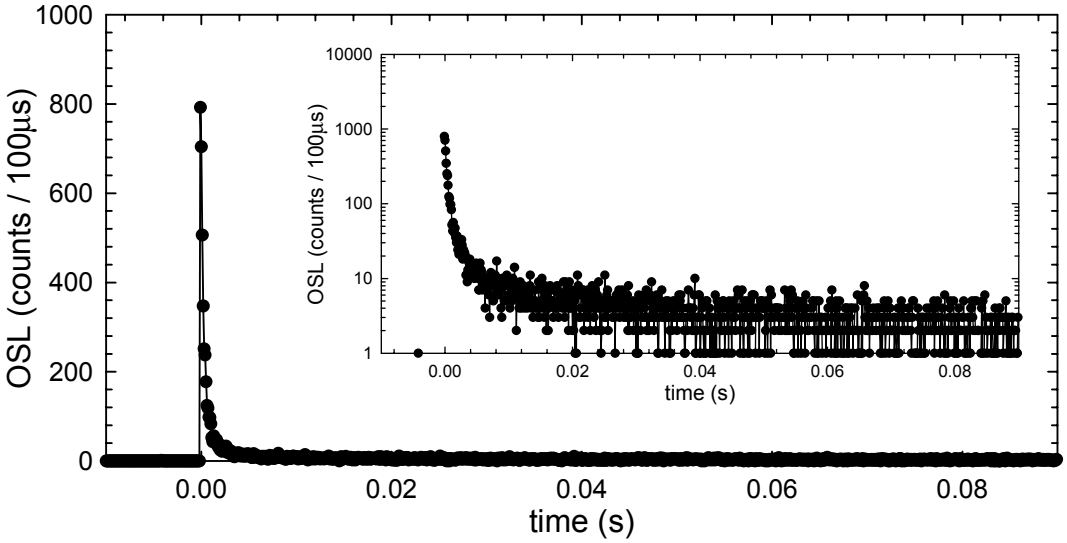

Fig. 5.8: Traditional OSL of KBr:Eu-2 after 23.9*mGy* of β radiation, represented on both a linear and on a logarithmic (inset) scale

5.4.2. Fading properties

The fading of the OSL signal is presented in figure 5.9. After being irradiated for 3 seconds at a dose rate of 0.344*mGy/s*, the KBr:Eu-2 sample was stored in the dark for increasing periods of time before red laser stimulation was applied. The OSL was integrated over 2*ms* (by summing the first 20 data points after stimulation was applied) and represented as a function of the storage time. The experiment was repeated afterwards at a different dose rate (7.97*mGy/s*), and the results indicated essentially the same behavior.

The experimental data in fig. 5.9 indicates negligible fading over time intervals on the order of 10 seconds. The signal fades to 50% of the initial value over periods of time on the order of 15 minutes.

It was noticed that subjecting the sample to thermal treatments (the initial annealing procedure) has significant, long-term consequences on the fading behavior of the OSL. Even though during the normal operation of the dosimeter it is not necessary to thermally anneal the KBr:Eu dosimeters, concerns related to the changes occurred in the crystalline structure of the investigated dosimeters in the last ~20 years since they were grown determined us to test the effects of some annealing procedures.

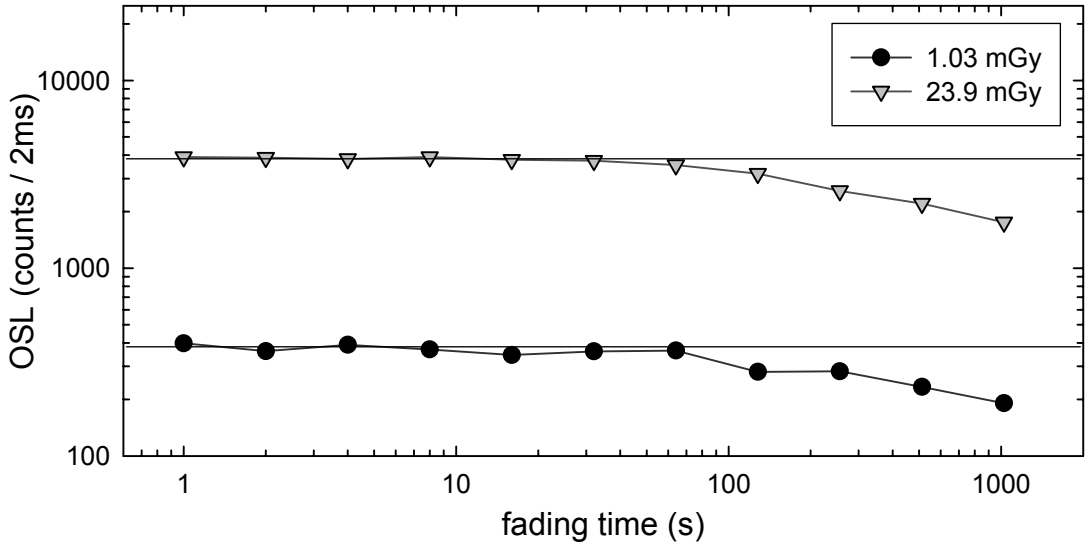

Fig. 5.9: Fading of OSL from sample KBr:Eu-2 after the absorption of 1.03*mGy* and 23.9*mGy*, respectively

The data in fig. 5.9 were obtained after heating up the sample KBr:Eu-2 for 1*hr* at 600℃, followed by slow cooling to 100℃ (1℃/s), and by subsequently keeping the sample for an additional 10*hrs* at 100℃. Besides this annealing procedure, referred to as 'slow cooling', another treatment involving 1*hr* baking at 600℃ followed by rapid cooling to RT lead to worse fading properties.

It has been long known that high temperature annealing can lead to sensitivity changes in traditional TL materials such as LiF:Mg, Ti. The effect has been attributed [31] to the dissociation of the trimer defect clusters responsible for charge trapping in the respective materials. The equilibrium state is only reached at a long storing time following such high-temperature annealing. Long annealing at lower temperatures (24*hrs* at 80*°C* in the case of LiF:Mg, Ti) favor the cluster formation process, and the restoration of the TL sensitivity of the dosimeters.

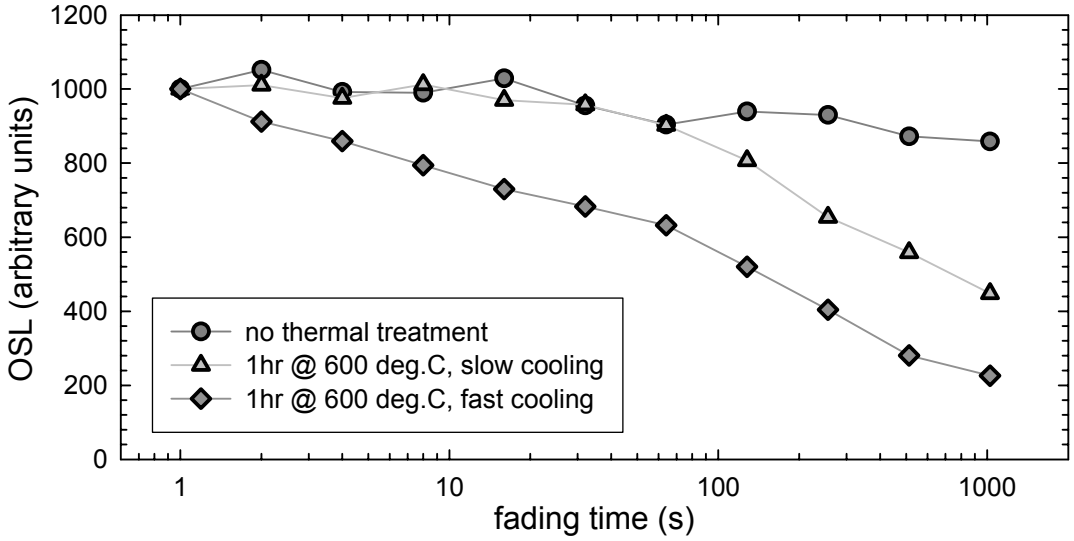

Fig. 5.10: KBr:Eu OSL fading after different thermal treatments

The same conclusion can be drawn from the data in figure 5.10, which presents a comparison in the fading properties of three samples subjected to either 'slow cooling' or 'fast cooling' following the 600*°C* annealing, or no thermal treatment at all. Previously to being used in this experiment, the samples were stored away for a time interval on the order of 10 years. The lowest fading (<20% over 15*min*) occurs for the untreated sample,

and the highest for the sample rapidly cooled to room temperature after annealing.

5.4.3. Traditional OSL dose response

Most usually, the dose response of a luminescence dosimeter is obtained by irradiating the sample for variable amounts of time, using a source of ionizing radiation that delivers a fixed, and previously calibrated, dose rate. Then the dose absorbed in the sample during each irradiation is calculated by multiplying the dose rate with the exposure time.

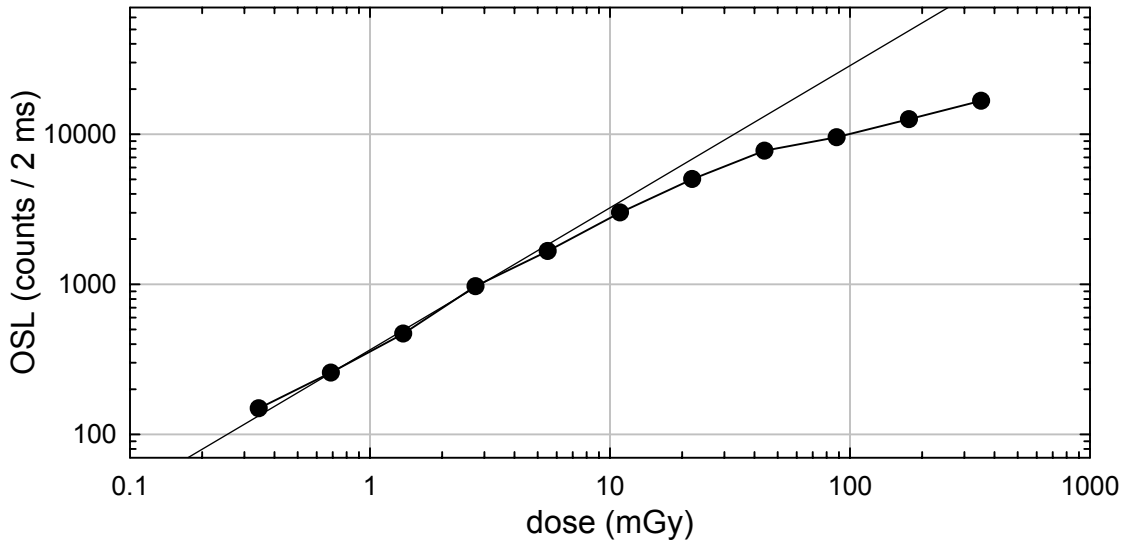

Fig. 5.11: OSL dose response of KBr:Eu-2, at a dose rate of 0.344*mGy/s*

The above approach was used for the determination of the dose response from a KBr:Eu dosimeter (sample KBr:Eu-2). The sample was connected to a 15*m*-long FT-600-EMT optical fiber from Thorlabs, and irradiated in a ^{90}Sr source, at a β dose rate of 0.344*mGy/s*. To stimulate the OSL, red laser light was applied to the sample starting 1*s* after the end of irradiation, and for a time period of 5*s*, sufficient for the total bleaching

of the OSL signal. The signal of interest, OSL integrated over 2*ms*, is represented as a function of the absorbed dose in figure 5.11.

The OSL dose response is linear for doses up to approximately 5*mGy*, corresponding to an irradiation time of 15*s*, and afterwards becomes sublinear.

At this point, it is important to point out that the dose response obtained by the method above actually represents the convolution of the dose response with the fading properties of the sample.

In order to obtain a dose response completely independent of fading, it would be necessary to irradiate the samples for the same time intervals, at different dose rates, and to stimulate the OSL at the same time interval after the irradiation ceases. For instance, this procedure could be achieved by irradiating the samples with X-rays, and then studying the OSL response as a function of tube current.

Since fading alone induces an additional degree of sublinearity in the dose response obtained at a fixed irradiation dose rate, it can be stated that the OSL from the sample is in fact linear with dose over a larger range than indicated in fig. 5.11.

5.5. Real-time OSL of KBr:Eu

As shown in figure 5.8, the OSL signal induced by 23.9*mGy* of absorbed radiation appears to be efficiently bleached within time intervals on the order of 10*ms*. Therefore, this material should be suitable for real-time measurements according to the original approach suggested by Creager (see figure 3.3). Still, as will be seen in the next sections, supplemental procedures will be needed to correct the sensitivity variations that occur in the course of irradiation procedure.

The experiment was performed by irradiating an initially bleached sample (KBr:Eu-1, attached to a 1.5*m*-long FT-600-UMT optical fiber) with β radiation at a dose rate of 177*mGy/s*, for a period of time on the order of 1 minute. During irradiation, the sample was periodically stimulated with red laser light for intervals of 18*ms*, repeated at approximately 65*ms*. The OSL from the sample was measured at a frequency of 5*kHz* ($200\mu s/d.p.$), starting 1*ms* before the beginning of each laser stimulation interval, and extending up to 1*ms* after the stimulation end. Thus, 100 data points were collected during each data collection period of (1+18+1)*ms*. The typical shape of the OSL decay obtained during one stimulation interval is presented in figure 5.12.

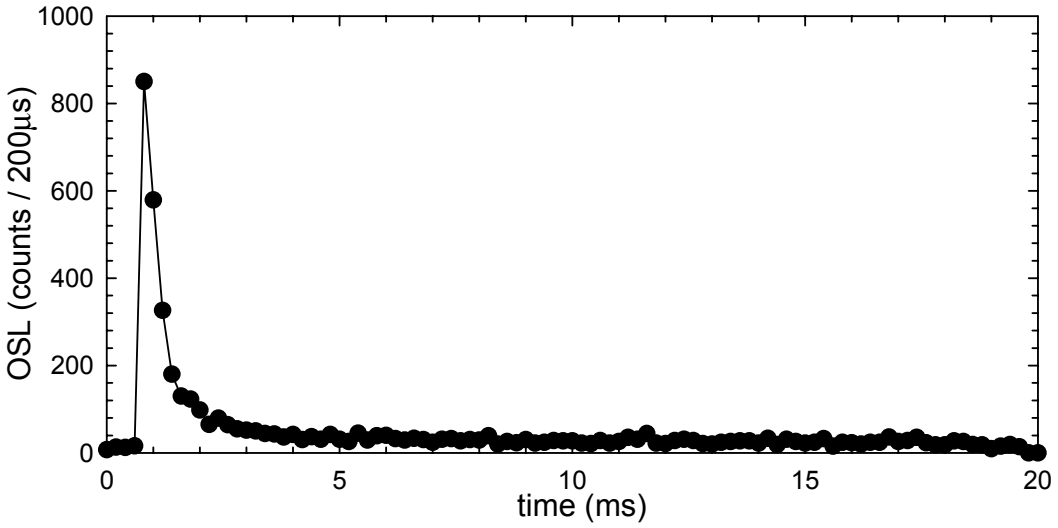

Fig. 5.12: Typical RT-OSL decay for the KBr:Eu-1 sample, under irradiation at a dose rate of 177*mGy/s*

Consider a sample being completely bleached during a given stimulation interval. The next laser-on interval should stimulate an OSL that is proportional to the dose absorbed in

the sample during the previous 45*ms* period during which laser light was not applied. Thus, for an irradiation at constant dose rate, the OSL maximum of every decay should have a constant value, proportional to the irradiation dose rate.

However, experimental data plotted in figure 5.13 indicate a trend in the time evolution of the maximum OSL intensity during the irradiation at the fixed dose rate of 177*mGy/s*, for both samples. The duration of the laser stimulation was 18*ms* for OSL data acquisition frequency of 5*kHz*, and 9*ms* for OSL data acquisition at 10*kHz*.

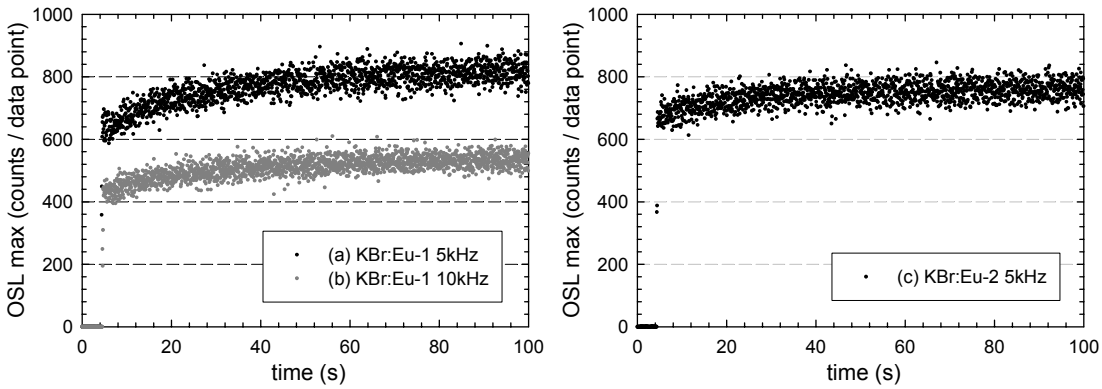

Fig. 5.13: Long-term effects in the OSL maximum from KBr:Eu during irradiation at a dose rate of177*mGy/s*

While being irradiated, the samples undergo a sensitization process, similar to the one observed in Al_2O_3:C. The smaller magnitude of the effect for sample KBr:Eu-2, as compared to sample KBr:Eu-1, is attributed to the thermal treatment sample 2 has been exposed to (1hr @ 600℃, cooling at 1℃/*s* to 100℃, 10hrs @ 100℃, then slow to RT). Also, reaching the maximum sensitivity appears to take place slower when longer intervals of laser stimulation are applied. As in the case of Al_2O_3:C, the phenomenon is

attributed to the presence of competing traps, less sensitive to photo stimulation, which give rise to a slow component in the OSL decay. An idea about the relative time constants of the two exponential-like decays can be obtained from a fit of the data in figure 5.12. The fitting function used is a double exponential of the form

$$I_{OSL} = A_1 e^{-\frac{t}{\tau_1}} + A_2 e^{-\frac{t}{\tau_2}} + y_0 \qquad (5.1)$$

and the results of the fit are represented in table 5.2.

Parameter	Value	±Error
y_0 (counts / 200μs)	22.9468	2.05043
A_1 (counts / 200μs)	43.31943	10.34662
t_1 (ms)	3.62651	1.21862
A_2 (counts / 200μs)	800.8759	13.27667
t_2 (ms)	0.37052	0.01208

Table 5.2: Parameters resulted from a double exponential fit of a RT-OSL decay measured in KBr:Eu-1 during irradiation at 177mGy/s

The fitted parameters indicate the presence of two components, the more intense component decaying approximately 10 times faster than the slow one. The long-time effects noticed in figure 5.13 are due to the incomplete bleaching of the slow component during every stimulation. It is also possible that a third, even slower component is present in the decay, but cannot be isolated from the recorded data set of a limited length. The ultraslow component is visible only in the background level of the OSL decay. A comparison of the normalized RT-OSL decays of a non-annealed (KBr:Eu-1) versus an annealed (KBr:Eu-2) sample, obtained in the same conditions as described for fig. 5.12,

is shown in figure 5.14, and reveals an increase in the relative OSL background from the annealed sample.

From the data in figures 5.10, 5.13 and 5.14, it appears obvious that the thermal treatment applied to the KBr:Eu samples can significantly affect the balance of the different types of traps. Although the thermal treatments increase the OSL background and worsen the fading properties, they also seem to improve the behavior of the samples in terms of sensitization effects under irradiation at high dose rates.

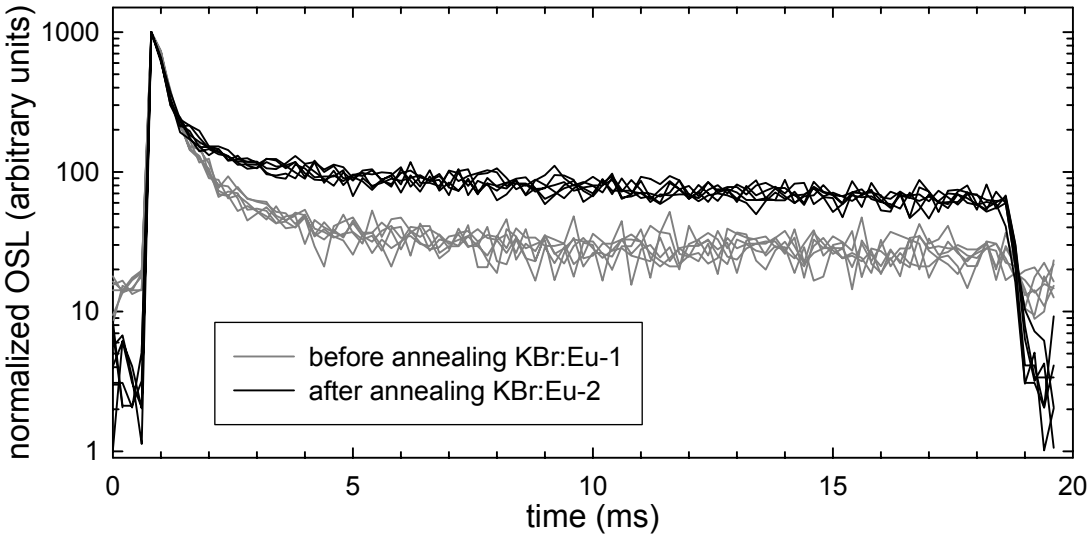

Fig. 5.14: Normalized RT-OSL decays obtained for two KBr:Eu samples before and after thermal treatment. Six typical decays are presented for each case

Aside from thermally treating the samples, the undesired changes in sensitivity can be compensated for by applying proper correction algorithms for the OSL data. Instead of considering only the OSL maximum as the signal of interest, these algorithms use information contained in different sections of the OSL decay. Figure 5.15 shows a

sequence of two OSL decays separated by a laser-off time interval 50*ms* long. Three different signals are defined for each decay, and denoted as I_0, I_1 and I_2.

The signal I_0 is the OSL maximum, integrated over a given number of data points. In the particular situation depicted in figure 5.15, I_0 is defined as the sum over the first two data points in the OSL decay ($400\mu s$ OSL). I_1 represents an OSL measured later in the decay, integrated over the same time interval as I_0. As shown in fig 5.15, I_1 is the sum of the 5th and 6th data points in the OSL decay. I_2 is the last OSL signal, measured over the specified integration time, before the laser stimulation is turned off.

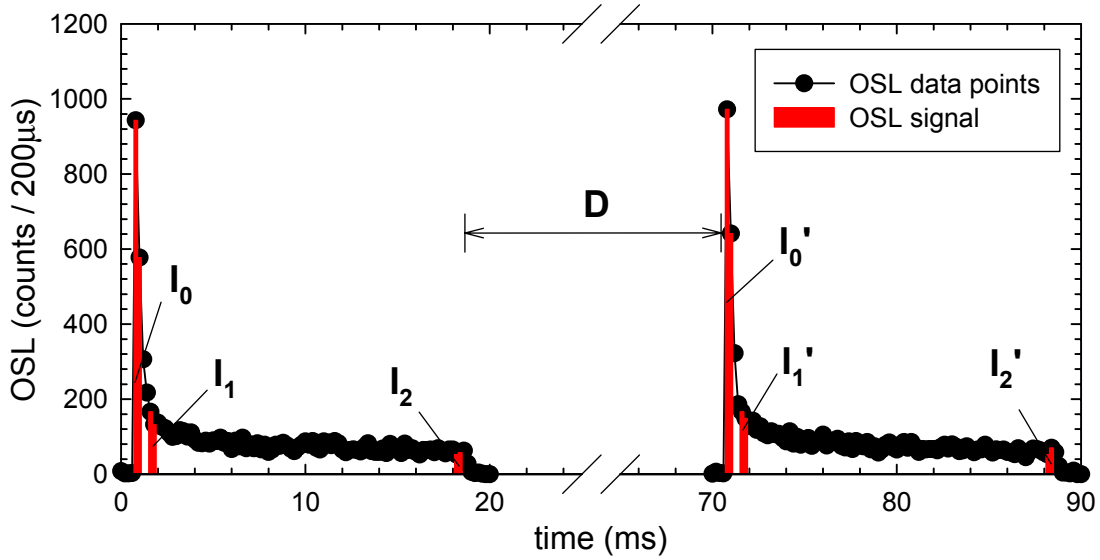

Fig. 5.15: Definition of the OSL signals of interest for the KBr:Eu data processing algorithms

With the 3 signals defined as above, the following algorithms were constructed:

A. The Δ (Delta) algorithm: The dose absorbed over the period when the laser light

is turned off should cause a proportional increase in the OSL signal. Thus, the difference between the OSL maximum of the current decay and the last OSL of the previous decay should be proportional to the dose rate:

$$\Delta_{OSL} = I_0' - I_2 = S \cdot \dot{D} \qquad (5.2)$$

where S is the sensitivity of the sample and $\dot{D}$ the irradiation dose rate.

B. The amplitude algorithm. Consider an OSL decay containing multiple components, with the fastest component having a decay time which is very short comparative to the decay times of all the other components. Then it can be considered that, during the time intervals required for the entire depletion of the fast component, the intensities of the slow components remain essentially the same. Thus, the fast component only can be isolated by taking the difference

$$A_{OSL} = I_0' - I_1' = S' \cdot \dot{D} \qquad (5.3)$$

where S' is the sensitivity of the fast component only.

In order to maximize the efficiency of the correcting algorithms, different timing parameters in the definition of the two signals can be chosen. Variables that can be freely chosen are the OSL integration time and the time delay between I_0 and I_1.

The 'Delta' algorithm applied on the data (a) in figure 5.13: 5*kHz* OSL data of sample KBr:Eu-1 irradiated at 177*mGy/s* is plotted in figure 5.16. It can be noticed that the correction has a minimal (if any) effect. The 'Delta' algorithm would be efficient in correcting the apparent sensitization of the OSL maximum due to an increase in the OSL background (or the ultraslow component). Our lack of success in applying it for the case of KBr:Eu should be indicative of the fact that the sensitivity increase appears due to changes in the balance of the fast and medium components.

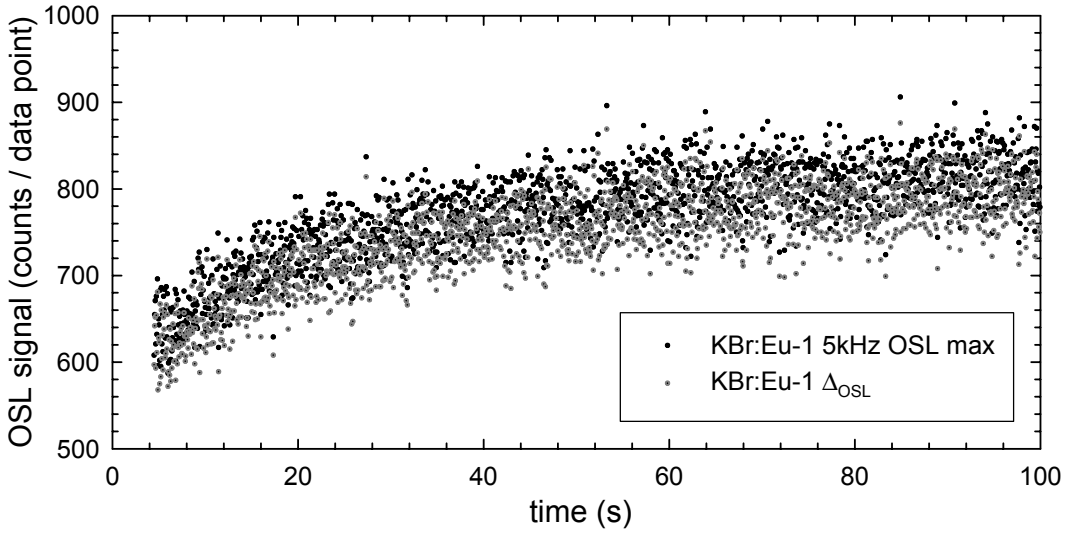

Fig. 5.16: The 'Delta' correcting algorithm applied for KBr:Eu-1 irradiated at 177*mGy/s*

The success of applying the 'Amplitude' algorithm depends upon the judicious choice of the position of the I_1 signal in the OSL decay. I_1 should be measured late enough in the decay, when the fast component will have faded away completely. Still, the time elapsed between the measurements of I_0 and I_1 should be short, so that the intensity of the medium component does not vary too much.

The data from figure 5.13 (a), corrected with the amplitude algorithm, is presented in fig. 5.17. The integration time for the OSL signals of interest was chosen to be $200\mu s$. Different delay times between the positions at which I_0 and I_1 resulted in different levels of accuracy in the signal correction. Taking the measurements I_0 and I_1 immediately after one another overcorrected for the sensitivity increase, resulting in a slightly decreasing trend for the measured dose rate (Fig. 5.17a). $400\mu s$ (2 data points) between I_0 and I_1 proved to be too long a delay time, providing an insufficient

correction, as shown by fig. 5.17c. A delay of 200μs (1 data point) returns the best results in terms of stability of the calculated dose rate, as shown in fig 5.17b.

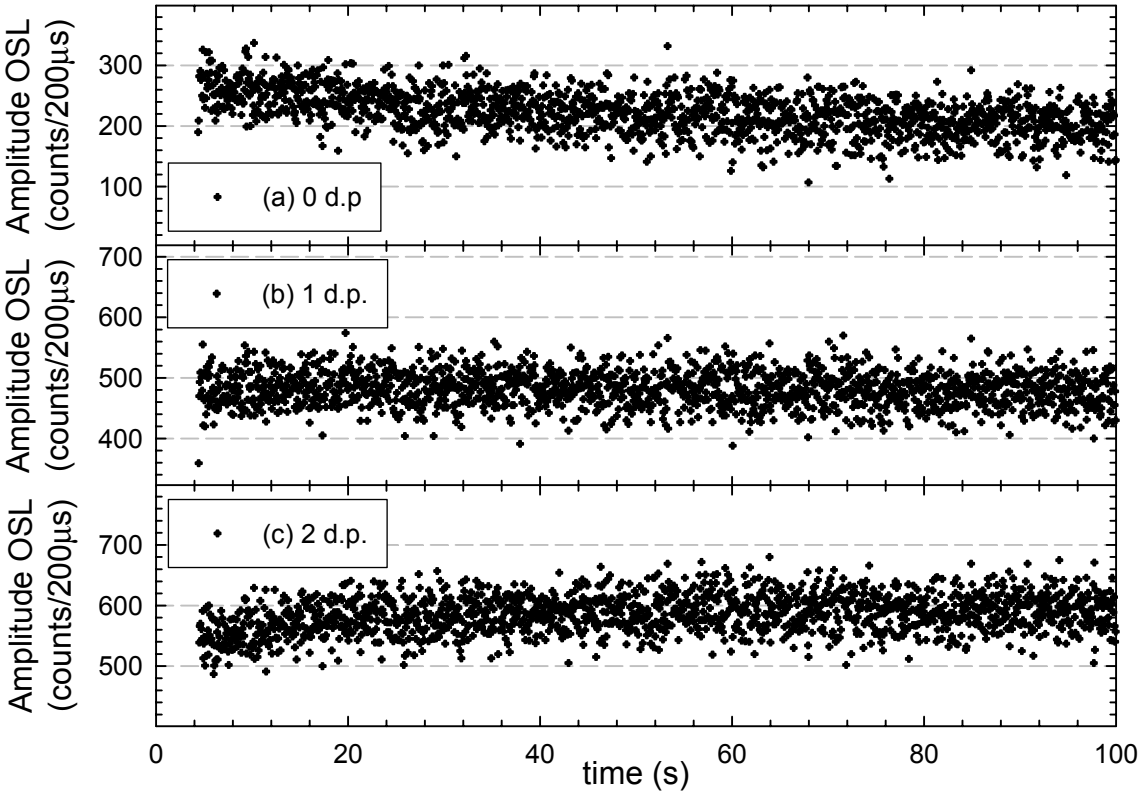

Fig. 5.17: Dose rate from the 'Amplitude' correction algorithm applied for sample KBr:Eu-1 irradiated at a dose rate of 177*mGy/s*, OSL data acquisition 5*kHz*

The algorithm can be consistently applied, with the very same timing settings, to estimate the dose rate from RT-OSL in the case of sample KBr:Eu-2, presented in figure 5.13c..

The dose rate thus obtained is represented in figure 5.18, and shows no variation during the irradiation procedure. This result suggests that the same correction parameters can be successfully used for a broader class of samples, i.e., the samples do not need to be individually calibrated in terms of the timing parameters.

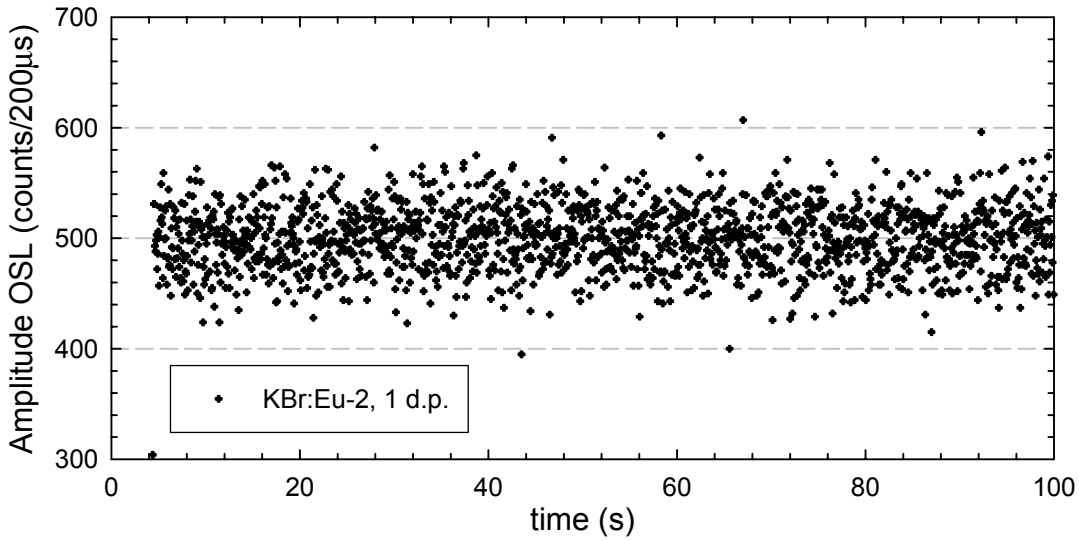

Fig. 5.18: Dose rate obtained from the 'Amplitude' algorithm during irradiation of sample KBr:Eu-2 at a constant dose rate of 177*mGy/s*, OSL data acquisition 5*kHz*

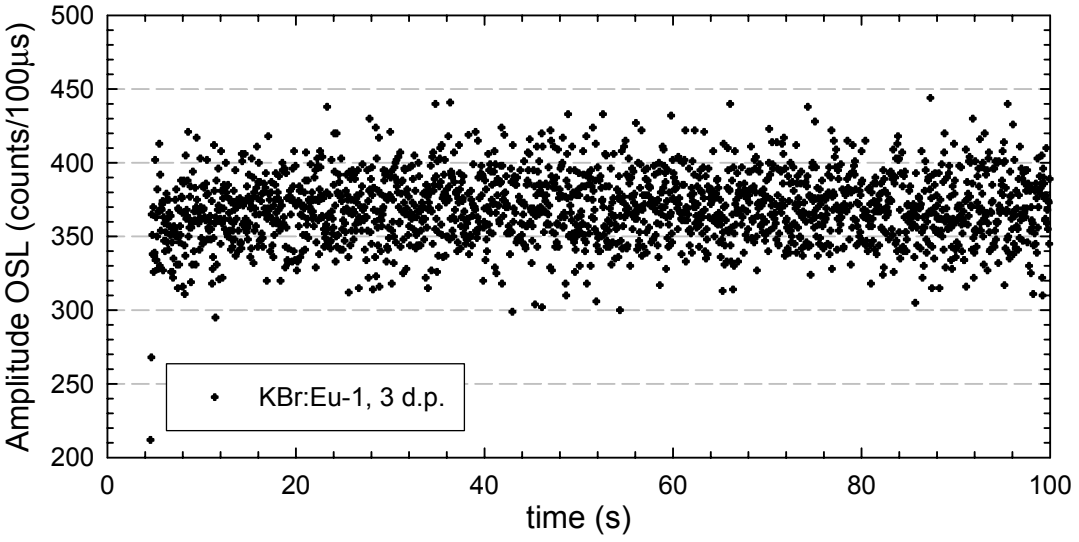

Fig. 5.19: Dose rate resulted from the 'Amplitude' correction algorithm applied for sample KBr:Eu-1 irradiated at a dose rate of 177*mGy/s*, OSL data acquisition 10*kHz*

Due to the different timing used in obtaining the data in figure 5.13b (OSL integrated

over $100\mu s$, the signals I_0 and I_1 had to be defined differently for the best possible accuracy. Namely, the delay between I_0 and I_1 (integrated over $100\mu s$ each) was taken to be 3 data points, or $300\mu s$. The result of the correction is plotted in the figure 5.19, and shows a good flatness of the corrected signal, from the very beginning of the measurement procedure.

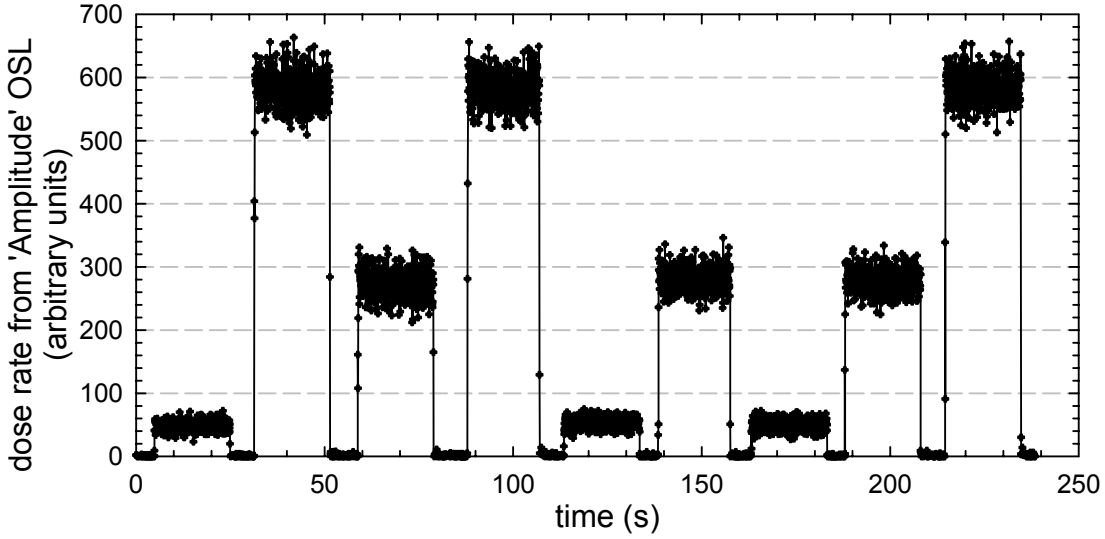

Fig. 5.20: Dose rates obtained in real-time from the 'Amplitude' algorithm applied on the OSL signal from sample KBr:Eu-2.

To evaluate the efficiency of the correction algorithm under more realistic conditions in which the dose rate varies between measurements, a series of fixed-time (20*s*) irradiations at the three dose rates of 7.97, 55.4 and 177mGy/s, alternated in random order, was performed on sample KBr:Eu-2, attached to a 1.5*m*-long FT-600-UMT optical fiber. Red laser light was used for the 18*ms*-long stimulations, and the OSL from the sample was read at a frequency of 10*kHz*. The dose rate resulted from the 'Amplitude'

algorithm is presented as a function of time in figure 5.20. Sudden application of irradiation results in quick transitions of the OSL signal, directly to the level corresponding to the particular dose rate. The efficiency of the correcting algorithm is confirmed by the absence of any trend in the OSL signal recorded at a constant dose rate.

Further processed data from these measurements are presented in figure 5.21, showing the dose rate response from the 'Amplitude' algorithm corrected OSL of the KBr:Eu-2 sample, as well as the standard deviation of the measured dose rates.

The dose rate response is linear for dose rates up to 55.4mGy/s. At this irradiation rate, and with a 'dosing' time interval of approximately 50ms, the dose absorbed between two successive OSL stimulations is on the order of 3mGy. For larger dose rates, the dosimeter response becomes sublinear. It should be noted that the sublinearity in the dose response can be compensated for by reducing the 'dosing' period and increasing the frequency of the measurements. Since the material is sensitive enough to allow measurements of smaller doses, the only difficulties in building a faster dosimetry system are of an engineering nature, and imply using faster data acquisition and computation hardware

The inset in figure 5.21 shows the standard deviation of each set of three measurements performed at each dose rate. The reproducibility in measuring the dose rate varies between approximately 5% and 0.2% (1 S.D.), larger at lower dose rates. Presumably, the errors at lower dose rates are induced by the limited dynamic range of the photomultiplier tube (PMT), caused by the very short OSL integration interval. The PMT starts to exhibit nonlinear properties at approximately $10^7 cps$ (counts per second), which translate into 10^3 counts per $100\mu s$ data point. Presumably, switching from the PMT with TTL output to an analog light detector would improve the dynamic range of the measurable doses.

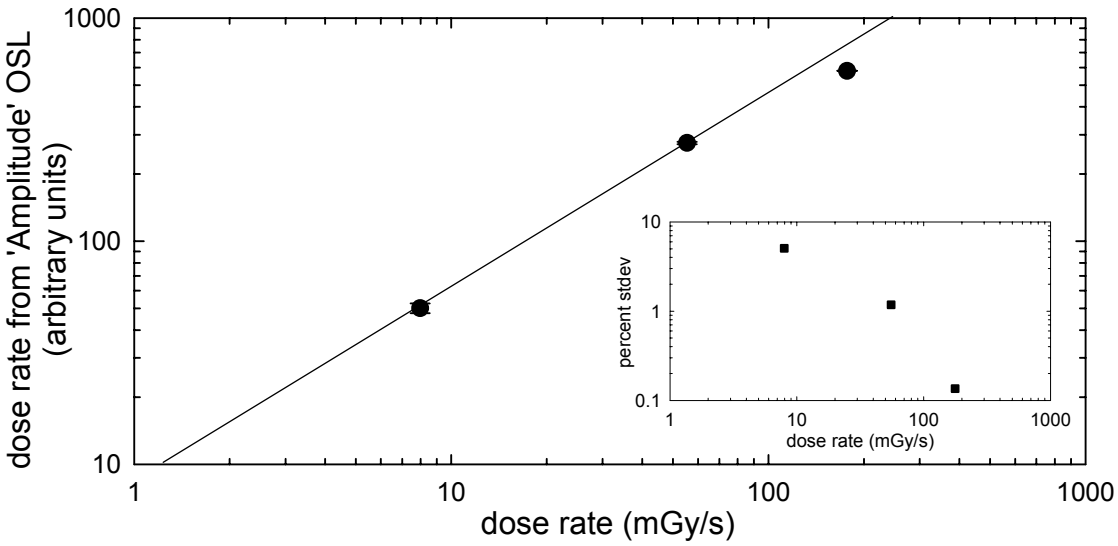

Fig. 5.21: Dose rate response of fiber KBr:Eu-2. The inset shows the standard deviation of the sets of 3 measurements performed at each dose rate

5.6. Conclusions related to the real-time OSL of KBr:Eu

i. The Europium-doped alkali halides allow for fast dose measurements. The OSL signal can be bleached rapidly to background level over time intervals on the order of milliseconds.

ii. In the particular case of KBr:Eu, efficient optical stimulation can be performed in the red region of the spectrum. Since the luminescence peaks in the blue region (430*nm*), inexpensive optical filtration can be used to separate the signal of interest (luminescence) from the stimulation background.

iii. Long-term effects leading to an increase in the OSL sensitivity with absorbed dose are visible in KBr:Eu, and can be attributed to the build-up of a slow component in the OSL decay. Correcting algorithms that separate the fast component of the OSL decay have been developed and successfully tested.

iv. The rate at which the dose is measured can be further improved. Limitations on our system are electronic and computational in nature, and are not imposed by the material properties.

CHAPTER SIX

DATA OBTAINED FROM CLINICAL IRRADIATIONS

6.1. General considerations

The tests performed so far on both dosimetry systems, and presented in the previous two chapters, consisted of irradiations under ^{90}Sr (β) and X-ray sources available in the radiation physics laboratories at Oklahoma State University, Stillwater OK, and at Risø National Laboratory, Roskilde, Denmark. The energy spectrum of the radiation investigated so far differs substantially from that of the radiation customarily used in the radiotherapy of cancer. Aside from fulfilling the need to confirm the results previously obtained with laboratory sources, the transition to clinical irradiators seeks answers to a whole new set of questions related to the performance of the OSL systems. Among them, the most important issue is perhaps related to the dependence of the luminescence response of the dosimeter on the radiation energy.

The results reported in this chapter were obtained from irradiations performed with several teletherapy sources (linear accelerators – LINACs) of various types. A description of the location, type and specifications of each irradiator is presented in table 6.1.

The original Al_2O_3:C portable reader was tested with all of the irradiators enumerated in table 6.1. The idea to use alternative OSL materials arose only later in the course of the project, allowing us to test the KBr:Eu OSL reader only during the September 2003 irradiations performed in Fort Collins. The two OSL materials will be treated individually in separate sections of this chapter, and specific conclusions will be drawn for each one of them.

Location	Fort Smith, AR	Malmö, Sweden	Malmö, Sweden	Fort Collins, CO
Dates experiments performed	April 2003	May - June 2003	May - June 2003	September 2003
LINAC type	Varian	Varian 2100C	Philips (Elekta)	Philips (Elekta)
Variable dose rate	Yes	Yes	Yes	No
Available energies photons (*MV*): electrons (*MeV*):	6, 10 6, 9, 12, 15, 18	6, 18 12, 16	4, 10 10	6 5, 6, 7, 10, 12
Phantom type	water	solid water	solid water	water
Materials used	Al_2O_3:C	Al_2O_3:C	Al_2O_3:C	Al_2O_3:C, KBr:Eu

Table 6.1: Specifications of the clinical irradiators used for the testing of the OSL dosimetry system

6.2. Clinical dosimetry based on OSL of Al_2O_3:C

6.2.1. General shape of the raw and processed RT-OSL signal

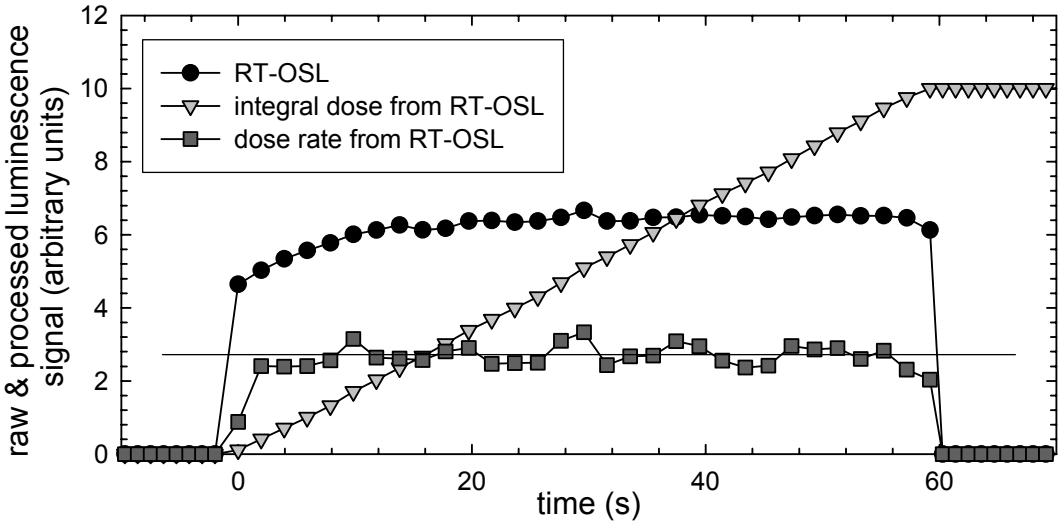

Fig. 6.1: RT-OSL, integral dose calculated from RT-OSL, and calculated dose rate for a 1minute irradiation of a F52 sample with 12*MeV* electrons

The luminescence signal presented in figure 6.1 was collected from a F52 Al_2O_3:C sample ($480\mu m$ diameter) during a 1minute irradiation with $12MeV$ electrons, at a dose rate of $67mGy/s$. After the subtraction of RL, the RT-OSL signal has a shape described by the black circles in fig. 6.1. From this signal, both the integral dose (light grey triangles) and the average dose rate absorbed between stimulations (dark grey squares) can be obtained as a function of time. Even though the RT-OSL signal presents an evidently increasing trend during the irradiation, the dose rate calculated from it promptly reaches a constant value, and thus confirms the ability of our algorithm to correct for the increase in sample sensitivity. The integral absorbed dose is then obtained as the integral over the measured dose rate, and shows a linear increase in time.

6.2.2. Signals of interest in the RT-OSL decay: RL and OSL

The dosimeter sample used for the bulk of the clinical experiments was the previously mentioned F52 Al_2O_3:C fiber shaped single crystal ($480\mu m$ diameter). In order to assure minimal losses in both the stimulation and luminescence light in the optical fiber cable, the sample was attached to a short ($1.5m$) FT-600-UMT (Thorlabs) silica fiber.

As described in chapter 4, the luminescence from the dosimeter being irradiated is monitored in the course of the experiment both in the absence of optical stimulation and with laser stimulation applied. During experiments performed with the ^{90}Sr source, the RL (background) signal measured in the absence of optical stimulation was consistently found to be one order of magnitude less intense than the OSL signal. Comparatively, the relative background levels measured during the irradiations with the VARIAN Clinac® in Fort Smith were found to be comparable with, and sometimes even larger than the OSL

signal. The new situation, showing the large relative RL/background intensity measured during the LINAC irradiations is presented in figure 6.2, for both photons and electron beams.

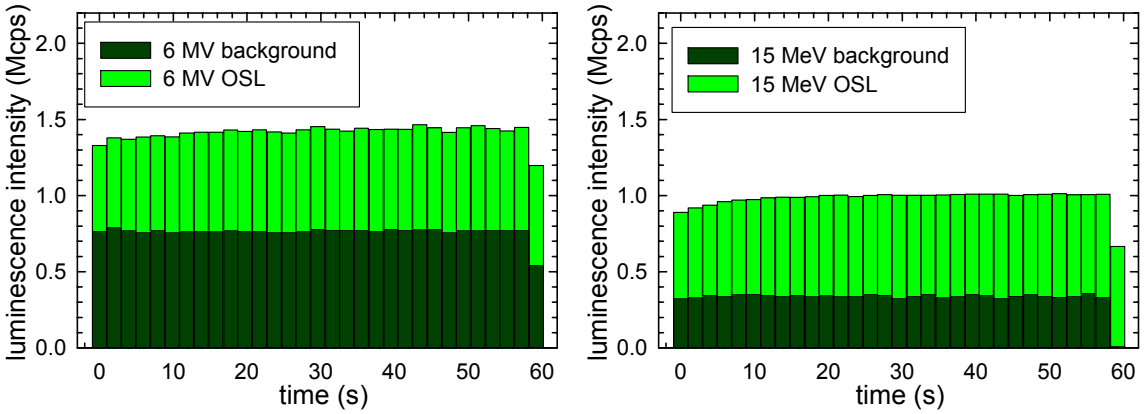

Fig. 6.2: RL/background and OSL signals from an F52 sample, attached to a 1.5m-long optical fiber, irradiated with 6MV photons and 15MeV electrons

Both irradiations in figure 6.2 were performed at the same dose rate: 67mGy/s. It can be noticed that in spite of the similar experimental conditions, radiation of different quality generates luminescence backgrounds that can substantially differ in intensity. At the same time, no important difference can be noticed in the equilibrium level of the RT-OSL $I_{OSL}(\infty)$.

The dramatic increase in the RL/background luminescence level could not be immediately explained. Since the OSL signal of interest is isolated via a subtraction of two signals that contain the same amount of luminescence background, as described in relation (3.5), the intensity of the RL/background level should be irrelevant in the outcome of the measurement. However, the background increase was found to reduce the

signal-to-noise ratio (SNR) of the acquired data, leading to a larger scatter in the individual dose rate estimations, and therefore a closer investigation of the effect was deemed necessary.

Initially, an electrical interference problem was suspected; however, additional shielding and grounding procedures preformed on the portable reader did not help recovering the relative OSL intensity expected from initial ^{90}Sr source irradiations.

It was later determined that the background signal increase does not originate in the fiber sample. Rather, if the reader is placed at a small distance from the LINAC head, the scattered radiation generates scintillations in the luminescence detector itself (PMT). The same phenomenon can be noticed to affect the functioning of the video cameras monitoring the irradiation area, in the form of sparks that appear on the video monitor during the irradiation. Since the amount of scattered radiation increases with an increase in the irradiation dose rate, so does the rate at which scintillations in the PMT occur. Also, the fact that the photons (X-ray radiation) scatter more easily than electrons explains the larger intensity of the measured RL/background signal at the same dose rate.

6.2.3. Energy dependence of the OSL response

The energy dependence of the OSL from the F52 Al_2O_3:C sample, connected to a 1.5*m*-long FT-600-UMT fiber, was studied by irradiating it at a LINAC output of 400*mu* (monitor units), with radiation of different quality: 6 and 10*MV* photons, and 6, 9, 12, 15, 18*MeV* electrons. The irradiations were performed in a water phantom, in a 100*cm* fixed source-to-skin distance (SSD) geometry, and the depth at which the detector was placed was chosen as the depth of maximum dose (d_{max}) for each radiation quality. Thus the dose

absorbed in the dosimeter amounted in each case for 4*Gy*, and was delivered at a rate of 67*mGy*/*s*. Each data point plotted in figure 6.3 represents the integral dose calculated from the OSL signal for an irradiation with a particular radiation quality.

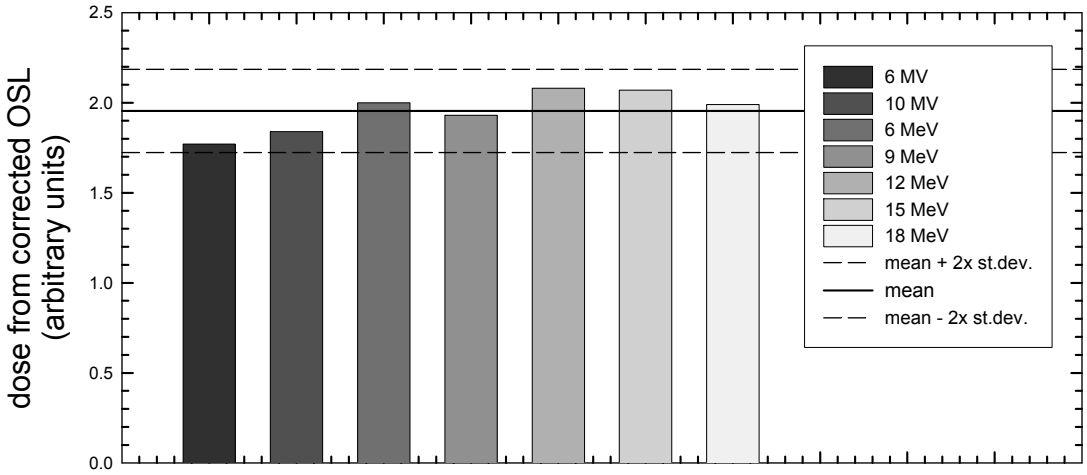

Fig. 6.3: Energy dependence of the OSL response from F52 under irradiation with 6 and 10*MV* photons, and 6, 9, 12, 15 and 18*MeV* electrons

From the data in figure 6.3, it can be stated that no evidence of a particle- or energy-dependent OSL response was found. The slight under-response of F52 under irradiation with photons might result from statistical fluctuations given by a larger noise than in the case of electrons, and is not statistically relevant.

6.2.4. Dose and dose-rate response of the corrected RT-OSL

The dose-rate response was studied by performing fixed-time irradiations at different dose rates on the F52 sample (1.5*m* FT-600-UMT optical fiber). The Varian Clinac® in Fort Smith was able to irradiate at 80, 160, 240, 320 and 400*mu/min*, corresponding to

dose rates (at the depth d_{max} in the water phantom) of 13, 27, 40, 53 and 67mGy/s.

Three electron (6, 12 and 18MeV) and two photon energies (6 and 10MV) were investigated. The average values of the dose rates from RT-OSL, obtained for each irradiation, and the associated standard deviations, are represented in figure 6.4.

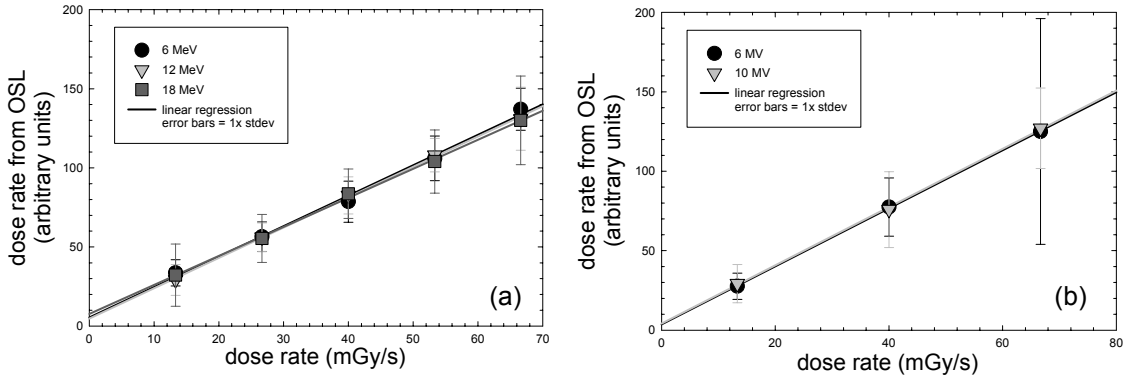

Fig. 6.4: Dose rate response of F52 (data points and linear fit) under Clinac® irradiation with (a) electrons and (b) photons of different energies

In all cases, data show a good linearity between the measured and the actual dose rates. The fact that the linear fit does not pass through the origin can be attributed to a light leakage into the PMT. Presumably, responsible for the leak is the imperfect filtration of the blue luminescence signal, which allows a small fraction of the very intense green stimulation light to reach the light detector.

The presented data offer additional evidence of the fact that the OSL response of the sample is energy- and particle-type-independent. This can be noticed by a direct comparison of the intensities of the OSL responses at different radiation types, expressed in figure 6.4 in the same arbitrary units.

The same results can also be interpreted as an indication of the good linearity of the dose

response, since the integral dose is calculated as the sum of the individual dose fractions (dose rate estimations). In this case, the accuracy in the determination of the integral dose is better reflected by the standard error of the set of dose fractions, instead of the standard deviation represented in figure 6.4. The relation between the two statistical parameters is given by the formula:

$$\sigma_m = \frac{\sigma}{\sqrt{N}} \qquad (6.1)$$

where σ_m is the standard error (standard deviation of the mean), σ is the standard deviation of the data set, and N is the number of individual dose rate estimations in a particular data set. According to (6.1), the accuracy in determining the integral dose increases with the number of individual dose fraction measurements, for a constant standard deviation of the data set. Each irradiation depicted by the results in fig. 6.4 had duration of 1 minute, and during this time 29 dose fraction samples were collected. With this information, the percent standard error can be calculated for each irradiation in fig. 6.4. The results are shown in figure 6.5.

The data indicate an average standard error in the measurement of the integral dose on the order of 5%, for 1 minute long irradiations. According to relation (6.1), a 4-fold reduction in the irradiation time would increase the uncertainty in the measured integral dose by a factor of 2. Generally, the errors decrease with the increasing dose rate, due to the larger OSL signal, and to the more abrupt OSL decay that allows for more accurate estimation of the shape coefficient K_S. Also, the errors appear to be slightly larger in the case of photons than for electrons, most probably due to the larger measured values in the RL/background level.

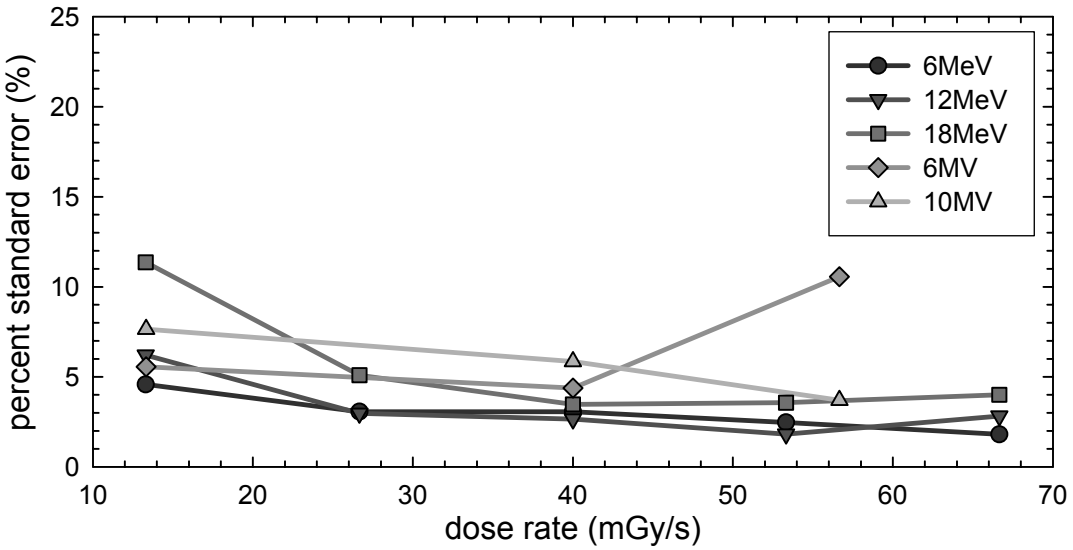

Fig. 6.5: Percent standard errors of the integral doses from RT-OSL at irradiation with different dose rates of 6, 12, and 18*MeV* electrons, and 6 and 10*MV* photons

6.2.5. Effects of longer fibers

There are two possible approaches that would lead to a decrease in the scattered radiation reaching the PMT. One would involve shielding the reader in a lead (Pb) case of appropriate thickness. In the other approach, the reader could be placed at a larger distance from the LINAC head, so that the scattered radiation would be reduced to a minimum. In this case, an optical fiber of an appropriate length should be used to transport the stimulation light from the laser to the sample, and the luminescence from the sample to the PMT.

Either approach also introduces some disadvantages, such as the need for a specifically designed, heavy shielding for the first case, or an increase in the absorbed light in the fiber for the second. We opted for the second approach, in which a long fiber was used for the light transport. The procedure was first implemented for the irradiations with a

Philips LINAC in the Malmö University Hospital, Sweden, when a new probe was assembled by attaching the F52 Al_2O_3:C dosimeter to a 15m-long, SMA terminated, plastic ESKA fiber with a core diameter of 1mm. The relative intensities of the RL and OSL signals obtained with the new probe can be observed in figure 6.6. Data points represent the luminescence measured from the sample, and integrated over time intervals of 100ms. The first 3 data points represent the RL, and are obtained with the shutter closed. The shutter is opened at $t = 300ms$, and after a 100ms transition period, OSL is measured between $t = 400ms$ and $t = 800ms$ (4 data points). After the shutter is closed at $t = 800ms$, the signal decays back to the RL level.

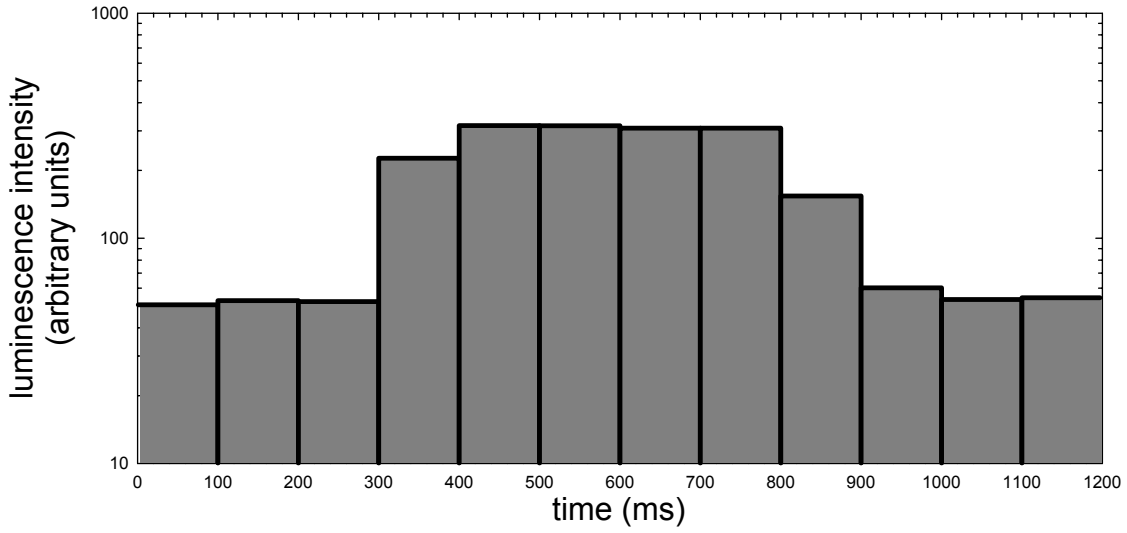

Fig. 6.6: Luminescence signals (RL and OSL) from fiber F52, attached to a 15m-long ESKA optical cable, irradiated with 6MV photons at a dose rate of 33mGy/s

The diameter mismatch between the crystal ($480\mu m$) and the fiber cable (1mm) was bound to worsen the quality of the optical coupling. Due to the smaller amount of

stimulation light reaching the sample, the optically stimulated luminescence decays more slowly. It is also expected that, because of the slower decay in the OSL signal, the uncertainties in the measured surrogate shape coefficient would increase. Still, as a result of placing the reader farther away from the irradiation area, the background luminescence intensity was reduced to a level similar to the one observed during ^{90}Sr irradiations.

6.2.6. Repeatability of the OSL measurements with Al_2O_3:C

In order to study the reproducibility of the integral dose measurements, multiple irradiations with both photons and electrons were performed on the F52 sample with the Philips LINAC in the Malmö University Hospital. The reader was placed in a radiation-free environment outside the treatment room, and was connected to the dosimeter sample by the 15*m*-long, 1*mm*-diameter ESKA fiber. The reproducibility was assessed by performing three sets of measurement on the sample, each set containing five irradiations under the same dose and dose rate conditions. The dose and / or the dose rate were changed between the different irradiation sets, as shown in table 6.2.

Irradiation set #	1	2	3
Integral dose (*Gy*)	2.00	1.00	4.00
Dose rate (*mGy*/*s*)	33	33	67

Table 6.2: Irradiation parameters of the reproducibility experiment

The experiment was performed for irradiations with both 10*MV* photons and 10*MeV* electrons. In each case, the dosimeter was placed at the corresponding depth of dose-maximum (d_{max}) in a structure consisting out of solid water. All the irradiations were

performed in 100*cm* fixed-SSD geometry. The results of the integral dose measurements are shown in figure 6.7 for (a) photon and (b) electron irradiations.

Data in figure 6.7 indicate a slightly larger OSL response for photons than for electrons, opposite to the energy dependence described in figure 6.3, providing further evidence that supports the hypothesis of a RT-OSL response essentially independent of the radiation quality. A further statistical analysis on the data in fig. 6.7 is plotted in figure 6.8, as the percent standard deviation in the data sets of integral dose.

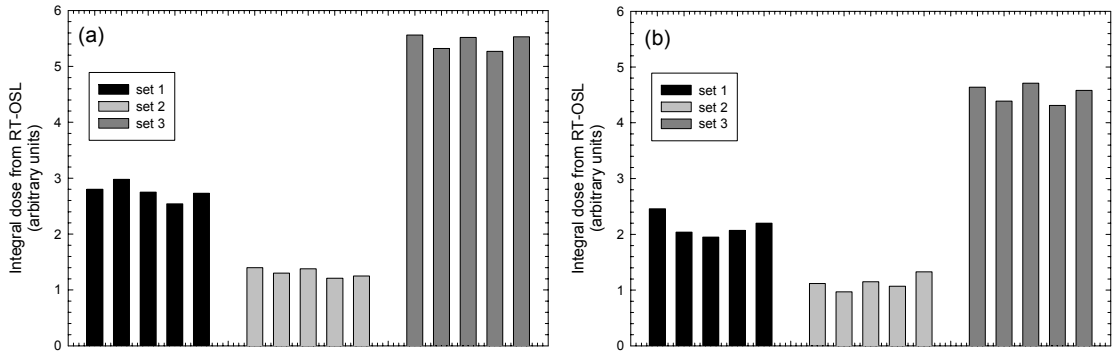

Fig. 6.7: Results of the reproducibility experiment performed on the F52 / 15*m* ESKA sample, irradiated with (a) 10*MV* photons and (b) 10*MeV* electrons

Conversely to the case described in figure 6.5, the reproducibility is better for photon measurements than for electrons. In both cases, it increases with both dose and dose rate. The outcome of this experiment suggests that the sources of uncertainty have changed after the longer fiber cable has been employed. If for the statistical data presented in fig. 6.5 the larger background signal affected negatively the photon measurements, the precision of the measurements presented in figure 6.8 is limited mainly by the level of the

luminescence signal. Since, for reasons having to do with the imprecision in placing the dosimeter at the required depth of maximum dose, the signal for photons was larger (as shown in figure 6.7) the precision of the determinations was better.

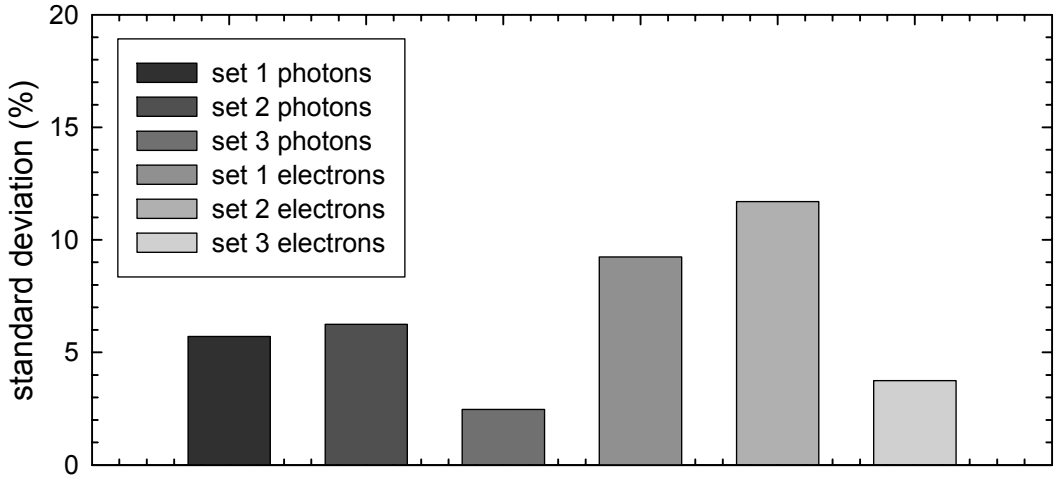

Fig. 6.8: Statistical analysis of the reproducibility test presented in figure 6.7

For reason related to statistical analysis, as described in relation (6.1), the standard error of the dose rates presented in figure 6.5 and the standard deviation of the integral doses presented in figure 6.8 can be directly compared to obtain a measure of the reproducibility of the dose rate measurements. The average value of approximately 5% taken by both quantities suggests that switching to a longer fiber did not make a significant difference in the measurement reproducibility. We can speculate that the gain in the signal-to-noise ratio, determined by the decrease in the RL/background level, was compromised by the additional light losses in the longer fiber cable, and by the lower quality of the dosimeter-to-fiber optical coupling.

6.2.7. Dose deposition profile measurements

The graph in figure 6.9 depicts the results of an irradiation experiment performed in Fort Collins, CO. The F52-1 sample, attached to a 15*m*-long FT-600-EMT Thorlabs fiber, was repeatedly irradiated at a constant LINAC output of 100*mu*, while being immersed at different depths in a water phantom. Since the dose delivered by the LINAC at the depth of dose-maximum in the water phantom was always the same, the dose absorbed in the dosimeter was only dependent on the depth at which the dosimeter was placed. Three irradiations with 7*MeV* electrons were carried out at each depth, using a 100*cm* constant-SSD geometry.

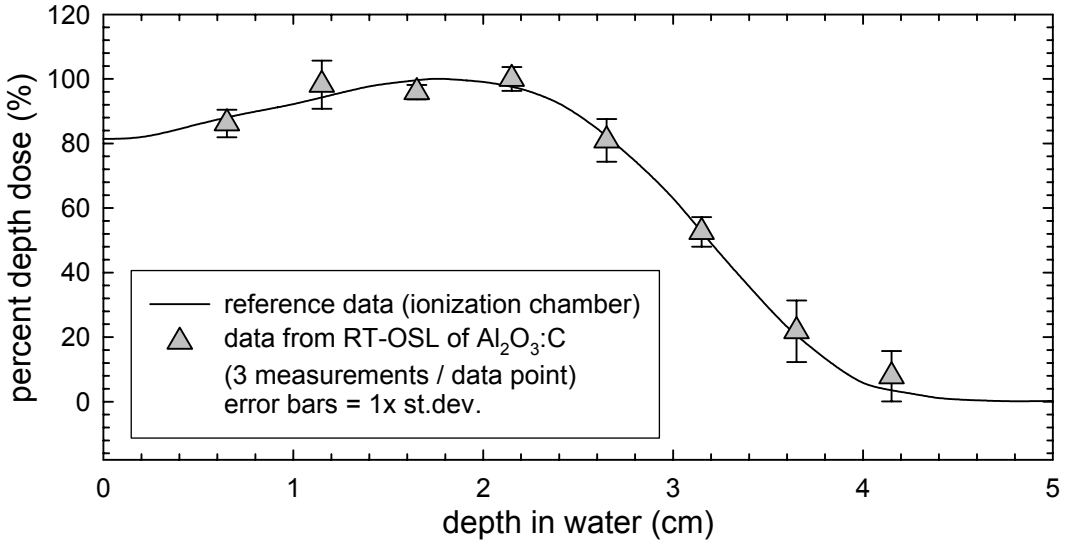

Fig. 6.9: Dose deposition profiles for 7*MeV* electrons, showing data obtained from both RT-OSL of Al_2O_3:C and from reference (ionization chamber) measurements

An insufficiency of the green-rejecting filtration in front of the PMT allowed a relatively large amount of 532*nm* stimulation light (~15,000*cps*) to reach the PMT. This was

corrected for during the post-irradiation processing of the data by subtracting the corresponding amount from the OSL+RL luminescence signal.

The integral doses from RT-OSL were normalized to the maximum measured value (the dose at d_{max}), and represented as grey triangles in figure 6.9. In the same figure is plotted the reference dose deposition profile, obtained via measurements with ionization chambers.

Good accuracy is indicated by the correlation between the dose estimations from OSL and reference data. The reproducibility of the measurement lies between 2.2% and 9.5%, (standard deviation of the sets of 3 measurements) and is better at higher doses.

Either 9 or 10 individual dose fractions were measured during each 100*mu* irradiation.

6.2.8. Conclusions on clinical dosimetry based on OSL of Al_2O_3:C

We have succeeded in developing a device, an associated data acquisition procedure and an associated mathematical algorithm, based on the OSL of a fiber-shaped Al_2O_3:C crystal, that can successfully perform near-real-time (on-line) dose measurements in the range of doses and dose rates customarily used in external beam radiotherapy (teletherapy), with a precision of the RT-OSL integral dose estimations on the order of 5% (1 standard deviation) under clinical conditions.

The dose determinations from RT-OSL are in good agreement with measurements performed by traditional dosimeters, as shown by the comparison of the depth deposition profile obtained by two different methods (RT-OSL and ionization chamber). The integral dose can be updated with a frequency of approximately 0.5*Hz* (~2*s* / data point).

Both the material properties and instrumentation issues impose limits on the further

increase in the speed and the precision of the measurements.

A major factor limiting the measurement frequency is the presence of a significant delayed OSL (DOSL) signal in the investigated samples. In order to be able to properly measure the intensity of the RL/background signal, the DOSL has to completely fade away, and thus a time interval of up to $1s$ has to be allowed between successive laser stimulations, depending on the quality of the Al_2O_3:C sample.

An additional constraint imposed by the material is the requirement that the stimulation light must be applied in a spectral region situated in the vicinity of the luminescence signal of interest. Accordingly, heavy filtration is needed to separate the weak luminescence from the intense stimulation light, which results in an important decrease in the OSL signal reaching the PMT.

The OSL decay takes place, even at high stimulation power, over long periods of time on the order of several seconds. Besides leading to imprecision in calculating the value of the shape coefficient K_S, stimulating the OSL for time intervals that are short compared to the specific decay time results in densely populated charge traps, and this pushes the OSL signal from the dosimeter from the linear to the non-linear region of the dose response.

The ultimate time boundary is represented by the same material characteristic that makes Al_2O_3:C a good candidate to be used in pulsed OSL (POSL) mode: the long lifetime ($35ms$) of the *F* luminescence center. Due to the slow rise- and fall-time of the OSL, it is difficult to deal with continuous-wave (CW) laser applications requiring the stimulation light to be modulated at frequencies larger than $10Hz$ ($100ms$ / data point).

The instrumentation being used has to compensate for the material deficits: a powerful

laser is needed to provide stimulation light that causes the OSL to decay faster; also, expensive dichroic filters need to be used for separating the blue luminescence from the green stimulation. The high level of laser power transmitted through the beamsplitter, fiber collimator and optical fiber are likely to generate local thermal effects, leading to miss-alignments of the optical components and variation in their optical properties.

The engineering issues related to building a commercial system require further research; among the items of interest are improving the coupling between the dosimeter sample and the optical fiber, both from the optical and the mechanical points of view. Ideally, an optical index-matching compound should be used at the sapphire ($n \cong 1.78$) and fused silica ($n \cong 1.46$) interface, to maximize the luminescence collection in the light guide.

Other improvements can be made in terms of the optical filtration of the luminescence light from the laser stimulation background; choosing optical fiber cables that ensure minimal absorption of luminescence and stimulation light; and eliminating ambient light leakage in the reader (light-tightness).

6.3. Clinical dosimetry based on OSL of KBr:Eu

6.3.1. The shape of the OSL signal

In the case of KBr:Eu, each laser stimulation pulse completely depletes the OSL signal previously accumulated in the sample. The irradiations carried out with the Philips Elekta LINAC in Fort Collins, CO, resulted in typical OSL decays as shown in figure 6.10. Each decay curve consists out of 100 data points collected at a frequency of $5kHz$ ($200\mu m/d.p.$). Laser stimulation is applied every time for $15ms$, or 75% of each $20ms$ interval. In addition to the $20ms$ in which the data acquisition takes place, the computer

needs an extra amount of time for data processing, bringing the total time required for estimating each dose fraction to a value of approximately 60*ms*. Accordingly, the integral dose is updated at a frequency of approximately 15*Hz*.

The sample under investigation was KBr:Eu-2, attached to a 15*m*-long FT-600-EMT Thorlabs silica fiber. Besides the OSL maxima that consistently appear at the same position in the data array, thus confirming the good synchronization of the data acquisition sequence with the application of laser stimulation, other peaks appear at random positions in the OSL decays, with a frequency and an intensity that depend on the radiation quality used. The luminescence pulses also appear in the data when a bare fiber (without a dosimeter attached at the distal end) is irradiated, but with an intensity which is lower than the intensity measured with the KBr:Eu sample present.

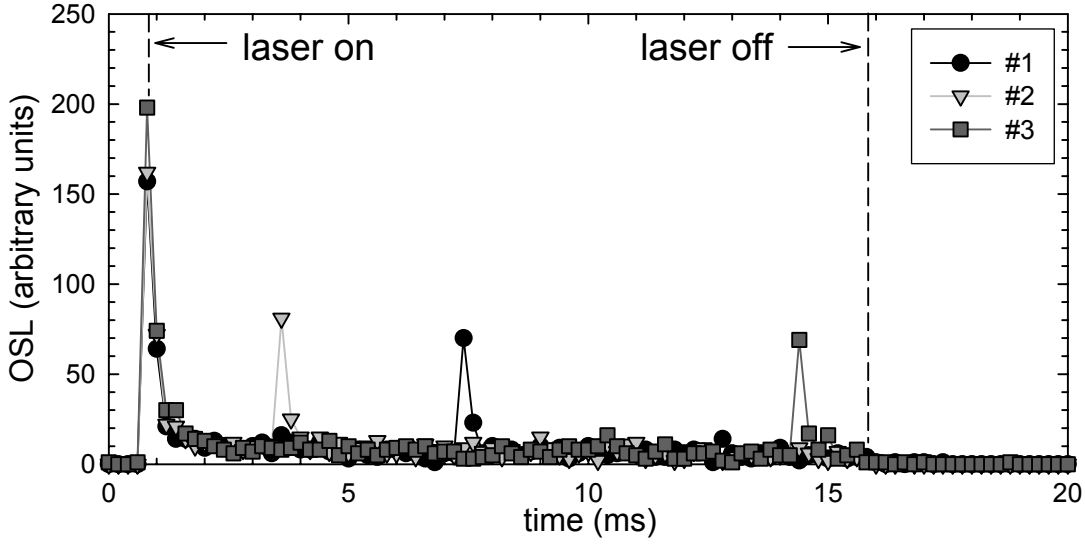

Fig. 6.10: Typical OSL decays (3 individual measurements) from the KBr:Eu-2 / 15*m* FT-600-EMT fiber sample, during irradiation with 5*MeV* electrons (Philips LINAC in Fort Collins, CO)

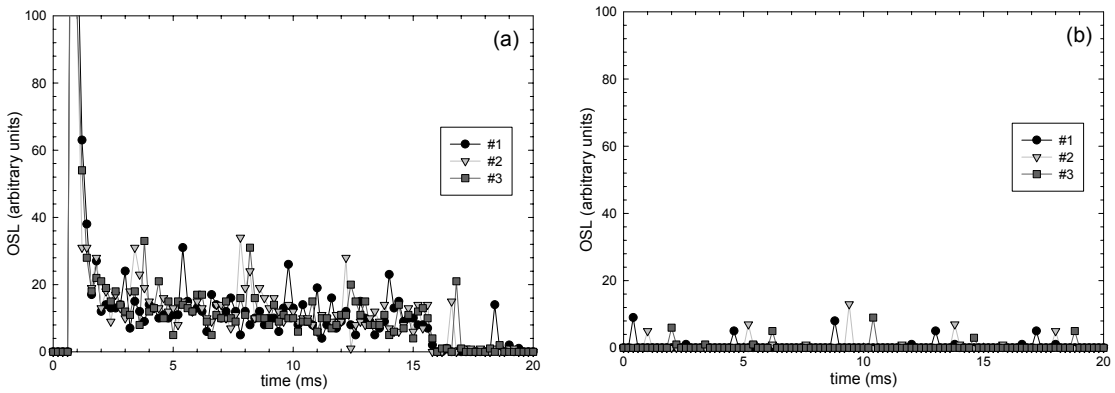

Fig. 6.11: Typical OSL signals from (a) the KBr:Eu-2 / 15*m* FT-600-EMT fiber sample and (b) the 15*m* FT-600-EMT bare fiber, during irradiation with 6*MV* photons

Figure 6.11 presents typical OSL decays obtained from both (a) a KBr:Eu-terminated and (b) a bare optical fiber, irradiated with 6*MV* photons. A pattern in the occurrence of the luminescence pulses is evident; the time delay between successive pulses is constant during irradiations with the same radiation quality. The explanation of the observed phenomenon is found in the technical literature describing the functioning of the medical irradiators, which indicates [40] that the radiation from LINACs is delivered in pulses (rather than in continuous-wave mode).

Unless the irradiation pulses are temporally correlated with the OSL data acquisition sequence, they appear as random supplemental luminescence spikes during the data acquisition process, and may result in an increase in the noise level of the measurements.

6.3.2. Energy dependence and reproducibility of the OSL from KBr:Eu

The energy dependence of the OSL response from KBr:Eu was studied by comparing the integral doses obtained from the RT-OSL signal during irradiation with different

radiation qualities. Both electrons (of energies 5, 6, 7, 10 and 12*MeV*) and photons (6*MV*) were used for irradiations. For each radiation quality, the dosimeter of the KBr:Eu-2 / 15*m* FT-600-EMT fiber probe was placed at the corresponding depth of maximum dose in a water phantom and three irradiations, delivering the same dose of 1*Gy*, were performed. The average integral doses from the 'amplitude algorithm' described in section 5.5 are plotted for different radiation quality in figure 6.12. Also shown are the standard deviations of each set of integral dose measurements, which serve as a factor that quantifies the measurement reproducibility.

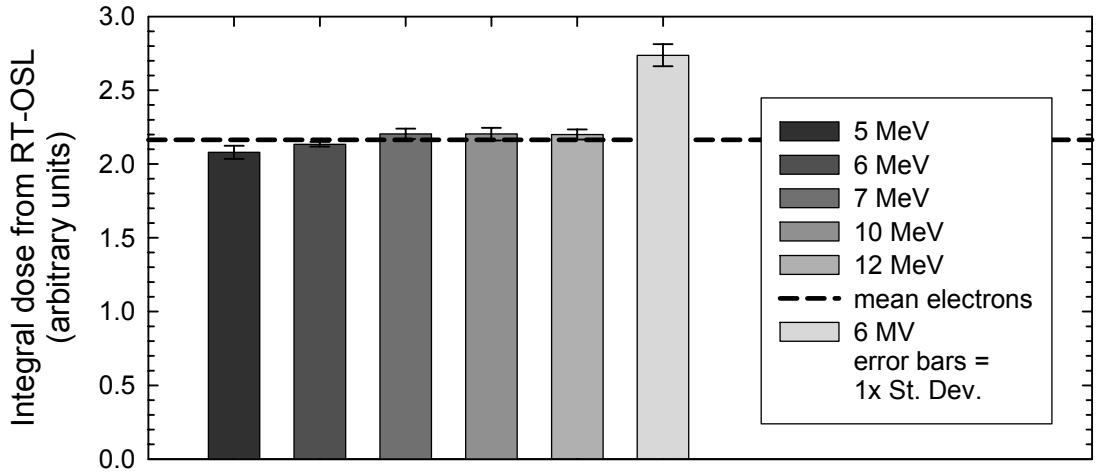

Fig. 6.12: Particle- and energy-dependence of the OSL response from the KBr:Eu / 15*m* FT-600-EMT fiber sample

Data indicate low (if any) energy dependence for electron irradiations. The OSL response for photons is larger than for electrons, but the limited data set prevents us to extract a definite conclusion in this regard.

Figure 6.13 shows the percent standard deviation of the sets of measurements presented

in figure 6.12. In all cases, the reproducibility of the dose estimation from OSL is better than 3% (at 1 standard deviation).

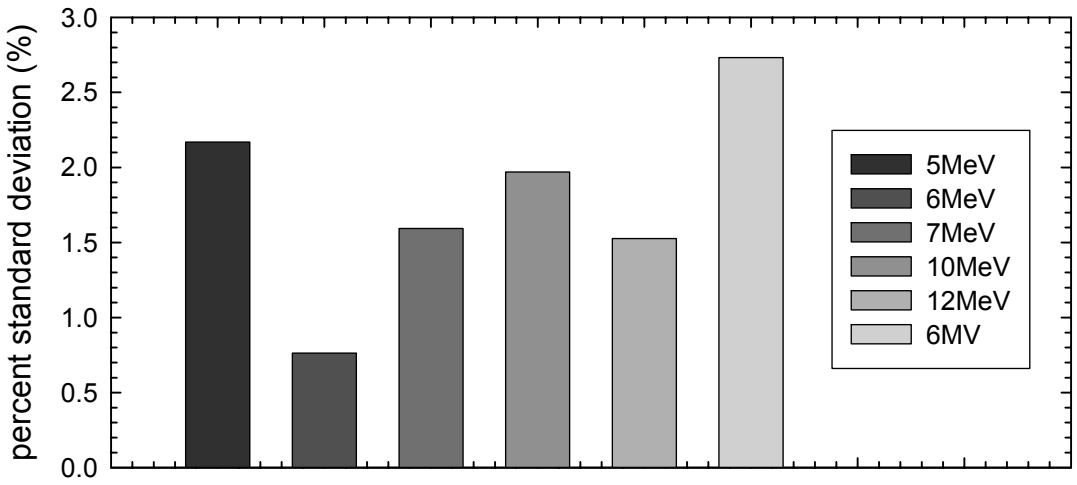

Fig. 6.13: Statistical analysis of the data presented in figure 6.12: reproducibility

6.3.3. Dose deposition profile from the RT-OSL of KBr:Eu

Similar to the case of Al_2O_3:C, the dose-rate response from the RT-OSL of KBr:Eu was studied by performing repeated 100*mu* irradiations with the dosimeter placed at several depths in the water phantom. As described in section 6.2.7, 3 irradiations were carried out at each depth, in 100*cm* fixed-SSD geometry. The results of the experiment are plotted in figure 6.14.

The correlation between the measurements performed by the two different methods, quantified by the weighted average of the percent difference in all the pairs of dose measurements, was calculated to be approximately 2.8%. In comparison, the same quantity measured for the dose deposition profile form the RT-OSL of Al_2O_3:C had a slightly larger value of 3.7%.

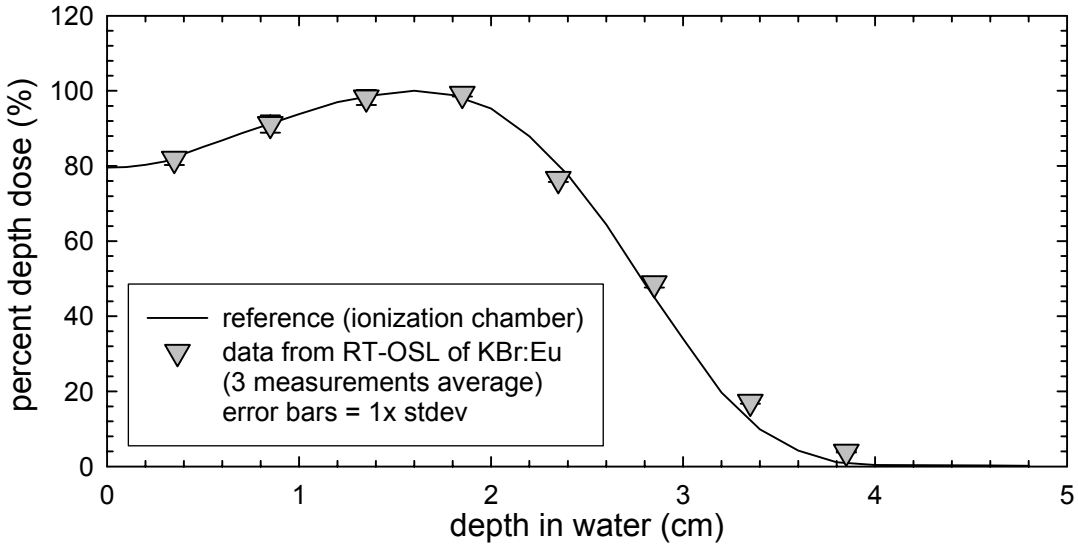

Fig. 6.14: Dose deposition profiles for 6*MeV* electrons, showing data obtained from both RT-OSL of KBr:Eu and reference (ionization chamber) measurements

The reproducibility of the measurements, quantified by the standard deviations of the sets of 3 integral dose estimations at the same depth in the water phantom fall in the range between 0.76% and 5.15%. The number of individual dose estimations during any 100*mu* irradiation was larger than 300 in all cases.

6.3.4. Conclusions on clinical dosimetry based on OSL of KBr:Eu

We have succeeded to implement a fast fiber dosimetry method based on the optically stimulated luminescence of KBr:Eu. The updates in the dose estimation can be achieved at frequencies of approximately 15*Hz*. A high spatial resolution is achieved by using probes having sensitive volumes (dimensions of the dosimeter) of less than $1mm^3$. The system is able to perform accurate measurements with good reproducibility in the range of doses and dose rates customarily used in teletherapy.

The brightness of the luminescence signal and the good response to optical stimulation in the red region of the spectrum are qualities that make KBr:Eu a good candidate for real-time dosimetry applications. A commercial product based on the OSL of KBr:Eu would be able to take advantage of the reduced costs related to the simple optical filtration and the inexpensive red diode lasers available on the market.

Further increase in the measurement frequency is possible by employing red lasers with higher optical power, which are already commercially available. However, in order to fully use the capabilities of the material, higher computation capabilities are required. The bottle neck in the dose update frequency is caused by the computation power available, rather than by the material properties.

An additional hardware problem was represented by the limited dynamic range (3 orders of magnitude) in the operation of the PMT. Typical photomultiplier tubes start exhibiting a non-linear behavior at counting rates of $10^7 cps$ (counts / second). If the luminescence signal is integrated over time intervals of $100\mu s$, only 10^3 counts can be measured for each data point without employing additional correcting algorithms.

Careful material engineering is expected to further improve the dosimetric properties of interest. Since fading is not an issue in the case of real-time applications, and since modern LINACS are able to perform irradiations at $1000 mu/min$ (up to $167 mGy/s$), the main material-related concern is raised by the limited range of linearity in the dose response of KBr:Eu. Measurement speed is also of importance in this regard: a faster system would be able to use the dosimeter in the linear region of its dose response, by reducing the irradiation time between two successive stimulation pulses, and thus the absorbed dose in the sample.

CHAPTER SEVEN

OTHER APPLICATIONS OF THE FIBER DOSIMETER

7.1. Two-dimensional mapping of dose distributions

In this section, we will analyze the possibility of using the fiber OSL dosimeter to obtain maps of the dose deposited in thin Al_2O_3:C layers. As described in the first chapter of this thesis, the measurement of the entrance and exit doses constitutes the most widely used quality-assurance (QA) procedure in radiation therapy. Instead of performing local dose measurements with point-detectors such as diodes or TLDs, dosimetry devices such as GAFChromic films can be used to obtain two-dimensional (2-D) maps of the entrance and exit doses. From these dose maps, the dose distribution in a plane containing the tumor, and perpendicular to the direction of the irradiation beam, can be estimated.

Thin layers of Al_2O_3:C powder having grain size on the order of $10-100\mu m$ are commercially available from Landauer, Inc., and constitute the active part of the Luxel® OSL dosimeter. The Al_2O_3:C powder is compacted using an adhesive material, and then deposited as a layer of uniform thickness between two transparent plastic sheets. The finite product resulted from the above manufacture process is in the form of long bands of plastic-coated Al_2O_3:C, with lengths of approximately 30*cm* and widths on the order of 2*cm*. These Al_2O_3:C 'ribbons' are subsequently cut into 2*cm*-long segments, and the resulting rectangles are incorporated into the Luxel® personal dosimetry badges.

Our experiments have focused on obtaining maps of the dose deposited in Al_2O_3:C by irradiation in a ^{90}Sr Beta source. The maximum dose delivered to the sample was on the order of 500*mGy*. The investigation of the post-irradiation OSL signal was performed

with the green stimulation OSL reader described in chapter 4. A bare optical fiber of the type Mitsubishi ESKA (plastic, 1*mm* diameter) was used to transmit the green stimulation to the sample, and the blue luminescence from the sample to the reader. The distal end of the light guide was partially melted in open flame to obtain a lens-like geometry, thus minimizing the angular dispersion of the stimulation light emerging from the fiber.

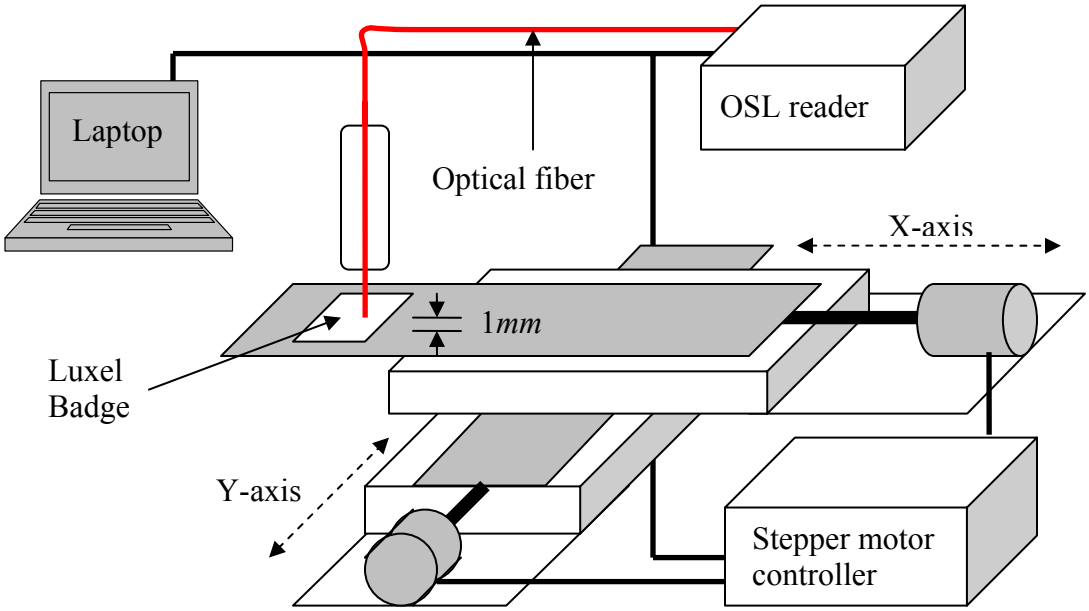

Fig. 7.1: Schematic diagram of the 2-D mapping experiment based on OSL of Al_2O_3:C, performed with the fiber reader on a pre-irradiated Luxel® Badge

The probing tip obtained in this manner was placed vertically at a distance of about 1*mm* (on the z-axis) above the flat Al_2O_3:C sample. The Al_2O_3:C film was laid on a two-dimensional translation stage capable of producing displacements in steps on the order of tens of microns along both the x- and the y-axis, and controllable by the same computer that was in charge of the data acquisition from and the control of the OSL reader. The

schematic experiment setup is presented in figure 7.1, and a picture of the mapping system in figure 7.2.

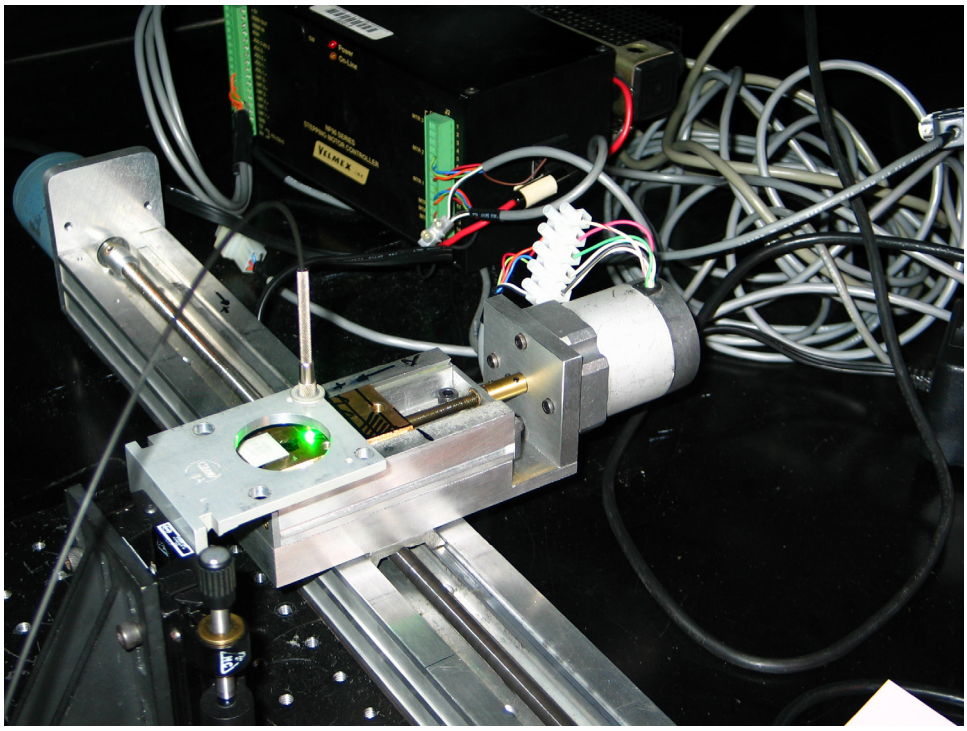

Fig. 7.2: Picture of the of the 2-D mapping experiment based on OSL of Al_2O_3:C, performed with the fiber reader on a pre-irradiated Luxel® Badge

With the fiber end situated above a certain region of the Luxel® layer, the laser was turned on for a time interval on the order of 100ms. Green light from the laser was projected from the bare end of the fiber on the Al_2O_3:C layer, and stimulated the emission of an OSL signal proportional to the dose previously deposited in the material. A fraction of the OSL signal was collected through that same optical fiber, transmitted at the OSL reader and measured at the light detector (PMT). While the stimulation that transmitted the green stimulation and the blue luminescence light was held fixed at a certain position,

the motorized stage moved the Al_2O_3:C sample between successive stimulations according to a predetermined pattern as described in figure 7.3, ensuring that the whole surface of the Luxel® was investigated.

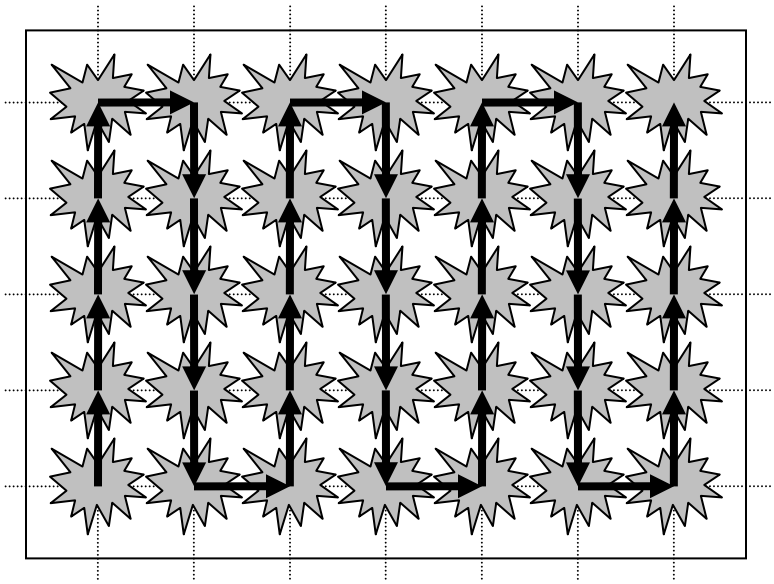

Fig. 7.3: Scanning pattern of the 2-D dose mapping system based on the green (Al_2O_3:C) OSL fiber reader

The entire procedure, consisting in the periodic stimulation & measuring of the OSL signal, and the advancement of the Al_2O_3:C layer to the new position, was incorporated into a LabVIEW virtual instrument (VI). Data acquisition and control was achieved by simultaneously using a National Instruments DAQ Card of the type 6062 (PCMCIA interface, connected to a 1*GHz* Intel Pentium III laptop PC) and the serial port of the computer. The DAQ card was used in conjunction with the OSL reader, and the serial port was used to control the 2-D motorized stage, through a Velmex stepper motor

controller. The user-interface of the dose-mapping VI is shown in figure 7.4.

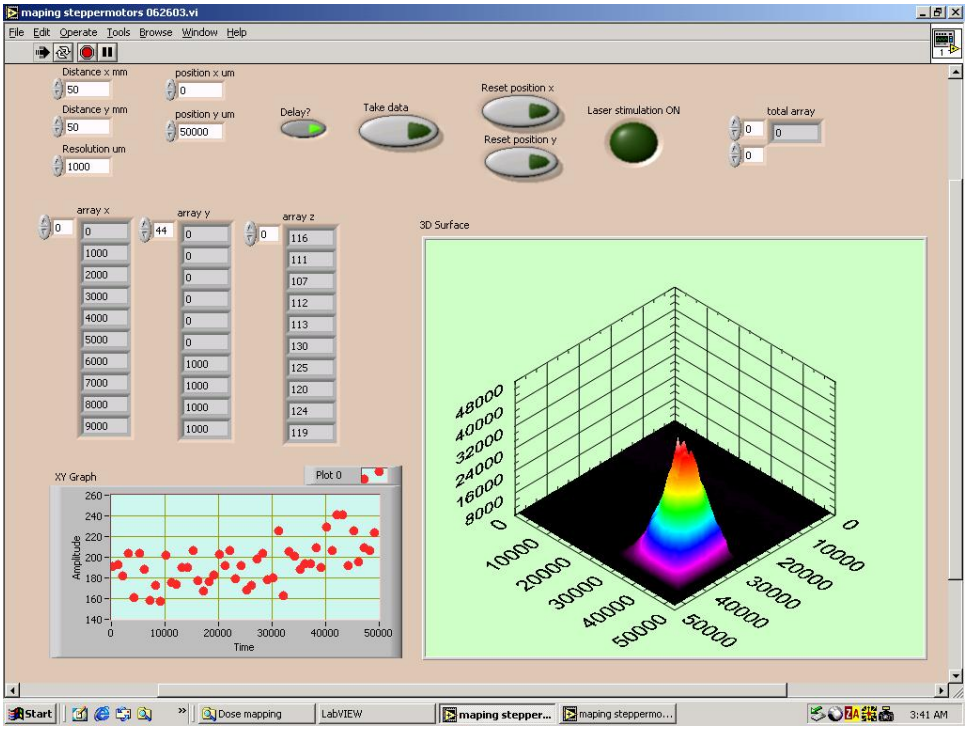

Fig. 7.4: User interface of the VI used for 2-D OSL mapping with Al_2O_3:C

As presented in figure 7.4, the experiment was set to scan a surface of 50x50mm^2, at a resolution of 1mm on both x- and y-axes. The 2-D dose distribution (in arbitrary units) is obtained in real time. A 3-D plot of the data obtained during the experiment shown in figure 7.4 is presented in figure 7.5, and indicates a relatively high degree of non-uniformity in the spatial distribution of the dose rate delivered by the ^{90}Sr source.

The procedure presents a simple alternative to obtain two-dimensional dose maps, and expands the possible applications of the fiber reader. Further investigation is needed for optimizing the operation of the 2-D mapping system, especially in the following aspects:

• Better collimation of the stimulation light emitted from the optical fiber;

• Improvement of the luminescence collection efficiency;

• Minimizing the cross-talk, i.e. the depletion in the OSL signal at a certain location by scattering of stimulation light applied to a neighboring location;

• Speed increase; primary limiting factor is the speed of the stage/motor assembly.

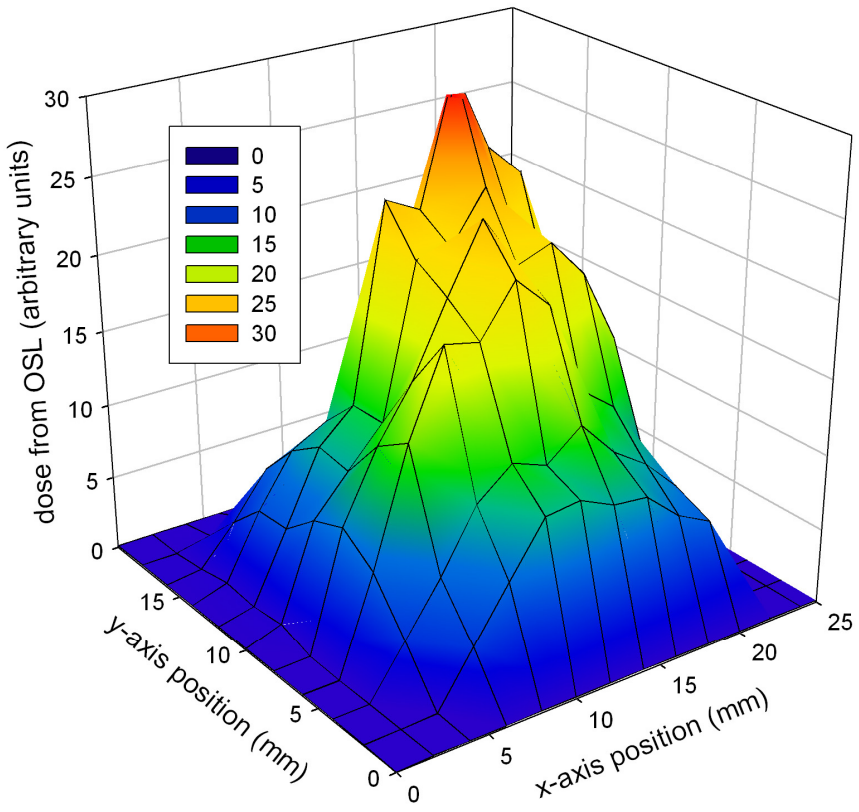

Fig. 7.5: Dose distribution of a ^{90}Sr beta source from the OSL of Al_2O_3:C

7.2. Low-dose applications

With the current elevated threat of terrorist attacks, there is an increasing interest shown by governmental agencies in employing effective sensors that would help safeguarding the ports of entry into the U.S. A special concern is raised by the possibility of illegal

importation of radioactive materials that could be used as starting materials in the manufacture of weapons of mass-destruction. Our OSL fiber detector shows some promising characteristics that would make its use for detection of radioactive material feasible:

1. The possibility of investigation of remote locations that are hardly accessible by other means, and
2. Ability to give real-time (on-line) readings.

In order to determine the minimum measurable dose by our KBr:Eu reader, we have used it in conjunction with a very weak ^{137}Cs radioactive source, able to deliver a radiation dose smaller than $1\mu Gy/s$. A KBr:Eu sample, attached to the end of a $15m$ long optical fiber, was irradiated for different periods of time on the order of tens to hundreds of seconds. In fact, we have used for these determinations the same KBr:Eu sample that was originally constructed for medical applications. In order to effectively measure low doses, the sensitivity of the OSL reader was improved by decreasing the amount of filtration in front of the PMT, from $13mm$ to $9mm$ total thickness of 5-58 Kopp filters. As will be seen in what follows, the increase in the luminescence background was negligible.

The timing parameters chosen for the experiment were somewhat similar to the ones used for medical applications: since the OSL from KBr:Eu decays extremely fast, a data acquisition speed of $100\mu s/d.p.$ was chosen. At every measurement, the OSL was recorded for a total of $5s$, the stimulation being applied starting at $0.25s$ after the initiation of the data acquisition, and extending up to $0.25s$ before the end of the $5s$ time interval, as shown in figure 7.6.

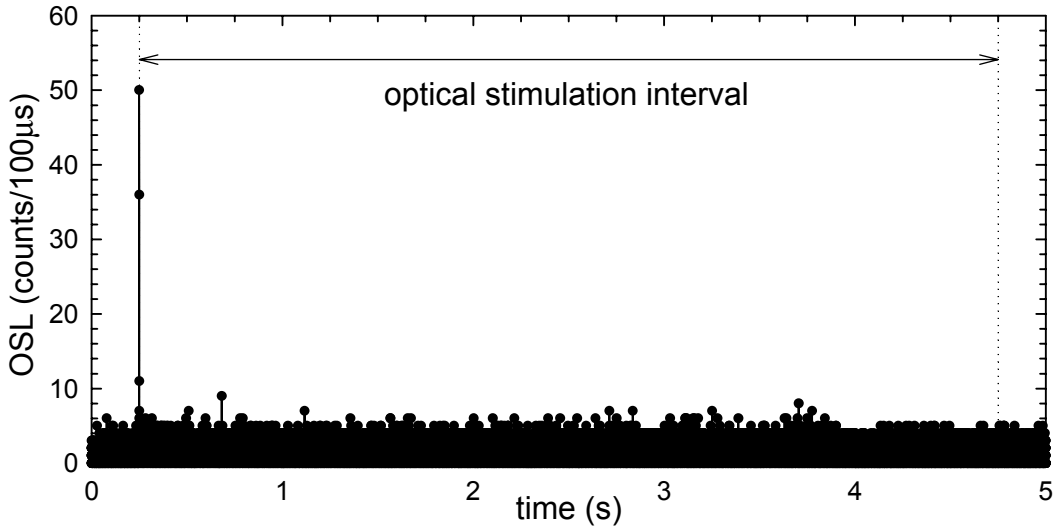

Fig.7.6: OSL signal from KBr:Eu following irradiation with $220\mu Gy$ of gamma radiation from a ^{137}Cs source

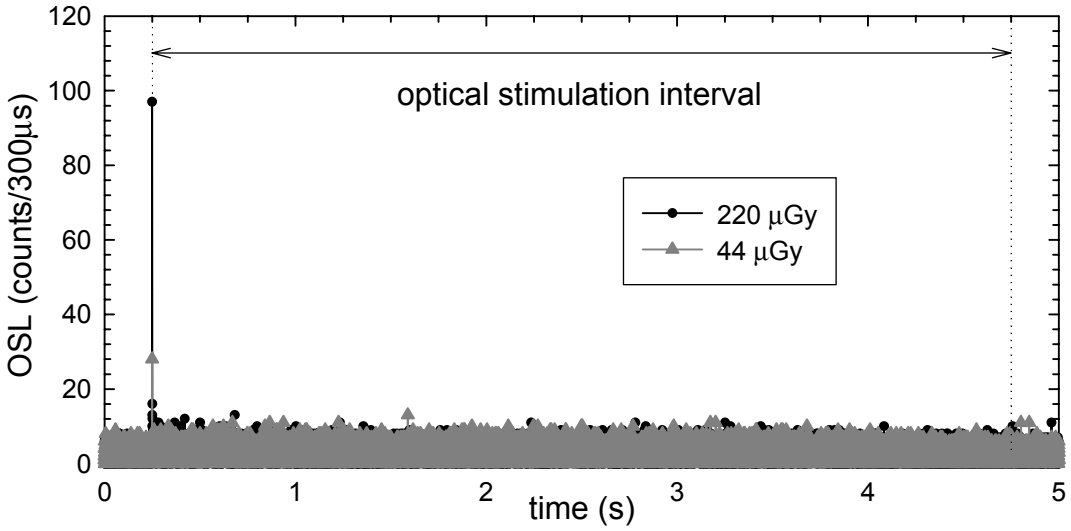

Fig. 7.7: Processed OSL signals (OSL integration time $300\mu s$) measured for KBr:Eu irradiated at $44\mu Gy$ and $220\mu Gy$

It can be noticed in figure 7.6 that turning off the stimulation signal does not have any

obvious effect on the luminescence background level, indicating a sufficient amount of red laser light filtration achieved even after the removal of 4*mm* of 5-58 filters.

The minimum detectable dose corresponds to an OSL level equal to the background average plus 3 times the standard deviation of the background. As can be seen from figure 7.6, the signal-to-noise ratio (SNR) can be improved by a judicious choice in the integration time of the OSL signal. Therefore, the data was further processed so that the OSL integration time was increased from $100\mu s$ to $300\mu s$, and the resulting data set was plotted in figure 7.7. Subsequently, the minimum detectable dose was calculated with the parameters given in table 7.1.

Absorbed dose (μGy)	44	220
Average background (counts)	2.81	2.92
Background standard deviation (counts)	1.77	1.81
Minimum detectable level (counts)	8.12	8.36
OSL maximum (counts)	28	97
Minimum detectable dose (μGy)	14.5	21.5

Table 7.1: Parameters of the OSL decays of KBr:Eu at low doses, used in the determination of the minimum detectable radiation dose

It can be noticed that the measurement at a lower dose of $44\mu Gy$ indicates a minimum detectable level of $14.5\mu Gy$, slightly lower than the value indicated by the measurement at a higher dose. This can be attributed to the fading of the signal, during irradiation at a small dose rate of approximately $0.88\mu Gy/s$. In order to absorb a dose of $220\mu Gy$, the sample needed to be irradiated for a period of time of approximately 250*s*, during which time significant fading has diminished the value of the OSL maximum. In any case, data

in table 7.1 indicates that radioactive activity can be positively identified in sources emitting dose rates as low as $1\mu Gy/s$.

Presumably, the sensitivity of the reader can be further improved by using larger KBr:Eu detectors (the volume of the investigated sample was on the order of $3x0.3x0.3mm^3$). Volume increases on the order of two orders of magnitude are easily achievable, and they would presumably lead to sensitivity increase in the same amount.

CHAPTER EIGHT

CONCLUSIONS AND FUTURE WORK

8.1. Summary

Local dose measurements constitute the only method by which the true spatial distribution of the dose absorbed in the body during a radiotherapy procedure can be obtained. Since the success of the cancer treatment depends greatly on the precision at which the prescribed radiation dose is delivered to the tumor and to the surrounding tissue, a reliable system able to perform in-vivo, real-time and localized dose measurements would constitute the ultimate quality assurance tool in radiotherapy.

This thesis presents a series of steps performed by us in designing, building and testing of a clinical dosimetry reader based on Optically Stimulated Luminescence (OSL) of two different materials: Al_2O_3:C and KBr:Eu. The system is intended to perform real-time, localized measurements of the dose deposited in tissue during radiotherapy treatments. The dose information is transported from the detector (dosimeter) to the processing unit (OSL reader) in the form of light; thus, the system is immune to electrical interference. Due to the small dimension of the dosimeter, it is possible to perform dose measurement with a high spatial resolution. Those same small dimensions constitute an important advantage allowing the radiation sensor to be placed at the tumor location within the patient's body during a procedure that is minimally invasive.

During irradiation, some of the energy of the incident particles is deposited in the medium they pass through. In OSL materials, part of this energy is transferred to the elementary charges, a fraction of which subsequently become trapped at defect sites

preexisting in the crystalline lattice. The remaining charges promptly lose the excess energy and relax via radiative processes; the luminescence emitted is known as radioluminescence (RL). When stimulation light is applied to an OSL dosimeter that contains a trapped charge population, the charges can absorb energy from the stimulation beam, get released form the defect sites, and relax emitting optically stimulated luminescence (OSL). If the luminescence background is affected by various types of noise emitted in the optical light guide, the OSL signal originates in the dosimeter crystal alone, and is emitted in an amount proportional to the radiation dose absorbed in the sample. For a sample being simultaneously irradiated and stimulated optically, the OSL component of the luminescence can be separated from the fluorescence background by a temporal method, as described in chapter 3. In order to reliably use the OSL signal as a measure of the absorbed dose, it is necessary to solve a number of issues related to both the basic physical properties of the luminescence samples and to engineering details required in the optimization of the reader.

The main concern raised in the case of both studied materials was an effective increase in the sensitivity of the samples being irradiated. The situation was attributed to the presence of multiple types of defects in the crystalline structure of the OSL materials, leading to competition effects, the magnitude of which is dependent upon the relative filling levels of different traps. In order to compensate for the sensitivity variations, different correcting algorithms have been separately designed, implemented and tested for each type of OSL material under investigation. If in the case of KBr:Eu, the fast rate of the OSL decay allows for a complete depletion of the trap population in short time intervals on the order of tens of milliseconds. For Al_2O_3:C, the relatively low sensitivity

to optical stimulation, in conjunction with the need for fast measurements, eventually determined us to design an algorithm based on incomplete OSL depletion which allowed us to take measurements at a rate of approximately $0.5Hz$.

The engineering challenges were, again, different for the two materials. In the case of Al_2O_3:C, the difficulties were related to choosing the proper optical components that would accommodate a high enough stimulation power ($100mW$). Also, because of the relative spectral proximity of the stimulation and luminescence light, high-quality filtration has to be used in front of the light detector for discriminating the latter from the former. Due to its high speed, KBr:Eu required increased computation power, and DAQ hardware able to perform synchronous data acquisition at frequencies up to $10kHz$. However, the ability to stimulate the OSL with light of a wavelength situated relatively far away from the luminescence relaxed the requirements imposed on the quality of filtration and on the necessary amount of optical stimulation power.

Besides testing in laboratory environment using ^{90}Sr and X-ray sources, the OSL readers were evaluated by phantom-irradiations with clinical irradiation sources. These tests, described in detail in chapter 6 of this thesis, concentrated on issues such as stability of the system, quantified by the repeatability of the measurements, and accuracy, in terms of comparisons with dose measurements performed with classical dosimeters such as ionization chambers.

A summary of the most important characteristics defining the operation of the readers, and calculated in chapter 6 from experimental data obtained during the clinical irradiations performed in Fort Collins, CO., is reproduced in table 8.1.

The reproducibility of the measurements is estimated from the dose deposition curves

obtained as described in sections 6.2.7. and 6.3.3., for Al_2O_3:C and KBr:Eu, respectively. The standard deviations of the sets of three measurements have values in the range given in table 8.1. For both materials, the reproducibility is better at higher measured doses. The bold number in parentheses represents the average of the standard deviations obtained at different depths in the water phantom, weighted by the measured doses, and indicates a two to three-fold increase in overall reproducibility for the measurements performed with KBr:Eu, as compared to Al_2O_3:C.

OSL reader	Al_2O_3:C	KBr:Eu
Reproducibility (%)	2.2 – 9.5 (**5.03**)	0.76 – 5.15 (**1.79**)
Accuracy (%)	3.7	2.8
Speed (dose updates / irradiation)	9-10	>300

Table 8.1: Summary of the performance indicators for the OSL readers based on Al_2O_3:C and KBr:Eu under irradiation with a clinical source

The accuracy refers, as described in section 6.3.3., to the correlation between the dose-depth measurements from OSL and ionization chambers, weighted to the different measured doses. KBr:Eu shows a slightly better performance than Al_2O_3:C.

The speed of the measurements is probably the factor making the most significant difference in the operation of the two systems. During each irradiation that lasted for about 20 seconds, the OSL reader based on Al_2O_3:C was able to update the total absorbed dose for 9 to 10 times. Under the same conditions, the dose obtained from the KBr:Eu dosimeter was updated for more than 300 times, an increase of more than one order of magnitude.

The measurements speed becomes vital if the dosimeter is to be used as a control for the

delivered dose – i.e., if the dose information from the OSL reader is used to decide when the irradiation source is to be turned off, after delivering the prescribed dose of radiation to the tumor. Based on the speed characteristics mentioned before, it should be expected that the Al_2O_3:C reader would determine a dose larger by up to 10% to be delivered to the patient. In contrast, the KBr:Eu reader would be able to control the dose within 0.3%.

Alternative uses for the OSL fiber dosimeter have also been investigated in this thesis. Among them, we have suggested a 2-dimensional dose mapping system based on the OSL of thin layers of Al_2O_3:C. Also, a possible application of the KBr:Eu reader for real-time detection of radiation sources was proposed, and it has been proven that detection of doses on the order of $10\mu Gy$ is possible even at this incipient stage of research.

8.2. Conclusions and future research directions

So far, our research has been focused on a multitude of aspects required by the design and implementation of the fiber OSL reader, including studies of basic OSL material properties, development of suitable algorithms for signal acquisition and processing, and engineering issues related to the OSL readers.

Some of the limitations in the basic material properties can be overcome by data processing procedures. For instance, it has been noticed that all the investigated samples suffer changes in sensitivity, when used in 'real-time' mode, and the phenomenon has been attributed to competition effects induced by the presence of multiple types of traps. We have been able to compensate for the sensitivity changes by employing specific correcting algorithms, which are essentially based on combinations of the following:

• Controlling the establishing of equilibrium in different OSL components after

transitions in irradiation dose rate by applying different amounts of stimulation light;

• Dynamically estimate the shape of the OSL decay;

• Prevent the upsetting of the material sensitivity induced by over-depletion of the competing traps, by controlled application of the laser stimulation;

• Preferentially use one component of the OSL to extract dose information.

Other limitations induced by the material properties, such as the slowly-decaying DOSL signal, induced by the presence of shallow traps in Al_2O_3:C, cannot be balanced by processing algorithms. The only viable solutions to the DOSL problem, as well as to the relatively long decay time of the OSL signal from Al_2O_3:C can only be solved by further improvements in the material growth techniques.

The characteristics of the KBr:Eu samples can be presumably improved further by material engineering. The area of investigation is vast, and a comprehensive study would involve determining the influence of dopant concentration, parameters of the crystal growth process, especially the speed of pulling from the melt in a Czochralski-type of growth, and post-growth thermal treatment on the OSL properties of the KBr:Eu dosimeters. In the very near future, we plan on growing single crystals of KBr:Eu in the Crystal Growth Laboratory of the Department of Physics at OSU, in collaboration with Dr. J.J. Martin and Mr. C. Hunt. The project also involves performing a basic characterization of the OSL properties of interest of the grown crystals, and tailoring the growth parameters in order to maximize the quality of the crystals as OSL dosimeters.

We plan on further improve the engineering aspects in the building of the OSL readers. In the case of the OSL reader based on Al_2O_3:C, tasks for the near future involve testing of different types of optical fiber cables, and improving the optical coupling between the

dosimeter sample and the silica fiber. For the KBr:Eu reader, a possible transition to an analog type of light detector capable of achieving a larger dynamic range of the measured OSL signal will be investigated.

It is imperatively necessary to continue the testing in medical environment. Beyond performance tests that can be performed in water phantoms, the next step would involve dosimetry with the fiber probes inserted in tissue samples. A study performed on living test animals, in collaboration with the OSU Department of Veterinary Medicine, would allow us to estimate the extent of the damage induced to the tissue by the catheters that would be used to insert the dosimeter sample at the tumor location. With the increased sensitivity of the KBr:Eu reader, it is possible to use it for localized dose estimations during radiological procedures, during which smaller doses are delivered, but their monitoring is important for radiation protection purposes (i.e. X-rays, computer tomography, and fluoroscopy procedures). The high speeds at which dose estimations are made recommend our high-resolution reader as a valuable tool able to perform a quick dose rate mapping of radioactive seeds used in brachytherapy. It is easy to envision an automated system able to translate the fiber-attached dosimeter along a regular pattern in a water phantom, allowing for rapid 3-dimensional dose rate mapping of radioactive sources, such as brachytherapy seeds.

The ability to discern individual irradiation pulses emitted by a medical linear accelerator (LINAC) with our KBr:Eu reader suggests that it is possible to create the ultimate clinical dosimetry tool: the dosimeter able to measure in real time the dose deposited locally by each and every radiation pulse output by the LINAC. In this configuration, the modulation of the laser stimulation would have to be synchronized with the radiation

pulses, such that every stimulation 'pulse' occurs immediately after the end of the irradiation pulse. At this time scale, when the OSL is measured between irradiation pulses, the physical approach simplifies to the classical case when optical stimulation is applied after, rather than during irradiation, thus making the subtraction of the fluorescence background irrelevant in the course of the procedure. The OSL material (KBr:Eu) has already proven that it is capable of performing at such high speeds, as shown in chapter 6. The only improvements needed to achieve this type of operation are strictly related to instrumentation – higher computation power for speed optimization, and finding the right LINAC output where to extract the synchronization signal from.

In terms of the alternate uses of the fiber dosimeter, the main interest resides in further improving the detectability of small doses for the KBr:Eu fiber samples. Since the criteria in choosing the dimensions of the dosimeter are not as tight as in the case of medical applications, increasing the volume of the dosimeter even by orders of magnitude is possible in order to attain the desired sensitivity. Also, sensitivity increases should be expected from the optimization of the crystal growth process.

On a longer term, it is in our intention to investigate the possibility of building of an inexpensive, small-dimension OSL dosimeter based on KBr:Eu, in which the stimulation will be provided by a red light-emitting diode (LED), and the luminescence will be read by a light detector such as a semiconductor photodiode. Such a small, integrated dosimeter could be employed as a radiation monitoring device in a large range of situations when near real-time alerts to radiation exposure would be deemed necessary: medical environment, radioactive waste containing facilities, ports of entry into the country susceptible to illegal transit of radioactive materials.

REFERENCES

[1] Orton, C.G., *Radiation dosimetry: physical and biological aspects*, Plenum Press, New York (1986).

[2] Becker, F.F., *Cancer: A comprehensive treatise, vol. 6: Radiotherapy, surgery and immunotherapy*, Plenum Press, New York (1977).

[3] Hope-Stone, H.F., *Radiotherapy in modern clinical practice*, Granada Publishing Ltd., London (1976).

[4] *Radiation protection guidance for activities in low-earth orbit*, NCRP Report No. 132, (2000).

[5]http://www.healthprotection.org.uk/presentations/The%20Health%20Effects%20of%20Radiation%20and%20Available%20Countermeasures/, 11/2/2003.

[6] Boyer, A.L. et al., *Physics Today*, **55**, No. 9, 34 (2002).

[7] del Regato, J.A., *Cancer: diagnosis, treatment & prognosis, 6th edition*, The C.V. Mosby Company, St. Louis (1985).

[8] Lowry, S., *Fundamentals of radiation therapy and cancer chemotherapy*, Arco Publishing Company, Inc., New York (1974).

[9] Fraas B.A., *Med. Phys.* **22**, 1911 (1995).

[10] Attix, F.H., *Introduction to radiological physics and radiation dosimetry*, Wiley, New York (1986).

[11] http://www.varian.com/onc/prd056.html, 12/15/2003.

[12] Burman C. et al., *Int. J. Rad. Oncol. Phys.*, **39**, 863 (1997).

[13] Kutcher G.J. et al., *Med. Phys.*, **21**, 581 (1994).

[14] *ICRU Report 24: Determination of absorbed dose in a patient irradiated by beams of X*

or Gamma rays in radiotherapy procedures, International Commission on Radiation Units and Measurements, Bethesda, Maryland, USA (1976).

[15] Goitein, M., *Med. Phys.*, **10**, 709 (1983).

[16] Anagnastopoulos G. et al., *Int. J. Radiation Oncol. Biol. Phys.*, **57**, 1183 (2003).

[17] Alecu, R and Alecu, M., *Med. Phys.*, **26**, 768 (1999).

[18] Beddar A.S. et al., *Phys. Med. Biol.*, **37**, 1883 (1992).

[19] Beddar A.S. et al., *Phys. Med. Biol.*, **37**, 1901 (1992).

[20] Beddar A.S. et al., *Phys. Med. Biol.*, **37**, 925 (1992).

[21] Arnfield, M.R., *IEEE Transactions on Nuclear Science*, **43**, 2077 (1996).

[22] Jones, S.C. et al., *Rad. Prot. Dosim.*, **47**, 525 (1993).

[23] Huston, A.L. et al., *Appl. Phys. Lett*, **68**, 3377 (1996).

[24] Creager, R.E. and Soltani, P.K., *U.S. Patent 5,091,653* (1992).

[25] Huston, A.L. and Justus, B.L., *U.S. Patent 6.087,666* (2000).

[26] Huston, A.L. et al., *Nuclear Instr. Meth. Phys. B*, 184, 55 (2001).

[27] Boetter-Jensen, L. and McKeever, S.W.S., *Rad. Prot. Dosim.*, **65**, 273 (1996).

[28] Polf, J.C., et al., *Rad. Prot. Dosim.*, **100**, 301 (2002).

[29] Andersen C.E. et al., *Development of optical fibre luminescence techniques for real-time in-vivo dosimetry in radiotherapy.*, IAEA-CN-96: International Symposium on Standards and Codes of Practice in Medical Radiation Dosimetry, Vienna, Austria (2002).

[30] Eisberg, R. and Resnick, R., *Quantum physics of atoms, molecules, solids, nuclei, and particles, 2nd edition*, Wiley, New York (1985).

[31] Chen, R. and McKeever, S.W.S., *Theory of thermoluminescence and related*

phenomena, World Scientific, Singapore (1997).

[32] McKeever, S.W.S., *Thermoluminescence of solids*, Cambridge University Press, Cambridge (1985).

[33] Kristianpoller, N. et al., *Optical Materials*, **16**, 105 (2001).

[34] De Carcer A. et al., *Radiation Measurements*, **29**, 203 (1998).

[35] Barboza–Flores, M. et al., *Radiation Measurements* **29**, 487 (1998).

[36] Nanto, H. et al., *J. Appl. Phys.* **74**, 1445 (1993).

[37] Nanto, H. et al., *IEEE Transactions on Nuclear Science*, **47**, 1620 (2000).

[38] Buenfil A.E. and Brandan M.E., *Health Physics*, **62**, 341 (1992).

[39] Martin J.J., *private communications*, Oklahoma State University (2003).

[40] http://www.varian.com/onc/prd055.html, 12/09/2003

VITA

Razvan Gaza

Candidate for the Degree of

Doctorate of Philosophy

Thesis: A FIBER-OPTICS, REAL-TIME DOSIMETER BASED ON OPTICALLY STIMULATED LUMINESCENCE OF Al_2O_3:C AND KBr:Eu, FOR POTENTIAL USE IN THE RADIOTHERAPY OF CANCER

Major Field: Physics

Biographical:

Personal Data: Born in Timisoara, Romania, Europe, on May 12, 1973, the son of Iosif and Severina-Maria Gaza.

Education: Graduated from the 'Colegiul Banatean' High School, Timisoara, Romania in 1991; received a Bachelor of Science degree in Physics of Materials and a Master of Science degree in Physics of Magnetic Materials from the Western University of Timisoara, Romania, in 1996 and 1998, respectively. Completed the requirements for a Doctorate of Philosophy degree with a major in Physics at Oklahoma State University in May 2004.

Experience: Employed as a photo-video operator / technical consultant by Poliphem Smile, Ltd., between 1996 and 1999; employed by the Department of Physics at Oklahoma State University as a Teaching Assistant between 1999 and 2001, and as a Research Assistant, 2002 to 2004.

Professional Membership: American Physical Society (APS) since 1999; American Association of Physicists in Medicine (AAPM) since 2003; Member-elect of the National Honor Society of Phi Kappa Phi since 2002.